optica

Volume 1 • Issue 1 • July 2014

OSA®
The Optical Society

ISSN: 2334-2536

optica.osa.org

optica

Welcome to *Optica*: a new home for high-impact optics and photonics research

ALEXANDER L. GAETA

Received 14 July 2014 (Doc. ID 217044); published 22 July 2014

Editor-in-Chief, Alexander Gaeta, announces the launch of *Optica*, OSA's new open-access journal for high-impact results. © 2014 Optical Society of America

OCIS codes: (000.1200) Announcements, awards, news, and organizational activities; (000.5360) Physics literature and publications.

http://dx.doi.org/10.1364/OPTICA.1.000ED1

I am very pleased to introduce the inaugural issue of *Optica*. This new, online-only, open-access journal, published monthly, is devoted to the rapid dissemination of high-impact results in all areas of optics and photonics, from fundamental studies to applied technology. The idea for *Optica* grew out of many discussions between OSA publication volunteers and researchers in the field regarding the need for a journal that provided authors with an outlet for their highest profile results and that would be of interest and accessible to the optics and broader scientific communities. After a thoughtful and deliberate vetting process by various volunteer governance committees, *Optica* was ultimately approved by the OSA Board of Directors.

Optica will publish original research letters (4 pages), research articles (6–8 pages), and mini reviews (8–12 pages). Each paper submitted to *Optica* will undergo an initial review by the Editorial Board to determine its potential suitability for the journal, at which point the paper will be sent for peer review or be declined. The Editorial Board will strive to make this initial decision on suitability within five business days or less, which will ensure that authors can quickly submit their work to another journal if it is declined by *Optica* at this stage. A unique feature of the journal is that authors whose papers are declined, either at this initial editorial stage or after the peer review process, may have the option, as determined by the Associate Editor(s), to transfer their manuscript to another of the many excellent OSA journals and maintain the original submission date to *Optica*. Newsworthy articles that are accepted for publication will be promoted via coordinated media outreach and distributed broadly.

The Editorial Board is comprised of a fantastic group of high-profile researchers and has a diversity of expertise that covers all areas of optics and photonics. They will work hard to ensure that papers are given careful consideration but are also dealt with quickly to maintain the spirit of rapid dissemination. I am also very pleased to introduce an additional member of the editorial staff, Dr. Alison Taylor, who will serve as the Executive Editor. Alison has a Ph.D. in optics, and she brings a wealth of editorial experience with over twelve years working in not-for-profit publishing at the American Physical Society and the American Institute of Physics. She will work closely with me and the Editorial Board on all aspects of the journal to ensure that it functions at the highest level.

As the founding Editor-in-Chief, I am extremely gratified by the enthusiastic support from the OSA volunteers, staff, and the general optics community. Starting a journal with such lofty goals is challenging. Nevertheless, I am highly encouraged by the superb articles that have already been submitted and the thoughtful reviews that the Associate Editors have obtained from the referees.

The inaugural issue consists of an impressive and diverse set of papers. These include letters by Lavery *et al.* on observation of rotational Doppler shifts and Rosenthal *et al.* on using filaments in air to collect light signals. There are also five research articles: Papp *et al.* demonstrate an optical clock based on a microresonator frequency comb; Nakazawa *et al.* demonstrate a novel type of laser - the Nyquist laser; Jalali *et al.* model optical data compression and expansion using time bandwidth engineering; Zhu *et al.* propose a novel design for self-cooling solar cells; and Seaberg *et al.* perform extreme ultraviolet

2334-2536/14/010ED1-02$15/0$15.00 © 2014 Optical Society of America

imaging using tabletop-size laser technology. In addition, we have an excellent review on third generation femtosecond technology by Fattahi *et al.*

Lastly, many aspects of *Optica* were developed based on extensive conversations I had with many colleagues, and I continue to welcome your thoughts and suggestions on how we can further improve the journal.

Alexander Gaeta
Editor-in-Chief
Optica

optica

Observation of the rotational Doppler shift of a white-light, orbital-angular-momentum-carrying beam backscattered from a rotating body

MARTIN P. J. LAVERY,* STEPHEN M. BARNETT, FIONA C. SPEIRITS, AND MILES J. PADGETT

School of Physics and Astronomy, University of Glasgow, Glasgow, UK

**Corresponding author: martin.lavery@glasgow.ac.uk*

Received 29 April 2014; accepted 29 May 2014 (Doc. ID 210521); published 22 July 2014

We observe the rotational Doppler shift of an orbital angular momentum (OAM)-carrying white-light beam after it is backscattered from a rotating object. Unlike the well known linear shift, this rotational shift is independent of the optical frequency, and hence each spectral component of the scattered light is shifted by the same value. Consequently, even a white-light source can give rise to a single-valued frequency shift. We show that the size of this shift is proportional to the OAM of the light and that superpositions of different OAM states give rise to multiple frequency sidebands. The observability of this rotational shift for white-light illumination highlights the potential for the rotational Doppler effect to form the basis of a rotational sensor for the remote detection of spinning objects. © 2014 Optical Society of America

OCIS codes: (000.2190) Experimental physics; (280.3340) Laser Doppler velocimetry; (280.7250) Velocimetry; (260.6042) Singular optics; (280.4788) Optical sensing and sensors; (280.1350) Backscattering.
http://dx.doi.org/10.1364/OPTICA.1.000001

The linear Doppler effect is the well-known frequency shift of a light beam that arises as a result of the relative motion between a source and an observer. This frequency shift scales with both the unshifted frequency and the linear velocity, an effect extensively used in Doppler velocimetry to detect the translational motion of surfaces and fluids [1,2]. Less well known than this linear effect is the rotational equivalent, where the frequency shift is proportional to the product of the rotational velocity between the source and the observer and the orbital angular momentum (OAM) of the light [3–8], such that $\Delta\omega = \ell\Omega$. Here, Ω is the angular rotational frequency and the illuminating field has an OAM of $\ell\hbar$ per photon. We reported recently that this rotational Doppler effect is manifest in monochromatic laser light backscattered from a spinning object, even in cases where the linear velocity between the source and observer is zero [9]. The effect has also been observed for a single point scatterer rotating about the optical axis of an illuminating beam [10]. In this last guise, the effect is similar to that predicted for the frequency shifts of atomic transitions when moving atoms are interrogated with light beams containing OAM [11]. The dependence of the rotational Doppler shift upon the angular momentum carried by the light means that in order to observe a single-valued shift, one needs to be selective in the angular momentum modes used either for illumination of the surface or in the detection of light scattered from it.

One striking feature of the rotational effect is that while the linear shift scales with the unshifted frequency, the rotational effect does not. Hence, for the rotational effect, all the frequencies within the same spatial mode of a white-light beam should be frequency shifted by the same amount. This ability to use white light suggests that the natural emission of light from a spinning object may result in a sufficiently large signal to allow the remote detection of spinning objects without the need for dedicated illumination.

In this present work we observe the rotational Doppler shift from a white-light source after it is backscattered by a spinning object. We show that the magnitude of this shift is dependent upon the OAM of the light, and that superpositions of different OAM states give rise to multiple sidebands on the shifted frequency. The observability of the frequency shift for white-light illumination highlights the potential of this rotational Doppler effect as the basis of a rotational sensor using backscattered light.

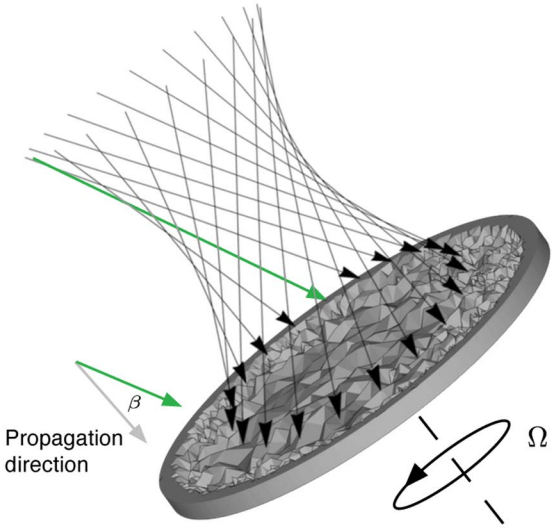

Fig. 1. For a helically phased beam (i.e., one carrying orbital angular momentum), the local ray direction is inclined by an angle $\beta = \ell/k_0 r$ with respect to the propagation direction. When used to illuminate a spinning object, this incline results in a frequency shift of the scattered light similar to that obtained in Doppler velocimetry.

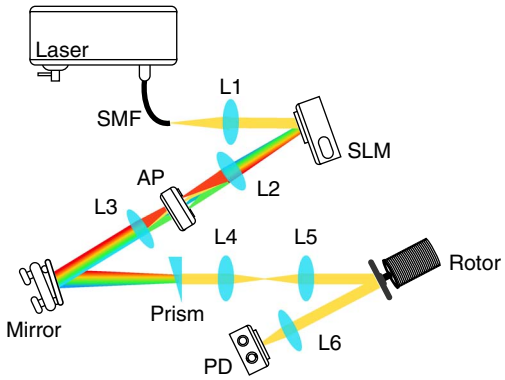

Fig. 2. A supercontinuum laser source is coupled into a single-mode fiber (SMF) to produce a spatially coherent beam of white light, which is then collimated by a lens, L1, and illuminates a spatial light modulator (SLM). The SLM is encoded with a combination of fork diffraction patterns, such that the first-order diffracted beam is of the desired OAM superposition ℓ. A spatial filter, AP, is placed in the focal plane of a lens, L2, and used to select the first-order diffracted beam of all the wavelength components. To compensate for chromatic dispersion resulting from the diffraction grating, the first-order beam is then reimaged onto a prism, yielding a white-light OAM-carrying beam within which all the wavelength components are coaxial. This white OAM is reimaged onto the spinning rough surface, and the backscattered light is collected by a photodetector, PD, to measure the intensity modulation frequency.

The linear Doppler shift is usually associated with the line-of-sight component of velocity between the source and observer. However, the Doppler effect can also be observed from transverse motion. If a moving rough surface is illuminated at an oblique angle, the light of frequency ω_0 scattered at normal incidence is subject to a reduced Doppler shift given by $\Delta\omega = (\omega_0 \sin \alpha)v/c$, where α is the angle between the illumination and the surface normal and v is the transverse velocity of the surface. Oblique illumination can take many forms; light is normally represented as a plane wave, but other phase structures are also possible. In particular, light beams with helical phasefronts, i.e., with a phase structure described by $\Psi(\phi) = \exp(i\ell\phi)$, carry an OAM of $\ell\hbar$ per photon [12,13]. These helical phasefronts correspond to a local skew angle of the Poynting vector (or local ray direction) of $\beta = \ell/k_0 r$, where k_0 is the wave number and r is the radius vector [14] (see Fig. 1). Consequently, for a surface spinning with an angular velocity Ω, and illuminated by a light beam with helical phasefronts, the on-axis scattered light is subject to a frequency shift of $\Delta\omega = \Omega\ell$. We note that, unlike the linear Doppler shift, this angular Doppler shift is independent of the frequency of the incident light and hence should be observable as a single shift for a scattered white-light beam. Rather than measure this frequency shift directly, it is convenient to create an illumination beam comprising two different values of OAM, ℓ_1 & ℓ_2, such that the scattered light comprises two different frequency components that interfere to produce a modulation in the detected intensity, $f_{\text{mod}} = \Omega|\ell_1 - \ell_2|/2\pi$.

Figure 2 shows the experimental arrangement for observation of the white-light rotational Doppler shift. A supercontinuum white-light source (Fianium SC400-6) is coupled to a single-mode fiber to define the light's spatial coherence. The output from this fiber is allowed to diverge and then collimated to illuminate a spatial light modulator (SLM). If the SLM is programmed with a simple diffraction grating containing an on-axis fork singularity, the resulting first-order diffracted beam possesses helical phasefronts [15]. The approach can readily be extended to create superpositions of helically phased beams [16], in our case with indices ℓ_1 and ℓ_2. The combination of a diffractive approach and a broad spectral source means that this first-order light is subject to angular dispersion. This angular dispersion is compensated by an appropriate prism placed in the image plane of the SLM, resulting in a collimated white-light beam with the chosen modal structure [17]. This phase-structured white-light beam is reimaged to the rotation axis of the scattering surface. The details of the scattering surface are not critical to the observation of the rotational Doppler effect. In this case the surface was plastic, of rough texture on the scale of a millimeter, and sprayed with a silver paint. The scattered light is then collected by a large-aperture lens and relayed to a large-area photodiode. Note that in this configuration the modal selectivity comes from the illumination light and the detection system is multimodal. However, as demonstrated in our earlier work, the modal selectivity can instead be incorporated into the detection system [9]. The output of this photodiode is acquired by computer, digitized, and Fourier transformed such that the frequencies of the resulting intensity fluctuations can be observed and recorded. The rotational speed of the surface could also be recorded and logged using a simple optical pulse counter measuring the periodic signal from a reflective mark on the rotation axle.

Figure 3 shows a typical power spectrum of the intensity fluctuations recorded in the white light that is backscattered from the spinning surface. Figure 4 is a graph showing the

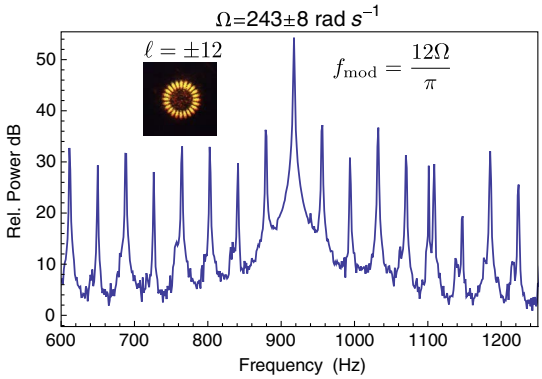

Fig. 3. The recorded time sequence of the intensity backscattered from the spinning surface is Fourier transformed to give a power spectrum from which the peak modulation frequency in this backscattered light can be measured. The power normalization is with respect to the noise floor of the detector (0 dB). The inset shows the intensity cross section of the OAM superposition $\ell = \pm 12$.

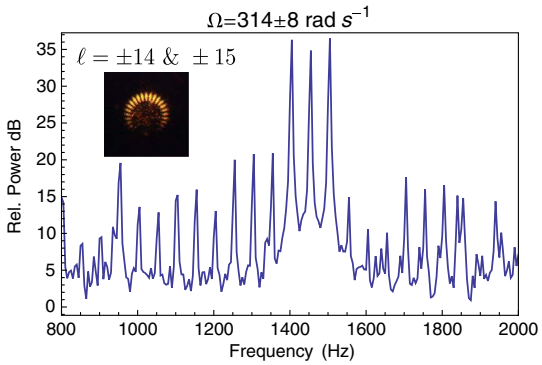

Fig. 5. The observed power spectrum in the intensity modulation of the scattered light obtained spinning surface is illuminated with a superposition of $\ell = \pm 14$ & ± 15. This superposition results in a cluster of peaks, corresponding to the integer differences between the various OAM components of the illuminating light. The power normalization is with respect to the noise floor of the detector (0 dB). The inset shows the intensity cross section of the OAM superposition $\ell = \pm 14$ & ± 15.

measured frequency of the largest peak in the power spectrum as a function of both the spin rate of the surface and the modal superposition of the illumination (insets show the intensity structure of the illumination beam). In each case, the intensity cross section of the illuminating beams corresponds to a petal pattern with $|\ell_1 - \ell_2|$ rotational symmetry. As anticipated, the power spectrum reveals a peak in the intensity modulation at an angular frequency $f_{\mathrm{mod}} = \Omega|\ell_1 - \ell_2|/2\pi$. This peak is approximately 20 dB above various other peaks at frequencies corresponding to integer differences $|\ell_1 - \ell_2|$. The origin of these additional peaks is consistent with modal impurities that are inherent in either lateral or angular misalignment of the illumination beam and/or slight aberrations in the optical system [18]. The main source of uncertainty in our results is not the identification of the peak in the power spectrum; rather, it is the uncertainty in the stability and measurement of the rotation speed of the motor to which the scattering surface is attached. This uncertainty in rotation speed is $\approx \pm 1$ Hz, equivalent to $\approx \pm 7$ rads^{-1}.

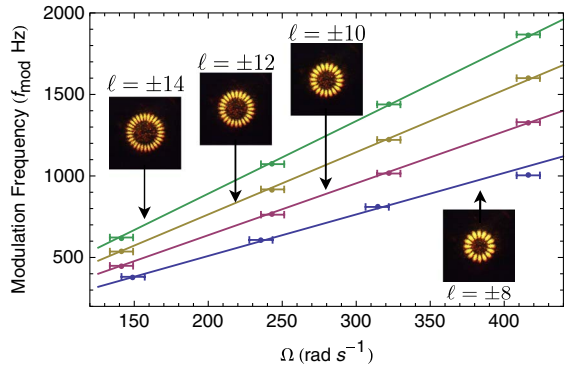

Fig. 4. Observed modulation frequency plotted as a function of rotation rate for four different superpositions of illuminating OAM, $\ell = \pm 8, \pm 10, \pm 12, \pm 14$. The predicted frequency of the intensity modulation is $f_{\mathrm{mod}} = \Omega|\ell_1 - \ell_2|/2\pi$, shown as a solid line. The insets show the intensity cross section of the various OAM superpositions.

To explore the influence of modal composition on the measured power spectrum, we deliberately created an illumination beam comprising multiple OAM modes. Figure 5 shows a specific example of the power spectrum obtained when the illuminating beam is an OAM superposition of $\ell_1 = 14$ & 15 and $\ell_2 = -14$ & -15. As anticipated, we observe significant peaks at modulation frequencies corresponding to 28 and 30 Ω, but we also observe a peak at 29 Ω. This latter peak corresponds to the interference between $\ell = \pm 14$ and $\ell = \mp 15$. The presence of this latter peak emphasizes that for modal superpositions, rather than obtaining a single-valued frequency shift that scales with the average OAM values, the spectrum comprises individual peaks that correspond to the pure OAM modes contained within the modal superposition. It is this last result that demonstrates that the OAM is the natural basis in which to both describe and calculate this rotational Doppler effect.

In this work we have observed the rotational Doppler shift within white light backscattered from a rotating object. We have shown that unlike the linear Doppler effect, the rotational Doppler effect is achromatic, in that all spectral components are shifted by the same frequency. We have also shown that OAM is the natural choice of basis set where, within a modal superposition, it is the individual pure OAM modes that give rise to an independently observable frequency shift. The observability of the rotational Doppler shift even for white-light sources suggests its applicability for the remote sensing of rotating objects. Applications for remote sensing based on this rotational Doppler shift have been suggested in various astronomical situations [19] but should also be applicable to terrestrial applications.

FUNDING INFORMATION

Engineering and Physical Sciences Research Council (EPSRC)—COAM (EP/I012451/1); European Research Council (ERC)—TWISTS; The Royal Society.

REFERENCES

1. T. Asakura and N. Takai, Appl. Phys. **25**, 179 (1981).
2. R. Meynart, Appl. Opt. **22**, 535 (1983).
3. B. A. Garetz, J. Opt. Soc. Am. **71**, 609 (1981).
4. I. Bialynicki-Birula and Z. Bialynicka-Birula, Phys. Rev. Lett. **78**, 2539 (1997).
5. J. Courtial, K. Dholakia, D. A. Robertson, K. Dholakia, L. Allen, and M. J. Padgett, Phys. Rev. Lett. **80**, 3217 (1998).
6. S. Barreiro, J. W. R. Tabosa, H. Failache, and A. Lezama, Phys. Rev. Lett. **97**, 113601 (2006).
7. A. Belmonte and J. P. Torres, Opt. Lett. **36**, 4437 (2011).
8. F. C. Speirits, M. P. J. Lavery, M. J. Padgett, and S. M. Barnett, Opt. Lett. **39**, 2944 (2014).
9. M. P. J. Lavery, F. C. Sperits, S. M. Barnett, and M. J. Padgett, Science **341**, 537 (2013).
10. C. Rosales-Guzmån, N. Hermosa, A. Belmonte, and J. P. Torres, Sci. Rep. **3**, 2851 (2013).
11. L. Allen, M. Babiker, and W. L. Power, Opt. Commun. **112**, 141 (1994).
12. L. Allen, M. W. Beijersbergen, R. J. C. Spreeuw, and J. P. Woerdman, Phys. Rev. A **45**, 8185 (1992).
13. A. M. Yao and M. J. Padgett, Adv. Opt. Photon. **3**, 161 (2011).
14. J. Leach, S. Keen, M. J. Padgett, C. Saunter, and G. D. Love, Opt. Express **14**, 11919 (2006).
15. V. Y. Bazhenov, M. V. Vasnetsov, and M. S. Soskin, JETP Lett. **52**, 429 (1990).
16. S. Franke-Arnold, J. Leach, M. J. Padgett, V. E. Lembessis, D. Ellinas, A. J. Wright, J. M. Girkin, P. Öhberg, and A. S. Arnold, Opt. Express **15**, 8619 (2007).
17. A. J. Wright, J. M. Girkin, G. M. Gibson, J. Leach, and M. J. Padgett, Opt. Express **16**, 9495 (2008).
18. M. V. Vasnetsov, V. A. Pas'ko, and M. S. Soskin, New J. Phys. **7**, 46 (2005).
19. M. Harwit, Astrophys. J. **597**, 1266 (2003).

optica

Collection of remote optical signals by air waveguides

E. W. Rosenthal, N. Jhajj, J. K. Wahlstrand, and H. M. Milchberg*

Institute for Research in Electronics and Applied Physics, University of Maryland, College Park, Maryland 20742, USA

**Corresponding author: milch@umd.edu*

Received 22 April 2014; revised 9 June 2014; accepted 10 June 2014 (Doc. ID 210659); published 22 July 2014

Collection of weak signals from remote locations is the primary goal and the primary hurdle of optical standoff detection schemes such as light detection and ranging and laser-induced breakdown spectroscopy. Typically, the measured signal is enhanced using large-NA collection optics and high-gain detectors. We show that the signal in remote detection techniques can be enhanced by using a long-lived air waveguide generated by an array of femtosecond filaments. We present a proof-of-principle experiment using an air plasma spark source and a ~1 m air waveguide showing an increase in the collected signal of ~50%. For standoff distances of 100 m, this implies that the signal-to-noise ratio can be increased by a factor ~10^4. © 2014 Optical Society of America

OCIS codes: (010.0280) Remote sensing and sensors; (190.7110) Ultrafast nonlinear optics; (230.7370) Waveguides; (300.6365) Spectroscopy, laser induced breakdown.

http://dx.doi.org/10.1364/OPTICA.1.000005

In optical standoff detection techniques, spectroscopic or other light-based quantitative information is collected from a distance. Among the most popular schemes are light detection and ranging (lidar) and laser-induced breakdown spectroscopy (LIBS). In lidar, the signal is induced by a laser pulse, either by reflection or backscattering from distant surfaces or atmospheric constituents. In remote LIBS, laser breakdown of a distant target is accompanied by isotropic emission from characteristic atomic and ionic species. Some recent schemes for optical standoff detection use femtosecond filamentation, which occurs when an ultrashort pulse, propagating through a transparent medium such as the atmosphere, experiences focusing from its self-induced Kerr lens [1]. When self-focusing is stronger than beam diffraction, the beam mode collapses into a tight core or filament where the local intensity reaches the ionization threshold of the medium. The beam collapse is then arrested by plasma defocusing. The interplay of focusing and defocusing over the pulse temporal envelope leads to extended propagation of the filament core over distances typically exceeding many Rayleigh lengths. The ability to deliver high peak intensities at relatively long distances has been applied to lidar [2] and LIBS [3] and other remote sensing schemes [4,5]. Other applications of filaments include terahertz generation [6,7], supercontinuum and few-cycle pulse generation [8,9], channeling of electrical discharges [10], and microwave guiding [11].

Recently, we have studied the long-term hydrodynamic response of the gas through which a filament has propagated [12,13]. Unique to femtosecond filaments is their extended high-intensity propagation over many Rayleigh lengths and their ultrafast nonlinear absorption in the gas, stored in plasma and atomic and molecular excitation [12–16]. This creates an axially extended impulsive pressure source to drive gas hydrodynamics. After the filamenting pulse passes, a gas density depression or hole grows over several hundred nanoseconds. Over the same time scale, a single-cycle acoustic wave is launched and begins to propagate away from the hole, which then slowly decays by thermal diffusion over milliseconds. Understanding this evolution has led to our use of symmetric filament arrays to generate very long-lived air waveguide structures [14] that can support very high-power secondary laser pulses. On microsecond time scales, the colliding acoustic waves launched by the filament array form a fiber-like guiding structure with a gas density (or refractive index) enhancement in the center [14,16]. On time scales well past the acoustic response, the residual gas density holes thermally relax and spread over milliseconds, forming the cladding of a long-lived fiber-like structure with higher gas density in the center. Even a single filament's acoustic wave [17] can trap light in an annular mode over a microsecond time window, as we have recently explained [16].

In this Letter, we show that femtosecond filament-generated air waveguides can collect and transport remotely

generated optical signals while preserving the source spectral shape. The air waveguide acts as an efficient standoff lens. Here, we demonstrate collection of an isotropically emitted optical signal, the worst case scenario in terms of collection efficiency. Even stronger collection enhancement would apply to directional signals from stimulated backscattering [18] or backward lasing [5]. Our results have immediate impact on remote target applications of LIBS [3] and on lidar studies [2]. Our proof-of-principle experiment tests ~1 m long air waveguides of various configurations, in both the acoustic and thermal regimes. Extrapolation of our results to >100 m waveguides generated by extended filamentation [1,19,20] implies potential signal-to-noise enhancements greater than $\sim 10^4$. Of course, sufficiently uniform filament energy deposition will need to be demonstrated over such distances.

In remote LIBS, as a specific example, laser breakdown of a gas or solid target of interest generates a characteristic line spectrum that allows identification of target constituents. However, as the optical emission from the target is isotropic with a geometrical R^{-2} falloff with source distance, very little of the signal is collected by a distant detector, necessitating large-NA collection optics and high-gain detectors [3]. Schemes to increase the LIBS signal by increasing the plasma temperature and/or density have been proposed, such as use of double pulses [21], but all such methods are still subject to the geometrical factor.

Figure 1 illustrates the experimental setup. Single filaments and filament arrays 75–100 cm long are generated in air using 10 Hz Ti:sapphire laser pulses at 800 nm, 50–100 fs, and up to 16 mJ. The beam focusing is varied between $f/400$ and $f/200$ depending on the type of guide. Arrays with four or eight filaments are generated by phase shifting alternating segments of the beam's near field phase front by π. As described in our earlier work, four-filament arrays, or quad-filaments, are generated using two orthogonal "half-pellicles" [14], and eight-filament arrays, or octo-filaments, are generated using eight-segment stepped mirrors [16], resulting in either a TEM_{11}-like mode or a linear combination of Laguerre–Gaussian $LG_{0,\pm 4}$ modes in the low-intensity beam focus, as seen in Figs. 1(b) and 1(c). Above the self-focusing threshold, the beam lobes collapse into parallel and distinct filaments [14,16]. By inserting burn paper into the paths of the quad- and octo-filaments [14], we have verified that their four- or eight-lobe character is preserved through the whole propagation path. As described above, colliding acoustic waves at the array center launched by either quad-filaments or octo-filaments form waveguides of a duration of ~1 μs, roughly corresponding to the acoustic wave transit time through the array center. Millisecond-lifetime waveguides develop during the slow postacoustic thermal diffusion of the density holes left by the filaments [14].

We tested the signal collection properties of our waveguides using an isotropic, wide-bandwidth optical source containing both continuum and spectral line emission, provided by tight focusing at $f/10$ of a 6 ns, 532 nm, 100 mJ laser pulse to generate a breakdown spark in air. The time evolution of the spectrally integrated spark emission is shown in Fig. 1(a), where the scattered 532 nm signal has been filtered out. The signal FWHM is ~35 ns, with a long, ~1 μs decay containing >85% of the emission. The air spark laser and the filament laser are synchronized with RMS jitter <10 ns. The delay between the spark and the filament structure is

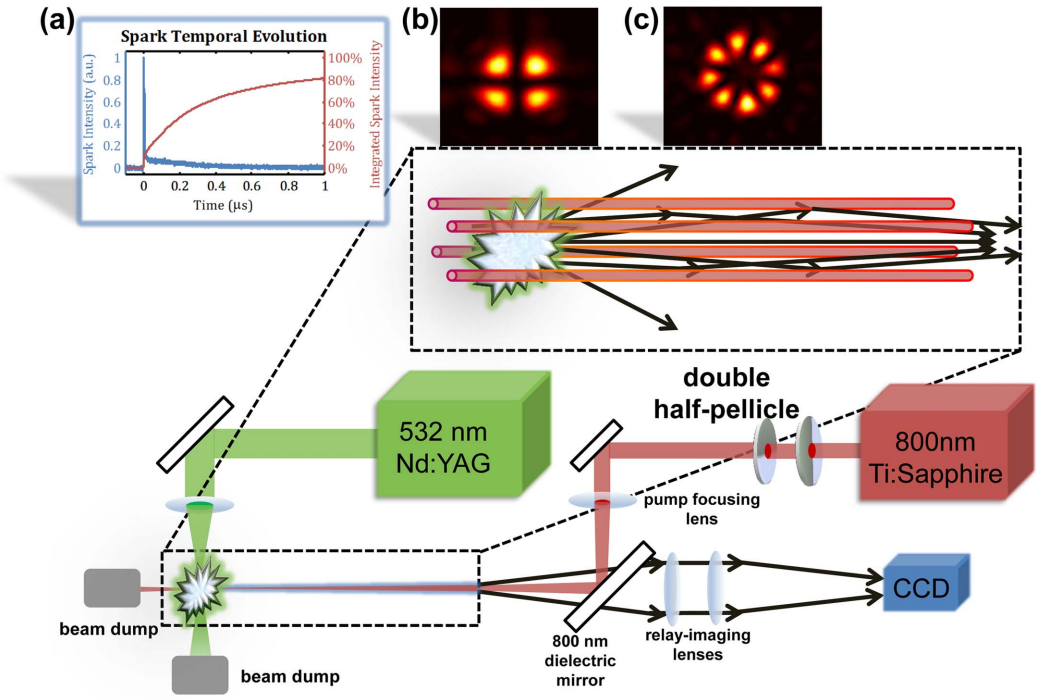

Fig. 1. Experimental setup for demonstration of light collection and transport by the air waveguide. (a) Time evolution of the spectrally integrated emission of the spark (blue curve) and its running integral (red curve), (b) low-intensity image of the four-lobe beam focus generated by orthogonal half-pellicles (shown), and (c) low-intensity image of the eight-lobe beam focus generated by the segmented mirror (not shown).

varied to probe the time-evolving collection efficiency of the air waveguides. The air spark and filament beams cross at an angle of 22°, so that the spark has a projected length of ~500 μm transverse to the air waveguide. As depicted in Fig. 1, the spark is positioned just inside the far end of the air waveguide. Rays from the source are lensed by the guide, and an exit plane beyond the end of the guide is imaged through an 800 nm dielectric mirror onto a CCD camera or the entrance slit of a spectrometer. This exit plane is located within 10 cm of the end of the waveguide.

The collected signal appears on the CCD image as a guided spot with a diameter characteristic of the air waveguide diameter. Guided spots are shown in Fig. 2 for five types of air waveguides: the quad-filament and octo-filament waveguides in both the acoustic and thermal regimes and the single-filament annular acoustic guide. Surrounding the guided spots are shadows corresponding to the locations of the gas density depressions, which act as defocusing elements to scatter away source rays. We quantify the air waveguide's signal-collecting ability using two measures. The peak signal enhancement, η_1, is defined as the peak imaged intensity with the air waveguide divided by the light intensity without it. We define the source collection enhancement, η_2, as the integrated intensity over the guided spot divided by the corresponding amount of light on the same CCD pixels in the absence of the air waveguide. Figure 3 shows plots of η_1 and η_2 for each of our waveguide types as a function of time delay between the spark and filament laser pulses. Inspection of Fig. 1(a) shows that ~70% of the spark emission occurs before 500 ns, so the evolution of the peak signal and collection enhancements are largely characteristic of the waveguide evolution and not the source evolution. The spot images shown in Fig. 2 are for time delays where the collection efficiency is maximized for each waveguide. In general, we find $\eta_1 > \eta_2$, because the peak intensity enhancement is more spatially localized than the spot.

Figures 2 and 3 illustrate the acoustic and thermal regimes of guiding discussed earlier. Figures 2(b) and 2(c) [and

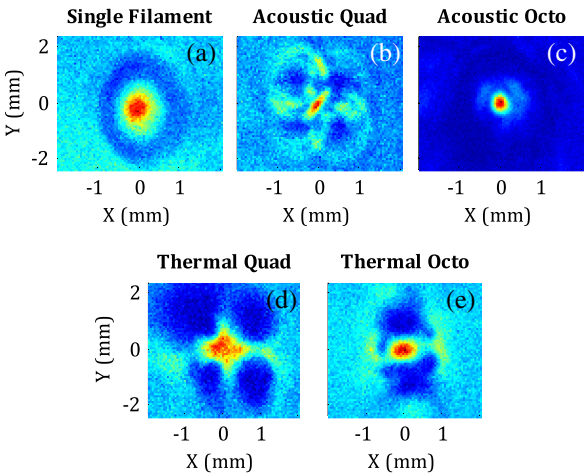

Fig. 2. Single-shot images of the breakdown spark light emerging from the exit of the guiding structures. (a) Single-filament-induced guide at 1.2 μs, (b) four-lobed acoustic guide at 3.2 μs, (c) eight-lobed acoustic guide at 1.4 μs, (d) four-lobed thermal guide at 250 μs, and (e) eight-lobed thermal guide at 100 μs.

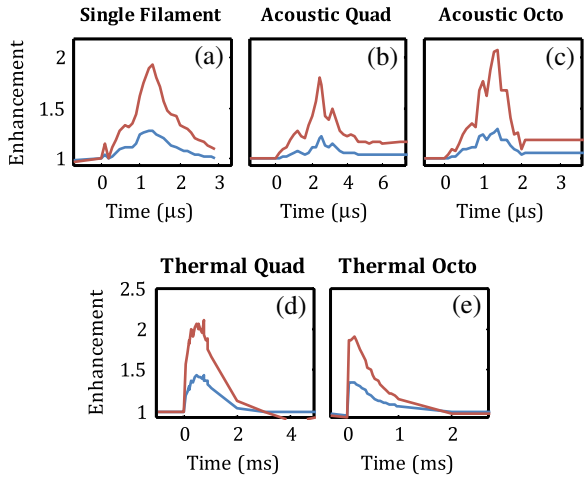

Fig. 3. Source collection enhancement (blue) and peak signal enhancement (red) plotted versus filament–spark source delay for (a) single-filament acoustic guide, (b) four-lobed acoustic guide, (c) eight-lobed acoustic guide, (d) four-lobed thermal guide, and (e) eight-lobed thermal guide.

Figs. 3(b) and 3(c)] illustrate microsecond-duration acoustic guiding in the waveguide formed by colliding sound waves from quad- and octo-filaments, while Figs. 2(d) and 2(e) [and Figs. 3(d) and 3(e)] illustrate the much longer duration thermal guiding from waveguide structures enabled by quad- and octo-density holes. The plots of peak and collection enhancement for the thermal guides show an almost 2 ms long collection window, ~10^3 times longer than for the acoustic guides. For a single filament [Figs. 2(a) and 3(a)], we also see source light trapping in a window ~1 μs long, where trapping occurs in the positive crest of the single-cycle annular acoustic wave launched in the wake of the filament [16]. Here, the trapping lifetime is constrained by the limited temporal window for source ray acceptance as the acoustic wave propagates outward from the filament.

For each of the guides we observe peak signal enhancement in the range $\eta_1 \sim 1.8$–2 and source collection enhancement $\eta_2 \sim 1.3$–1.5 [Figs. 2(a)–2(e) and Figs. 3(a)–3(e)]. For a waveguide of numerical aperture $\mathrm{NA} = \sqrt{2}(\delta n_{\mathrm{co}} - \delta n_{\mathrm{cl}})^{1/2}$ [14], where δn_{co} and δn_{cl} are the shifts in the air waveguide core and cladding refractive indices relative to undisturbed ambient air, respectively, the source collection enhancement is

$$\eta_2 = 4(\mathrm{NA})^2 \left(\frac{a_{\mathrm{in}}}{w}\right)^2 \left(\frac{L}{a_{\mathrm{out}}}\right)^2 \alpha, \qquad (1)$$

where L is the waveguide length, a_{in} and a_{out} are the mode diameters for the waveguide at the spark source and the output, respectively, w is the greater of the source diameter d_s and a_{in}, and α is a transient loss coefficient computed from a beam propagation method (BPM) [22] simulation (see below). For our octo-thermal guide we used burn paper to characterize the transverse profile of the guide and a microphone [16] to measure the axial extent. Similar to previous experiments [14], we find the mode diameter to be roughly half the lobe spacing. Parameters for the octo-thermal guide are $\mathrm{NA} \sim 2.5 \cdot 10^{-3}$,

$L = 1$ m, $a_{in} = 0.5$ mm, $a_{out} = 1.5$ mm, $d_s = 0.5$ mm, and $\alpha = 0.28$, resulting in $\eta_2 = 3$, which is in reasonable agreement with our measured $\eta_2 = 1.4$. Although the signal enhancement is modest for our meter-scale filament, the scaling $\eta_2 \propto L^2$ would enable an $\sim 10^4$ collection enhancement by a 100 m air waveguide.

For the BPM simulation, we used a paraxial portion of a spherical wave to simulate rays from a point source lensed by an eight-lobed thermal index structure with a peak index shift consistent with the NA used above. Greater than exponential losses are observed over the first meter as the lossiest leaky modes radiate out of the guide, factored into Eq. (1) through α as discussed above. Extending the propagation simulation from $\sim$1 to 100 m for either a constant or linearly tapered transverse profile (doubling over 100 m) gives similar results, showing that beyond 1 m, the losses transition to weakly exponential for the few weakly leaky modes remaining. After transient losses over the first meter, only 25% of the signal is lost over the remaining $\sim$99 m of transit, preserving the L^2 efficiency scaling. These results do not account for absorption in air.

Crucial to remote sensing schemes is identification of the source's chemical composition, which is typically done by identifying characteristic spectral lines of neutral atoms or ions of a given species. For such schemes, it is important that the emission spectrum at the source location be conveyed with high fidelity to the remote detector location. To investigate this property of our air waveguide, we compared spectra measured 10 cm from the air spark source to spectra of the guided signal collected from the output of the air waveguide. The results are shown in Fig. 4 for a thermal waveguide from a quad-filament, where the spectra have been averaged over 100 shots. There is no significant difference in the spectra except for attenuation in the range 700–900 nm due to signal transmission through a broadband 800 nm dielectric mirror, as depicted in Fig. 1, and the onset of UV absorption at less than $\sim$350 nm due to absorption by the BK7 substrate of the same mirror and in the following BK7 lenses. In addition to the characteristic nitrogen emission lines identified in Fig. 4, a very strong scattering peak is seen at 532 nm from the spark laser, with the spectral peak extending well past the range of the plot's vertical axis.

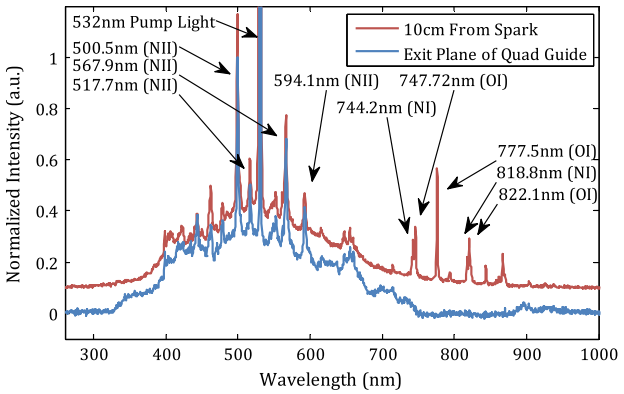

Fig. 4. Air spark spectrum collected near the source (red curve) and after transport in a 75 cm air waveguide (thermal guide from a quad-filament, blue curve). Characteristic lines are indicated on the spectrum. The red curve is raised for clarity. (Spectrometer: Ocean Optics HR2000+).

In conclusion, we have demonstrated that a femtosecond filament-generated air waveguide can be used as a remote broadband collection optic to enhance the signal in standoff measurements of remote source emission. This provides a new tool for dramatically improving the sensitivity of optical remote sensing schemes. By employing air waveguides of sufficient length, the signal-to-noise ratio in lidar and remote LIBS measurements can be increased by many orders of magnitude. Finally, we emphasize that air waveguides are dual purpose: not only can they collect and transport remote optical signals, but they can also guide high peak and average power laser drivers to excite those sources.

FUNDING INFORMATION

Air Force Office of Scientific Research (AFOSR); Defense Threat Reduction Agency (DTRA); National Science Foundation (NSF).

ACKNOWLEDGMENTS

The authors thank R. Birnbaum and S. Zahedpour for useful discussions and technical assistance.

REFERENCES

1. A. Couairon and A. Mysyrowicz, Phys. Rep. **441**, 47 (2007).
2. J. Kasparian, M. Rodriguez, G. Méjean, J. Yu, E. Salmon, H. Wille, R. Bourayou, S. Frey, Y.-B. André, A. Mysyrowicz, R. Sauerbrey, J.-P. Wolf, and L. Wöste, Science **301**, 61 (2003).
3. P. Rohwetter, J. Yu, G. Mejean, K. Stelmaszczyk, E. Salmon, J. Kasparian, J.-P. Wolf, and L. Wöste, J. Anal. At. Spectrom. **19**, 437 (2004).
4. J. Liu, J. Dai, S. L. Chin, and X.-C. Zhang, Nat. Photonics **4**, 627 (2010).
5. P. Sprangle, J. Peñano, B. Hafizi, D. Gordon, and M. Scully, Appl. Phys. Lett. **98**, 211102 (2011).
6. C. D'Amico, A. Houard, M. Franco, B. Prade, and A. Mysyrowicz, Phys. Rev. Lett. **98**, 235002 (2007).
7. K. Y. Kim, A. J. Taylor, J. H. Glownia, and G. Rodriguez, Nat. Photonics **2**, 605 (2008).
8. C. P. Hauri, W. Kornelis, F. W. Helbing, A. Heinrich, A. Couairon, A. Mysyrowicz, J. Biegert, and U. Keller, Appl. Phys. B **79**, 673 (2004).
9. G. Stibenz, N. Zhavoronkov, and G. Steinmeyer, Opt. Lett. **31**, 274 (2006).
10. A. Houard, C. D'Amico, Y. Liu, Y. B. Andre, M. Franco, B. Prade, A. Mysyrowicz, E. Salmon, P. Pierlot, and L.-M. Cleon, Appl. Phys. Lett. **90**, 171501 (2007).
11. M. Châteauneuf, S. Payeur, J. Dubois, and J.-C. Kieffer, Appl. Phys. Lett. **92**, 091104 (2008).
12. Y.-H. Cheng, J. K. Wahlstrand, N. Jhajj, and H. M. Milchberg, Opt. Express **21**, 4740 (2013).
13. N. Jhajj, Y.-H. Cheng, J. K. Wahlstrand, and H. M. Milchberg, Opt. Express **21**, 28980 (2013).
14. N. Jhajj, E. W. Rosenthal, R. Birnbaum, J. K. Wahlstrand, and H. M. Milchberg, Phys. Rev. X **4**, 011027 (2014).
15. S. Zahedpour, J. K. Wahlstrand, and H. M. Milchberg, Phys. Rev. Lett. **112**, 143601 (2014).
16. J. K. Wahlstrand, N. Jhajj, E. W. Rosenthal, S. Zahedpour, and H. M. Milchberg, Opt. Lett. **39**, 1290 (2014).
17. L. Levi, O. Lahav, R. A. Nemirovsky, J. Nemirovsky, I. Orr, I. Kaminer, M. Segev, and O. Cohen, "Long-lived waveguides and sound wave generation by laser filamentation," arXiv:1307.3588 (2013).

18. P. N. Malevich, D. Kartashov, Z. Pu, S. Ališauskas, A. Pugžlys, A. Baltuška, L. Giniūnas, R. Danielius, A. A. Lanin, A. M. Zheltikov, M. Marangoni, and G. Cerullo, Opt. Express **20**, 18784 (2012).
19. M. Scheller, M. Mills, M. Miri, W. Cheng, J. Maloney, M. Kolesik, P. Polynkin, and D. Christodoulides, Nat. Photonics **8**, 297 (2014).
20. S. Varma, Y.-H. Chen, J. P. Palastro, A. B. Fallahkair, E. W. Rosenthal, T. Antonsen, and H. M. Milchberg, Phys. Rev. A **86**, 023850 (2012).
21. J. Scaffidi, J. Pender, W. Pearman, S. R. Goode, B. W. Colston, J. C. Carter, and S. M. Angel, Appl. Opt. **42**, 6099 (2003).
22. M. D. Feit and J. Fleck, Appl. Opt. **17**, 3990 (1978).

Research Article Vol. 1, No. 1 / July 2014 / Optica 10

Microresonator frequency comb optical clock

Scott B. Papp,[1,*] Katja Beha,[1] Pascal Del'Haye,[1] Franklyn Quinlan,[1] Hansuek Lee,[2] Kerry J. Vahala,[2] and Scott A. Diddams[1]

[1]Time and Frequency Division 688, National Institute of Standards and Technology, Boulder, Colorado 80305, USA

[2]T. J. Watson Laboratory of Applied Physics, California Institute of Technology, Pasadena, California 91125, USA

*Corresponding author: scott.papp@nist.gov

Received 4 April 2014; revised 16 June 2014; accepted 17 June 2014 (Doc. ID 209505); published 22 July 2014

Optical frequency combs serve as the clockwork of optical clocks, which are now the best time-keeping systems in existence. The use of precise optical time and frequency technology in various applications beyond the research lab remains a significant challenge, but one that integrated microresonator technology is poised to address. Here, we report a silicon-chip-based microresonator comb optical clock that converts an optical frequency reference to a microwave signal. A comb spectrum with a 25 THz span is generated with a 2 mm diameter silica disk and broadening in nonlinear fiber. This spectrum is stabilized to rubidium frequency references separated by 3.5 THz by controlling two teeth 108 modes apart. The optical clock's output is the electronically countable 33 GHz microcomb line spacing, which features stability better than the rubidium transitions by the expected factor of 108. Our work demonstrates the comprehensive set of tools needed for interfacing microcombs to state-of-the-art optical clocks.

OCIS codes: (140.3945) Microcavities; (190.4410) Nonlinear optics, parametric processes; (230.4910) Oscillators.

http://dx.doi.org/10.1364/OPTICA.1.000010

1. INTRODUCTION

Optical frequency combs enable extraordinary measurement precision and accuracy entirely commensurate with their reference oscillator. A new direction in experiments is the creation of ultracompact combs via parametric nonlinear optics in microresonators [1,2]. We refer to these as microcombs, and here we report a silicon-chip-based microcomb optical clock that phase-coherently converts an optical reference to a microwave signal.

Optical clocks leverage the narrow, unvarying transitions of atoms to realize exceptionally stable laser frequencies measured at below the 10^{-17} level [3]. Optical frequency combs facilitate the measurement and use of these atomic references by providing a set of clock-referenced lines that span more than an octave [4]. Moreover, they have enabled advances in diverse fields from spectroscopy of atoms and molecules [5,6] to astronomy [7].

A new type of frequency comb has emerged based on optical microresonators [1,2]. Here, the comb generation relies on nonlinear parametric oscillation and cascaded four-wave mixing driven by a CW laser. Such microcombs offer revolutionary advantages over existing comb technology, including chip-based photonic integration, uniquely large comb-mode spacings in the tens of gigahertz range, and monolithic construction with small size and power consumption. Microcomb development has included frequency control of their spectra [8–11], characterization of their noise properties [12–14], a Rb-stabilized microcomb oscillator [15], and demonstration of phase-locked [12,16,17] and mode-locked states [18,19]. However, the milestone of all-optical frequency control of a microcomb to an atomic reference, including frequency division to the microwave domain, has not been achieved.

In this paper, we report the achievement of this goal by demonstrating a functional optical clock based on full stabilization of a microcomb to atomic Rb transitions. We generate a low-noise, continuously equidistant microcomb spectrum by use of an on-chip silica microresonator. The clock output is the 33 GHz microcomb line spacing, which is electronically measurable, and a traceable integer partition of the 3.5 THz frequency spacing of the Rb references. Here, we explore the basic features of this microcomb clock. Its 5×10^{-9} Allan

deviation for 1 s averaging is completely dominated by the Rb reference, and the microcomb contribution is only $<2 \times 10^{-14}$ at 1 s, indicating that much more stable clocks could be supported. Our results highlight an architecture for the integration of microcombs with other high-performance and chip-scale atomic frequency references [20].

2. EXPERIMENTAL METHODS

Figure 1(a) shows a schematic of our microcomb optical clock. A 2 mm diameter disk resonator with a 10° wedge side profile provides parametric comb generation. The resonator, which has an unloaded quality factor of 63 million, is fabricated on a silicon chip using conventional semiconductor fabrication techniques [21]. Hence, the core of our system is scalable and could be integrated with other on-chip photonic elements, and eventually atomic systems [20,22]. In these experiments we use a tapered fiber for evanescent coupling [23]. We excite the disk resonator with light from a CW laser (optical frequency ν_p) that is intensity modulated at frequency f_{eo} and amplified to a maximum of 140 mW. The first-order sideband powers are approximately 3 dB lower than the pump, and the piece of highly nonlinear fiber (HNLF) before the disk resonator increases the second-order (third-order) sidebands to 12 (25) dB below the pump. The modulation implements our parametric seeding technique [11], which enables unmatched control of the microcomb line spacing. Here we further demonstrate that parametric seeding enables the complete suppression of undesirable, nonequidistant subcombs. Following generation in the disk resonator, the microcomb output is optically filtered to attenuate the pump laser and modulation sidebands; the resulting spectrum is shown by the top trace in Fig. 1(b). The microcomb bandwidth is approximately a factor of 10 higher than the seeding comb. By amplifying the microcomb spectrum and without any dispersion control, we broaden the initial 20 nm bandwidth an additional factor of 10 to 200 nm. The ~2 ps duration optical waveform obtained directly from the microresonator offers sufficient peak power for our experiments and is stable and repeatable even for different settings of pump frequency and power, intensity modulation, taper–resonator coupling, and pump polarization. The broadened spectrum [Fig. 1(b)] overlaps with the resonance frequencies of molecules such as HCN, C_2H_2, CO_2, CH_4, and atomic Rb and K after second-harmonic generation.

For frequency stabilization, we heterodyne the microcomb spectrum with telecom-grade semiconductor distributed feedback (DFB) lasers at 1560 and 1590 nm. These lasers are frequency doubled and stabilized to well-known Rb transitions [24–26]. Precise Rb spectroscopic data, especially near 780 nm, exist, and with attention to systematic effects a stability of $10^{-12}/\sqrt{\tau}$ has been demonstrated [24]. Therefore, we focus only on salient details for controlling the microcomb with these optical references. To operate an optical clock, we stabilize the microcomb's two *independent* degrees of freedom to the Rb references by leveraging frequency control of its spectrum. The central line of the microcomb is phase locked to the 1560 nm DFB laser, which is separate from the pump laser. [9,15]. Additionally, the 108th comb line from the center, which we obtain via spectral broadening, is phase locked to the 1590 nm DFB laser by tuning the microcomb line spacing through control of f_{eo}.

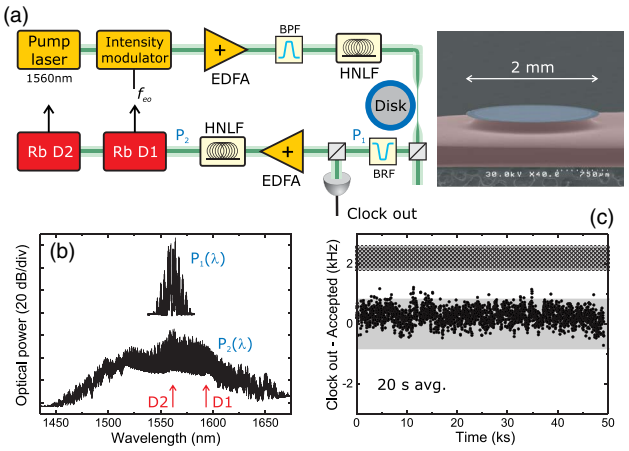

Fig. 1. Microcomb optical clock with Rb atoms. (a) An intensity-modulated pump laser excites a chip-based microresonator (see micrograph at right) to create a 33 GHz spacing comb. The comb is broadened in highly nonlinear fiber (HNLF) following amplification to 1.4 W. Two lines of the comb 108 modes apart are stabilized to Rb transitions by control of the pump frequency and the intensity modulation f_{eo}. The clock output is obtained via photodetection of the unbroadened spectrum. Not shown are polarization controllers, which are needed before the intensity modulator, the microresonator, the HNLF, and all the elements of the Rb spectrometers. Other components are an optical bandpass filter (BPF), a bandreject filter (BRF), and two erbium-doped fiber amplifiers (EDFA). (b) Optical spectrum after a filter to suppress the pump (top) and following spectral broadening (bottom), (c) optical clock output over 12 h. Each point is the average of twenty 1 s measurements. For comparison, published Rb spectroscopic data on the D2–D1 difference divided by 108 has been subtracted. The solid [25] and hatched [26] gray regions represent previous data.

3. RESULTS AND DISCUSSION

The output of our microcomb optical clock is obtained via photodetection of the $\Delta\nu = 32.9819213$ GHz line spacing, which reflects the frequency difference Δ_{Rb} of the D2- and D1-stabilized lasers divided by 108, and a fixed 660/108 MHz offset for phase stabilization. This specific offset arises because the comb's central mode is phase locked at a frequency 920 MHz higher than the 1560 nm laser, while mode 108 is phase locked 260 MHz higher than the 1590 nm laser. The offset could assume a range of predetermined values, including zero, and the microresonator free spectral range could be targeted to utilize a specific value. The data points in Fig. 1(c) are a continuous >12 h long record of the clock output. Here, the vertical axis shows the difference between the clock output and $\Delta_{Rb} = 3,561,387,470(180)$ kHz, whose uncertainty [24–26] is shown by the gray band. Although we have not systematically analyzed the accuracy of our clock, its output is in reasonable agreement with these previous data. The 271 Hz RMS fluctuation in a 20 s average of the clock output is significantly reduced from those of the D2 and D1 reference lasers, due to the principle of optical frequency division associated with

frequency combs [4,27,28]. The remainder of this paper presents an investigation of our clock, including the deterministic generation of an equidistant microcomb spectrum, a demonstration of the precise relationship between the clock output and Rb reference, and an analysis of the clock's stability.

The essential aspect of a frequency comb is a uniform spacing of all its modes. However, microcomb spectra are often composed of overlapping subcombs with different offset frequencies [29]. Such a microcomb spectrum has a fundamentally reduced frequency measurement precision and is unusable for our optical clock experiment. Subcombs arise when parametric oscillation creates initial signal/idler fields in resonator modes $\pm m_i$ away from the one excited by the pump laser. The green lines in Fig. 2(a) show a schematic of a subcomb with characteristic frequency offset from that of an equidistant comb given by $\nu_0 = n_1(\Delta P - m_i \Delta\nu)$, where $\Delta P \approx m_i \Delta\nu$ is the primary spacing with order n_1. We use a coherent control technique, parametric seeding, to deterministically suppress subcombs and favor a continuous comb with a single offset frequency. The seeding comb, whose spectrum $\nu_m = \nu_p + m f_{eo}$ is shown by the red lines in Fig. 2(a), experiences parametric gain in the microresonator, and it induces sidebands of the first signal/idler pair that fix $\Delta\nu$ of all parametrically generated lines at f_{eo}. In this paper, we demonstrate for the first time (to our knowledge) that sufficient amplitude of the seeding comb $\nu_{\pm m_i}$ modes can injection lock the subcomb, which completely nullifies its frequency offset ν_0.

To investigate subcomb injection-locking (Fig. 2), we monitor the amplitudes of subcomb and parametric seeding comb lines while we tune f_{eo}, and thus ν_0. Information about these amplitudes is obtained via photodetection of the entire microcomb spectrum, which yields a signal at frequency $\Delta\nu$ and its sidebands associated with ν_0; see the schematic in Fig. 2(b). The measurement of RF power versus frequency in Fig. 2(c) shows $\Delta\nu$ and ν_0, including its four-wave mixing harmonics. By recording many such traces for different settings of f_{eo}, we explore the transition into and out of injection-locked operation; Fig. 2(d) presents a false color "waterfall" plot of these data. Here the horizontal band at zero is the microcomb line spacing, which is always f_{eo}, and the other bands are associated with the subcomb offset. As the offset is tuned toward zero via a computer-controlled scan of f_{eo} in 1.7 kHz increments, we observe an abrupt suppression of the subcomb RF components. This represents the point at which the line frequencies of the seeding comb and subcomb are sufficiently close to capture the latter. A linear fit of the first-order offset signals yields the f_{eo} setting (this fit establishes f_{lock}) for $\nu_0 = 0$, which is used to calibrate the horizontal axis of Fig. 2(d), and the slope, which corresponds to m_i. The injection-locking range is 400 kHz, in which the RF frequencies associated with the subcomb offset are suppressed by >40 dB; see Fig. 2(c). In future experiments, such a large locking range would enable a direct harmonic relationship between Δ_{Rb} and $\Delta\nu$. Following initiation of the injection-locked state, the microcomb's spectrum is equidistant and offset free and can operate continuously for >24 h. (The seeding must remain on.) We verify the equidistance of the central 110 lines of the broadened microcomb spectrum by use of a calibrated reference system [11].

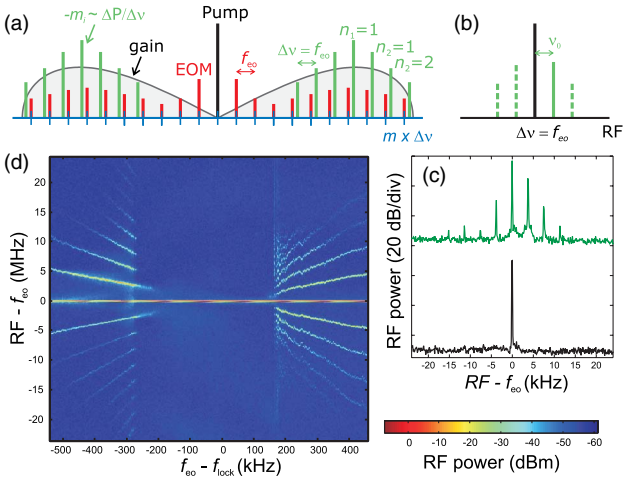

Fig. 2. Injection locking to create an equidistant microcomb. (a) Model for microcomb generation, including a subcomb (green) and parametric seeding (red), (b) model RF spectrum after photodetection. All the comb lines contribute at frequency $\Delta\nu = f_{eo}$, and the presence of a subcomb is reflected in the sidebands spaced by ν_0. (c) Measured RF spectra with a 100 kHz resolution bandwidth, indicating a subcomb (top, green) with $\nu_0 \approx 4$ MHz at $f_{eo} - f_{lock} = -387$ kHz and an injection-locked comb (bottom, black) at $f_{eo} = f_{lock}$, (d) waterfall plot compiled from many traces like those in (c). The false color bar shows the scaling of RF power.

Our microcomb optical clock is designed to generate an electronically detectable microwave output at a precise *integer* subdivision of the Rb reference. In contrast to earlier work [15], the clock output is traceable to atomic structure without regard to the operating parameters or conditions of the microcomb. To test this principle, we simultaneously count the DFB lasers' frequencies and the clock output and characterize their degree of correlation. The frequencies are recorded in nearly continuous 1 s intervals by use of an auxiliary self-referenced and repetition-rate-stabilized Er:fiber frequency comb [30]. In Fig. 3(a), the black points show the clock output, while the red open points are $\Delta_{Rb}/108$. Since the difference of the DFB lasers is not calibrated, for clarity we subtract its mean value $\bar{\Delta}_{Rb}/108$ from all the points. The overlap of the two data sets suggests their correlation, which we analyze in more detail by plotting them against each other; see Fig. 3(b). A linear fit of this correlation plot yields a slope of 108.0002(59), and the horizontal intercept differs from zero by only -2.4 ± 1.5 Hz, compared to the ~3.5 THz frequency of the Rb reference. Knowledge of Δ_{Rb} via the stabilized fiber comb enables us to compare the clock signal with its optical reference in real time. Figure 3(c) shows a frequency counter record of the clock output from the same dataset as in Fig. 1(c), but here at each point a correction for the noise of the Rb spectrometers is applied. This reduces the scale of clock fluctuations by a factor of ~1000 to the hertz level and demonstrates that they are overwhelmingly determined by the Rb reference.

We expect the microcomb clock output will closely reproduce the frequency stability of the Rb references. To characterize them, we record the optical heterodyne frequency of the microcomb and the 1590 nm laser, while the microcomb's

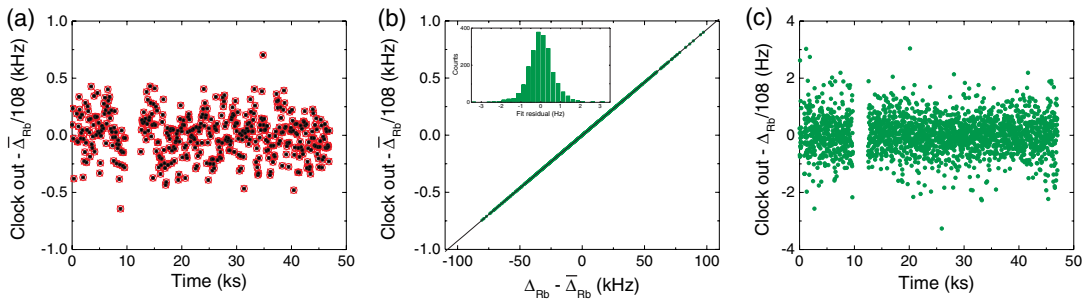

Fig. 3. Subdivision of the 3.5 THz Rb reference. (a) Clock output (black points) and difference of the Rb-stabilized DFB lasers (red circles) minus the mean of all Δ_{Rb} measurements. Here, 100-sample mean values of the 1 s gate data are displayed. (b) Strong correlation of clock output and the terahertz frequency of the Rb reference. The inset shows a histogram of the fit residuals. (c) Real-time-corrected clock output with 0.64 Hz standard deviation. During the gap in measurements at 10 ks, the fiber comb was unlocked.

central line is phase locked to the 1560 nm laser. For this experiment, the phase lock to the 1590 nm laser is switched off and a constant parametric seeding frequency, which is synthesized from a hydrogen maser, determines the microcomb line spacing. The open circles in Fig. 4 show the combined Allan deviation of the Rb references normalized to 33 GHz for six decades of integration time. For short measurement periods the stability increases as approximately $1/\sqrt{\tau}$. However near 0.1 s the Allan deviation increases and only slowly improves for averaging periods up to 10,000 s. The impact of systematic drifts on the Rb transitions due to, for example, excitation laser power fluctuations, magnetic field noise, and the Rb vapor cell pressure has been discussed extensively in the literature [24]. Importantly, these effects, rather than any associated with the microcomb, explain the references' stability.

With microcomb servo control via the Rb D1 reference restored, we analyze the clock output by way of its Allan deviation, which is obtained with respect to a synthesized 33 GHz frequency referenced to a hydrogen maser. Importantly, the clock's stability (filled black points in Fig. 4) is improved by a factor of ~100 over that of the DFB lasers, whose noise is distributed among all the lines of the microcomb. Such

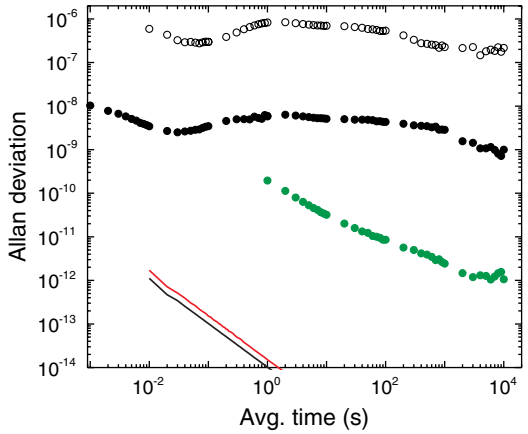

Fig. 4. Microcomb optical clock stability. Allan deviation of the DFB lasers (open points) and the microcomb clock (closed black points) normalized to a 33 GHz carrier. The green points are the clock stability after correcting the Rb reference noise via measurements against an auxiliary comb. The red and black traces represent the in-loop residual noise for stabilization of the microcomb pump laser and mode 108, respectively.

optical frequency division is the key metrological feature of any comb. Fluctuations and inaccuracy of the Rb-referenced lasers are naturally reflected in the microcomb clock output, and this explains the slow averaging of the black filled points in Fig. 4 beyond ~0.1 s. On the other hand, the in-loop noise of the two servos that stabilize the microcomb, which are shown by the black and red traces in Fig. 4, indicate that our microcomb system as currently configured could support more stable frequency references, and hence produce a 33 GHz output with a 1 s fractional stability of 2×10^{-14}. Increasing the bandwidth of the servo loops, in particular by shortening the second HNLF, would improve residual noise. We demonstrate this potential for improvement by characterizing the clock output, including its real-time correction for Rb reference noise [Fig. 3(c)]. The green points in Fig. 4 show an upper limit for the corrected clock output's Allan deviation, which monotonically decreases with averaging time to 10^{-12} at 10,000 s. Accordingly, we project that a microcomb utilizing compact, all-optical Rb frequency references in a controlled environment [24] could produce a 33 GHz output with $5 \times 10^{-11}/\sqrt{\tau}$ stability.

4. CONCLUSION

In conclusion, we have reported the all-optical stabilization of a chip-based microresonator frequency comb to atomic Rb transitions. The electronically detectable microwave output of our optical clock is stable, and it accurately subdivides the terahertz frequency difference of the Rb references. At present the clock output stability is limited entirely by the Rb references. However, the microcomb frequency control architecture demonstrated here is sufficient to support references with orders-of-magnitude-higher performance. Future work will address this point, as well as focus on generation of higher-peak-power optical waveforms directly from the microcomb. Combined with nonlinear spectral broadening, this would enable the subdivision of even larger frequency gaps and ultimately the self-referencing of a microcomb.

FUNDING INFORMATION

Defense Advanced Research Projects Agency (DARPA) (PULSE, QuASAR), National Aeronautics and Space Administration (NASA), Air Force Office of Scientific Research (AFOSR), and Kavli NanoScience Institute at Caltech.

ACKNOWLEDGMENTS

We thank Elizabeth Donley and Andrew Ludlow for thoughtful comments on this manuscript and M. Hirano for supplying the HNLF. It is a contribution of the U.S. government (NIST) and is not subject to copyright in the United States of America.

REFERENCES

1. P. Del'Haye, A. Schliesser, O. Arcizet, T. Wilken, R. Holzwarth, and T. J. Kippenberg, "Optical frequency comb generation from a monolithic microresonator," Nature **450**, 1214–1217 (2007).
2. T. J. Kippenberg, R. Holzwarth, and S. A. Diddams, "Microresonator-based optical frequency combs," Science **332**, 555–559 (2011).
3. N. Hinkley, J. A. Sherman, N. B. Phillips, M. Schioppo, N. D. Lemke, K. Beloy, M. Pizzocaro, C. W. Oates, and A. D. Ludlow, "An atomic clock with 10^{-18} instability," Science **341**, 1215–1218 (2013).
4. S. A. Diddams, T. Udem, J. C. Bergquist, E. A. Curtis, R. E. Drullinger, L. Hollberg, W. M. Itano, W. D. Lee, C. W. Oates, K. R. Vogel, and D. J. Wineland, "An optical clock based on a single trapped $^{199}Hg^{+}$ ion," Science **293**, 825–828 (2001).
5. K.-K. Ni, S. Ospelkaus, M. H. G. de Miranda, A. Pe'er, B. Neyenhuis, J. J. Zirbel, S. Kotochigova, P. S. Julienne, D. S. Jin, and J. Ye, "A high phase-space-density gas of polar molecules," Science **322**, 231–235 (2008).
6. M. J. Thorpe, K. D. Moll, R. J. Jones, B. Safdi, and J. Ye, "Broadband cavity ringdown spectroscopy for sensitive and rapid molecular detection," Science **311**, 1595–1599 (2006).
7. M. T. Murphy, T. Udem, R. Holzwarth, A. Sizmann, L. P. C. Araujo-Hauck, H. Dekker, S. D'Odorico, M. Fischer, T. W. Hansch, and A. Manescau, "High-precision wavelength calibration of astronomical spectrographs with laser frequency combs," Mon. Not. R. Astron. Soc. **380**, 839–847 (2007).
8. P. Del'Haye, O. Arcizet, A. Schliesser, R. Holzwarth, and T. J. Kippenberg, "Full stabilization of a microresonator-based optical frequency comb," Phys. Rev. Lett. **101**, 053903 (2008).
9. S. B. Papp, P. Del'Haye, and S. A. Diddams, "Mechanical control of a microrod-resonator optical frequency comb," Phys. Rev. X **3**, 031003 (2013).
10. P. Del'Haye, S. B. Papp, and S. A. Diddams, "Hybrid electro-optically modulated microcombs," Phys. Rev. Lett. **109**, 263901 (2012).
11. S. B. Papp, P. Del'Haye, and S. A. Diddams, "Parametric seeding of a microresonator optical frequency comb," Opt. Express **21**, 17615–17624 (2013).
12. S. B. Papp and S. A. Diddams, "Spectral and temporal characterization of a fused-quartz-microresonator optical frequency comb," Phys. Rev. A **84**, 053833 (2011).
13. A. A. Savchenkov, E. Rubiola, A. B. Matsko, V. S. Ilchenko, and L. Maleki, "Phase noise of whispering gallery photonic hyperparametric microwave oscillators," Opt. Express **16**, 4130–4144 (2008).
14. J. Li, H. Lee, T. Chen, and K. J. Vahala, "Low-pump-power, low-phase-noise, and microwave to millimeter-wave repetition rate operation in microcombs," Phys. Rev. Lett. **109**, 233901 (2012).
15. A. A. Savchenkov, D. Eliyahu, W. Liang, V. S. Ilchenko, J. Byrd, A. B. Matsko, D. Seidel, and L. Maleki, "Stabilization of a Kerr frequency comb oscillator," Opt. Lett. **38**, 2636–2639 (2013).
16. F. Ferdous, H. Miao, D. E. Leaird, K. Srinivasan, J. Wang, L. Chen, L. T. Varghese, and A. M. Weiner, "Spectral line-by-line pulse shaping of on-chip microresonator frequency combs," Nat. Photonics **5**, 770–776 (2011).
17. P. Del'Haye, K. Beha, S. B. Papp, and S. A. Diddams, "Self-Injection locking and phase-locked states in microresonator-based optical frequency combs," Phys. Rev. Lett. **112**, 043905 (2014).
18. T. Herr, V. Brasch, J. D. Jost, C. Y. Wang, N. M. Kondratiev, M. L. Gorodetsky, and T. J. Kippenberg, "Temporal solitons in optical microresonators," Nat. Photonics **8**, 145–152 (2014).
19. K. Saha, Y. Okawachi, B. Shim, J. S. Levy, R. Salem, A. R. Johnson, M. A. Foster, M. R. E. Lamont, M. Lipson, and A. L. Gaeta, "Modelocking and femtosecond pulse generation in chip-based frequency combs," Opt. Express **21**, 1335–1343 (2013).
20. S. Knappe, V. Gerginov, P. D. D. Schwindt, V. Shah, H. G. Robinson, L. Hollberg, and J. Kitching, "Atomic vapor cells for chip-scale atomic clocks with improved long-term frequency stability," Opt. Lett. **30**, 2351–2353 (2005).
21. H. Lee, T. Chen, J. Li, K. Y. Yang, S. Jeon, O. Painter, and K. J. Vahala, "Chemically etched ultrahigh-*Q* wedge-resonator on a silicon chip," Nat. Photonics **6**, 369–373 (2012).
22. W. Yang, D. B. Conkey, B. Wu, D. Yin, A. R. Hawkins, and H. Schmidt, "Atomic spectroscopy on a chip," Nat. Photonics **1**, 331–335 (2007).
23. M. Cai, O. Painter, and K. J. Vahala, "Observation of critical coupling in a fiber taper to silica-microsphere whispering gallery mode system," Phys. Rev. Lett. **85**, 74–77 (2000).
24. J. Ye, S. Swartz, P. Jungner, and J. L. Hall, "Hyperfine structure and absolute frequency of the ^{87}Rb $5P_{3/2}$ state," Opt. Lett. **21**, 1280–1282 (1996).
25. A. Marian, M. C. Stowe, J. R. Lawall, D. Felinto, and J. Ye, "United time-frequency spectroscopy for dynamics and global structure," Science **306**, 2063–2068 (2004).
26. M. Maric, J. J. McFerran, and A. N. Luiten, "Frequency-comb spectroscopy of the D1 line in laser-cooled rubidium," Phys. Rev. A **77**, 32502 (2008).
27. W. C. Swann, E. Baumann, F. R. Giorgetta, and N. R. Newbury, "Microwave generation with low residual phase noise from a femtosecond fiber laser with an intracavity electro-optic modulator," Opt. Express **19**, 24387–24395 (2011).
28. T. M. Fortier, M. S. Kirchner, F. Quinlan, J. Taylor, J. C. Bergquist, T. Rosenband, N. Lemke, A. Ludlow, Y. Jiang, C. W. Oates, and S. A. Diddams, "Generation of ultrastable microwaves via optical frequency division," Nat. Photonics **5**, 425–429 (2011).
29. T. Herr, K. Hartinger, J. Riemensberger, W. C. Y. E. Gavartin, R. L. Holzwarth, M. Gorodetsky, and T. J. Kippenberg, "Universal formation dynamics and noise of Kerr-frequency combs in microresonators," Nat. Photonics **6**, 480–487 (2012).
30. F. Quinlan, T. M. Fortier, M. S. Kirchner, J. A. Taylor, M. J. Thorpe, N. Lemke, A. D. Ludlow, Y. Jiang, and S. A. Diddams, "Ultralow phase noise microwave generation with an Er:fiber-based optical frequency divider," Opt. Lett. **36**, 3260–3262 (2011).

Research Article Vol. 1, No. 1 / July 2014 / Optica 15

The Nyquist laser

MASATAKA NAKAZAWA,* MASATO YOSHIDA, AND TOSHIHIKO HIROOKA

Research Institute of Electrical Communication, Tohoku University, 2-1-1 Katahira, Aoba-ku, Sendai-shi, Miyagi-ken 980-8577, Japan

**Corresponding author: nakazawa@riec.tohoku.ac.jp*

Received 7 April 2014; revised 30 May 2014; accepted 10 June 2014 (Doc. ID 209725); published 22 July 2014

Nyquist pulses, which are defined as impulse responses of a Nyquist filter, can be used to simultaneously achieve an ultrahigh data rate and spectral efficiency (SE). Coherent Nyquist optical time-division multiplexing transmission increases SE, but the optical signal-to-noise ratio (OSNR) is limited by the amplitude of the original CW beam. To further improve transmission performance, here we describe a new pulsed laser that can emit an optical Nyquist pulse train at a repetition rate of 40 GHz. The Nyquist laser is based on a regeneratively and harmonically mode-locked erbium fiber laser that has a special spectral filter to generate a Nyquist pulse as the output pulse. The pulse width was approximately 3 ps, and the oscillation wavelength was 1.55 μm. The spectral profile of the Nyquist pulse can be changed by changing the spectral curvature of the filter with a roll-off factor, α, between 0 and 1. A Fabry–Perot etalon was also installed in the laser cavity to select longitudinal modes with a free spectral range of 40 GHz, resulting in the suppression of the mode hopping in the regenerative mode locking. A numerical analysis is also presented to explain the generation of a stable Nyquist pulse from the laser. The Nyquist laser is important not only for the direct generation of high-OSNR pulses but also for scientific advances, proving that pulse shapes that differ significantly from the conventional hyperbolic-secant and Gaussian pulse shapes can exist stably in a cavity. © 2014 Optical Society of America

OCIS codes: (140.4050) Mode-locked lasers; (140.3510) Lasers, fiber; (140.3500) Lasers, erbium; (140.7090) Ultrafast lasers; (320.5540) Pulse shaping; (060.1660) Coherent communications.

http://dx.doi.org/10.1364/OPTICA.1.000015

1. INTRODUCTION

Intensive efforts have been made to increase spectral efficiency (SE) by adopting a coherent multilevel modulation format, such as quadrature amplitude modulation (QAM) or orthogonal frequency-division multiplexing [1,2]. We recently reported 1024 and 2048 QAM digital coherent transmission experiments and showed a potential SE of more than 14 bit/s/Hz [3,4]. To increase the transmission speed in such a system, we recently proposed a Nyquist pulse that is given by the impulse response of a Nyquist filter [5]. An optical Nyquist pulse was first generated by spectrally filtering a Gaussian pulse, and it was used for optical time-division multiplexing (OTDM) transmission [5,6]. The Nyquist pulse enables us to reduce bandwidth without causing intersymbol interference. The SE was improved from 0.5 to 1.5 bit/s/Hz under differential phase shift keying transmission over 525 km, and we showed that the Nyquist pulse was robust against high-order dispersion and polarization-mode dispersion [6,7].

To further increase the SE, coherent Nyquist OTDM transmission was proposed, where a CW frequency-stabilized laser followed by a combination of sideband generation using a phase modulator and spectral filtering made it possible to generate a coherent Nyquist pulse [8]. Thus, we successfully demonstrated 1.92 Tbit/s/channel, 64 QAM coherent Nyquist transmission over 150 km, where the SE was increased to 7.5 bit/s/Hz [8]. However, to improve the transmission performance of the coherent Nyquist transmission, it is important to increase the optical signal-to-noise ratio (OSNR) of the coherent Nyquist pulse, which is usually limited by the amplitude of the original CW beam.

In this paper, we propose a Nyquist laser that can directly emit a coherent Nyquist pulse with a high OSNR. To generate

2334-2536/14/010015-08$15/0$15.00 © 2014 Optical Society of America

such a pulse train, we based our approach on our regeneratively and harmonically mode-locked erbium fiber laser at a wavelength of 1.55 μm [9]. We suppressed mode hopping by installing a Fabry–Perot etalon to select longitudinal modes with a free spectral range (FSR) of 40 GHz. The shape of the Nyquist pulse was varied by changing the spectral curvature of the filter installed in the cavity, which depended on a roll-off factor α of between 0 and 1. The installation of a special optical filter plays an important role in generating the Nyquist pulse, as it can control the amplitude and phase of each longitudinal mode.

2. CONFIGURATION OF THE NYQUIST LASER

Mode-locking techniques have generally been used to generate a transform-limited Gaussian or sech pulse train [10]. In amplitude modulation (AM) mode locking, parabolic time-domain shaping near the top of a sinusoidal amplitude modulation gives rise to a stable Gaussian pulse. When we introduce an optical nonlinear effect such as self-phase modulation (SPM) into a laser cavity under anomalous dispersion, the laser starts to emit a sech pulse described by the nonlinear Schrödinger equation. This is called a soliton laser [11]. Interesting schemes for mode locking such as interferential mode locking [12], additive pulse mode locking [13] and Kerr-lens mode locking [14] have also appeared. In FM mode locking, we employ a pulse formation mechanism combined with frequency chirping using a phase modulator and an optical bandpass filter. Here, the up or down linear chirping part of the sinusoidal phase modulation generates a linear chirping, and the two frequency components outside the optical bandpass filter can be removed. In other words, a combination of linear chirping and an optical bandpass filter in the cavity converts a CW wave into a pulse. Since this pulse-shaping mechanism exists with both up and down chirping, the FM mode locking is usually unstable unless cavity dispersion is introduced. For example, a stable FM mode-locked soliton laser uses up-chirping to counterbalance the anomalous dispersion during the course of soliton formation, and we can even accelerate up-chirping, which has the same chirping slope as SPM, for shorter soliton pulse generation. All these stable pulse formations in AM and FM mode locking were proven analytically in the 1970s, for example, by Kuizenga and Siegman [15,16], and Haus [17].

On the other hand, the Nyquist pulse is an entirely new pulse that has neatly repetitive ringing on the pulse tail. Therefore, we need a new mechanism to generate such ringing, which can be realized by installing a Nyquist optical filter as follows. The spectral profile of the raised-cosine Nyquist filter, $R(f)$, and its impulse response, $r(t)$, are given by

$$R(f) = \begin{cases} T, & 0 \le |f| \le \frac{1-\alpha}{2T} \\ \frac{T}{2}\left\{1 - \sin\left[\frac{\pi}{2\alpha}(2T|f| - 1)\right]\right\}, & \frac{1-\alpha}{2T} \le |f| \le \frac{1+\alpha}{2T}, \\ 0, & |f| \ge \frac{1+\alpha}{2T} \end{cases}$$

$$r(t) = \frac{\sin(\pi t/T)}{\pi t/T}\frac{\cos(\alpha\pi t/T)}{1 - (2\alpha t/T)^2}, \quad \textbf{(1)}$$

where T is the symbol period and α ($0 \le \alpha \le 1$) is known as a roll-off factor [18]. A Nyquist pulse, which depends on the value of α, accompanies its specific ringing feature (or ripples) on the wing of the pulse. Therefore, to generate such a pulse, we need not only pulse shaping at the pulse peak (parabolic time-domain shaping by using an optical intensity modulator) but also shaping on the wing. Since it is not easy to introduce time-domain shaping on the wing of the pulse, we use spectral-domain shaping by incorporating spectrum manipulation based on a liquid-crystal-on-silicon (LCoS) spatial modulator [19], which can precisely control both spectral amplitude and its phase. Dark and bright pulses were generated in a passively mode-locked laser with LCoS in the cavity [20]. Ultrashort pulses were also generated with an intracavity phase-shaping element [21]. Furthermore, it is important to note that simply the installation of an ideal Nyquist filter does not produce an ideal Nyquist pulse as an output. That is, the output spectral profile (flattop spectral profile for the Nyquist pulse) is given by the product of a Gaussian-like convex spectral profile generated by parabolic shaping in the time domain and a concave spectral profile, which is newly introduced by, for example, an LCoS filter [19].

The experimental setup of the Nyquist laser is shown in Fig. 1(a), where we adopted regenerative and harmonic mode locking in a fiber laser with a total cavity length of 17 m. The fiber cavity consists of a 5 m long polarization-maintaining erbium-doped fiber (PM-EDF), a 30% output coupler, an optical etalon, a polarization-dependent isolator, a $LiNbO_3$ Mach–Zehnder intensity modulator, an LCoS filter, and a WDM coupler with fiber pig-tails. The LCoS filter can manipulate the spectrum with a frequency resolution of 1 GHz over the C band, and the intensity can be controlled over a range of 35 dB with a precision of 0.1 dB. All the fibers in the cavity were polarization-maintaining fibers to prevent polarization fluctuations. In addition, all the fibers and the LCoS filter had anomalous dispersions. The average cavity dispersion characteristic is shown in Fig. 1(b), where the laser cavity had an anomalous dispersion of 28.9 ps/km/nm at 1550 nm. The dispersion characteristic was obtained with a group delay time measurement by changing the peak oscillation wavelength and detecting the corresponding pulse delay under an ordinary regenerative mode-locking condition. The pumping source was a 1.48 μm InGaAsP laser diode. We installed an optical etalon with an FSR of 40 GHz and a finesse of 200 to suppress mode hopping. The insertion loss of the etalon was 3 dB, and the total cavity loss was approximately 15 dB, which was easily compensated for by the erbium-doped fiber amplifier (EDFA). The fundamental cavity mode spacing was 12 MHz, and we set the repetition rate in the harmonic mode locking at 40 GHz. To obtain a sinusoidal harmonic beat signal at 40 GHz between the longitudinal laser modes, part of the output beam was coupled into a clock extraction circuit consisting of a high-speed photodetector, a 40 GHz high-Q dielectric filter ($Q \sim 1200$), and a high-gain electrical amplifier. After adjusting the phase between the pulse and the modulation peak, the beat signal was amplified and fed back to the intensity modulator in the cavity, resulting in regenerative mode locking [9]. The dispersion of the output pulse thus obtained

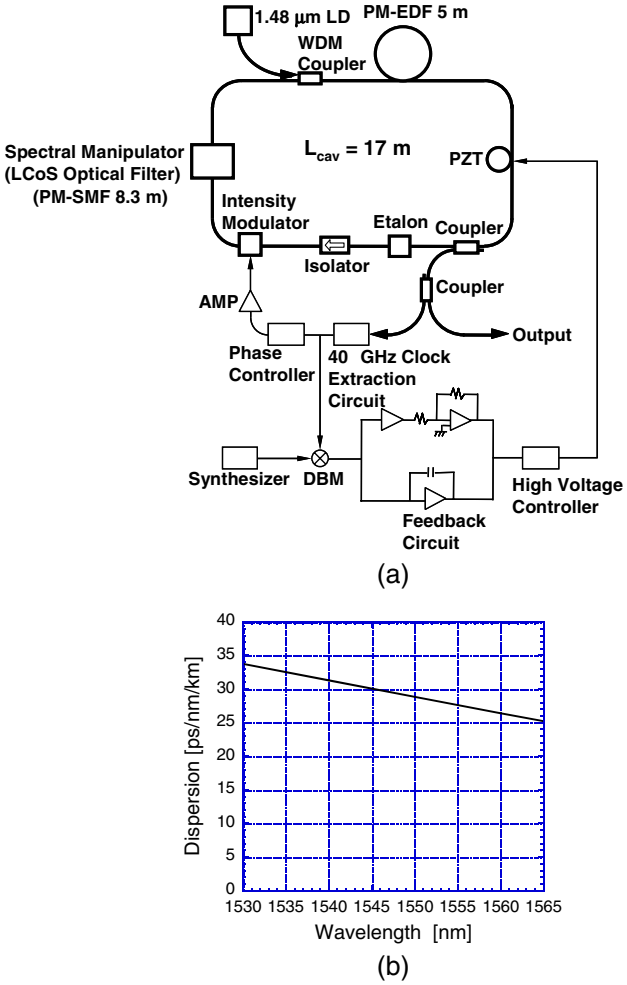

Fig. 1. (a) Experimental setup of the Nyquist laser and (b) average cavity dispersion characteristics. A $LiNbO_3$ Mach–Zehnder intensity modulator and a single LCoS spectral filter were installed in the cavity. A PLL operation was also adopted to keep the repetition rate at 40 GHz. PM-SMF, polarization-maintaining single-mode fiber; PZT, piezoelectric transducer; AMP, amplifier; DBM, double-balanced mixer.

was compensated for with appropriate opposite dispersion generated from a tunable grating-pair dispersion compensator. The output pulse was measured with an optical sampling scope with a resolution of 800 fs.

A $LiNbO_3$ Mach–Zehnder intensity modulator was used for parabolic intensity modulation. An LCoS spectral filter in the cavity plays an important role in changing the roll-off factor α. The resolution of the spectral manipulation was 1 GHz, but in our experiment one spectral slot was set at a bandwidth of 40 GHz. That is, if the aim is to apply the Nyquist laser to coherent optical communication, no longitudinal mode of the laser should fluctuate with time. Therefore, we installed a Fabry–Perot etalon to suppress the mode-hopping effect in the harmonic mode locking [22]. LCoS enabled us to modify the spectral curvature to obtain the Nyquist pulse. A phase-locked loop (PLL) operation was also adopted to keep the repetition rate constant at 40 GHz [23].

3. OUTPUT CHARACTERISTICS

The output power of the Nyquist laser as a function of the pump power is shown in Fig. 2(a), where the pump threshold was 30 mW and the slope efficiency was 8.1%. An output power of 15 mW was obtained at a pump power of 220 mW. The electrical spectrum of the output pulse train, which was detected with a high-speed photodetector, is shown in Fig. 2(b). Only one spectrum was observed at 39.813 GHz, with a noise suppression of 80 dB, which indicates that supermode noise was well suppressed below −80 dB by the installation of a Fabry–Perot etalon.

Figure 3 shows the output waveform characteristics of the Nyquist pulse when α was set at zero. A rectangular spectral profile was obtained when the spectral filter profile generated by the LCoS was that given in Fig. 3(b). To obtain the rectangular profile, the transmittance on both edges of the optical filter was enhanced by approximately 5.3 dB. Thus, a sinc-like Nyquist pulse was obtained as shown in Fig. 3(c), where the FWHM of the Nyquist pulse was 3 ps. An output power of 15 mW with a 3 ps duration and a 40 GHz repetition rate gives a peak power of 125 mW, which is more than 10 times larger than that with a Nyquist pulse generated from a CW beam [8]. By increasing the OSNR by 10 dB, the multiplicity of the QAM data can be increased fourfold. In Ref. [8], for example, a polarization-multiplexed 160 Gsymbol/s, 64 QAM (1.92 Tbit/s) transmission was demonstrated with an SE of 7.5 bit/s/Hz. We therefore expect the multiplicity to be increased to 256 QAM and to achieve an SE of 10 bit/s/Hz by using a Nyquist laser instead of the CW laser-based pulse source. It should be noted that when a Nyquist pulse is generated from a CW beam, the output power is limited by the maximum allowable input power of the optical modulator for optical comb generation. This inevitably results in OSNR limitation, even if a high-power CW laser is used. Therefore, a much better OSNR can be obtained with the Nyquist laser. Figure 4 shows the output waveform characteristics of the Nyquist pulse when α was set at 0.2. When $\alpha = 0.2$, the height of the shoulders in the spectral profile were decreased slightly to 1.7 dB and the spectral width was increased to 2.9 nm by controlling the LCoS filter as shown in Fig. 4(b). The obtained Nyquist waveform given in Fig. 4(c) agrees well with the theoretical waveform shown in red. The pulse width

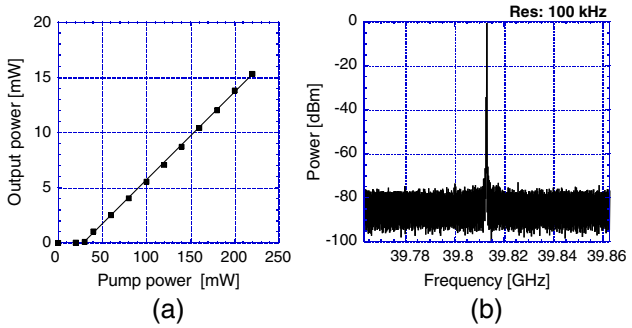

Fig. 2. Output characteristics of Nyquist laser. (a) The output power of the Nyquist laser as a function of the pump power and (b) the electrical spectrum of the output pulse train detected with a high-speed photodetector.

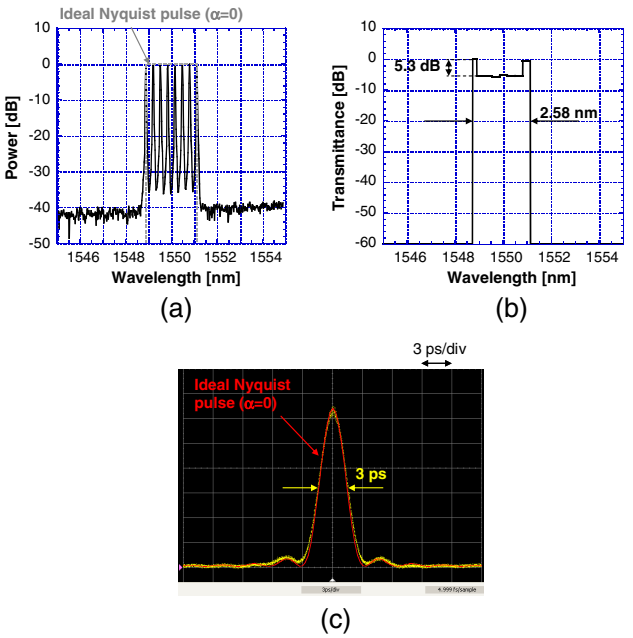

Fig. 3. Output waveform characteristics of Nyquist pulse when $\alpha = 0$. (a) The output spectral profile, (b) the spectral filter profile generated by the LCoS, and (c) the obtained sinc-like Nyquist pulse.

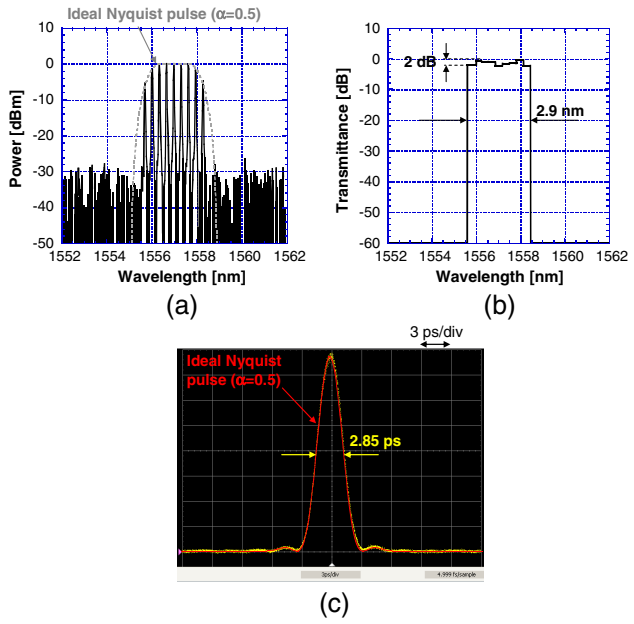

Fig. 5. Output waveform characteristics of the Nyquist pulse when α was 0.5. (a) The output spectral profile, (b) the spectral filter profile generated by the LCoS, and (c) the obtained Nyquist pulse. A small ringing on the wing still exists.

decreased slightly to 2.85 ps because of the larger filter width. When we set α at 0.5, the spectral profile of the output pulse on both shoulders was further decreased by 2 dB by setting the LCoS filter as shown in Fig. 5(b). In addition, a wider loss band on the shoulders was introduced to make the $\alpha = 0.5$ Nyquist pulse. Ringing is still clearly observed on the wing of the pulse, as shown in Fig. 5(c), where the experimental result agrees well with the red theoretical curve.

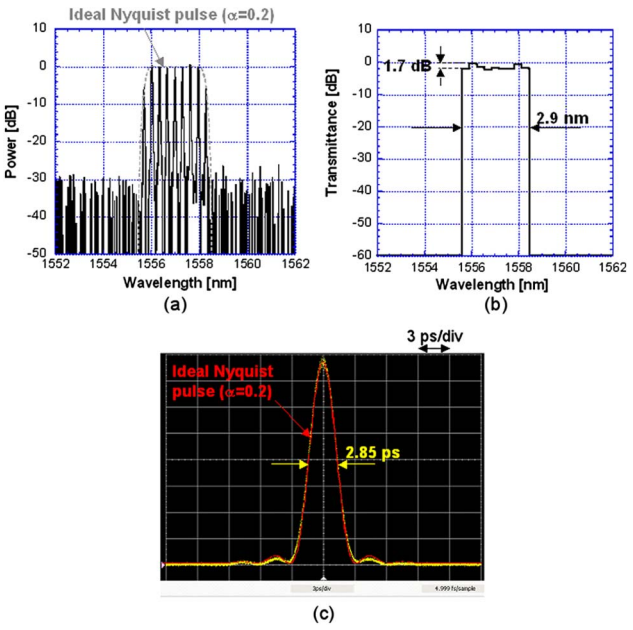

Fig. 4. Output waveform characteristics of the Nyquist pulse when α was 0.2. (a) The output spectral profile, (b) the spectral filter profile generated by the LCoS, and (c) the obtained Nyquist pulse.

Figure 6 shows the Nyquist output pulse when $\alpha = 0.8$, where we broadened the LCoS passband from 2.9 ($\alpha = 0.5$) to 3.55 nm to obtain a broader spectral profile, as shown in Fig. 6(a). The spectral profile starts to be similar to the ordinary spectral profile of a conventional Gaussian or sech pulse. The ringing on the wing has almost disappeared, as shown in Fig. 6(c), where the pulse width was decreased to 2.6 ps. When we set α at 1, we prepared a broader passband

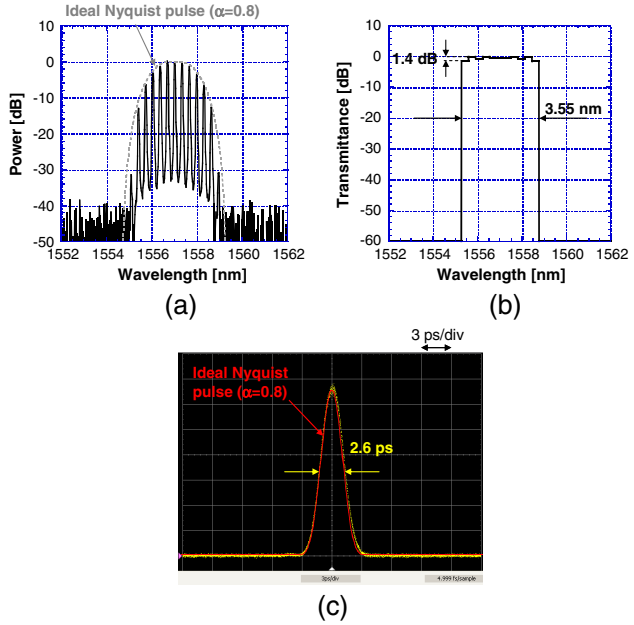

Fig. 6. Output waveform characteristics of the Nyquist pulse when α was 0.8. (a) The output spectral profile, (b) the spectral filter profile generated by the LCoS, and (c) the obtained Nyquist pulse. The ringing on the wing has almost disappeared.

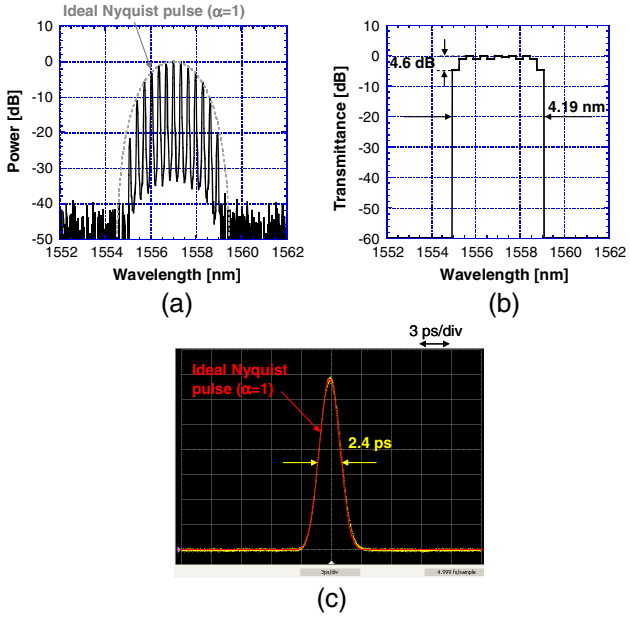

Fig. 7. Output waveform characteristics of the Nyquist pulse when α was 1. (a) The output spectral profile, (b) the spectral filter profile generated by the LCoS, and (c) the obtained Nyquist pulse. It looks like an ordinary pulse profile.

of 4.19 nm and a shoulder loss of 4.6 dB. Then we obtained the Nyquist spectral profile seen in Fig. 7(a). The pulse width was 2.4 ps, as shown in Fig. 7(c), and the pulses look similar to ordinary pulses. In part (a) of Figs. 3–7, dotted lines indicate theoretical spectral profiles for each α. In addition, to obtain a better fitted Nyquist spectral profile, we changed the transmittance slightly for every 40 GHz band in the LCoS, as seen in part (b) of Figs. 4–7, which was effective in compensating for the small spectral amplitude fluctuation in the mode locking.

The mode locking occurred more easily when α approached 1, since the Nyquist waveform became similar to ordinary pulses. An $\alpha = 0$ Nyquist pulse was the most difficult to obtain, because the top of the spectral profile had to be kept flat. All the experimental results described in Figs. 3–7 were obtained by AM mode locking with the use of a $LiNbO_3$ intensity modulator. We also generated the Nyquist pulses with FM mode locking using a $LiNbO_3$ phase modulator. We obtained the Nyquist pulses when α exceeded 0.8. However, at an α below 0.5, we were not able to obtain a stable Nyquist pulse, and a clock signal at 40 GHz for regenerative mode locking could not be extracted. This means that with FM mode locking, the phase of each longitudinal mode tends to be different because of the phase modulation given by the Bessel function, while the Nyquist pulse requires the same phase in each longitudinal mode. A flattop spectral profile under Nyquist mode locking can be realized with AM, because all longitudinal modes oscillate at the same phase due to the nature of AM.

4. NUMERICAL ANALYSIS OF THE NYQUIST LASER

A numerical model for the experimental setup of the Nyquist mode-locked laser is shown in Fig. 8, where intensity or phase

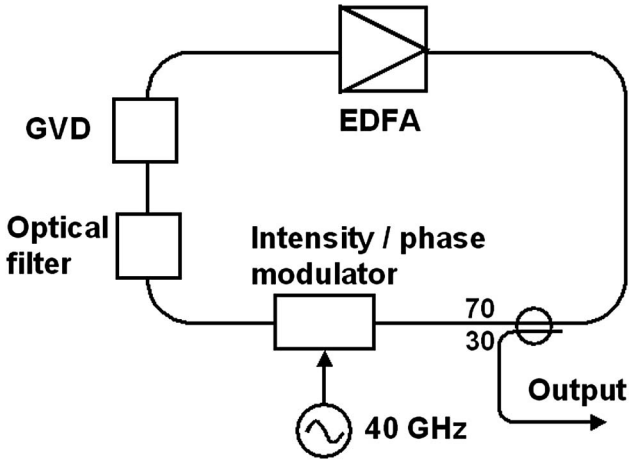

Fig. 8. Configuration of the Nyquist laser cavity used for numerical simulations.

modulation was applied with a sinusoidal function at 40 GHz. The split-step Fourier method was used for the pulse propagation in the fiber. However, since the laser cavity in the experiment was 17 m long with an average dispersion of 28.9 ps/km/nm, nonlinearity was not taken into account for the generation of a 3 ps pulse. This was realized by setting the nonlinear coefficient at zero in the nonlinear Schrödinger equation. We confirmed that the numerical result is identical even when including the nonlinear effects, which implies that the present laser operates in a linear regime and the nonlinearities do not play an important role because of the large dispersion. The gain in the EDFA, which compensates for the cavity loss, was calculated including gain saturation based on the rate equation between the pump power P_p and signal power P_s as follows:

$$\frac{dP_s}{dz} = \frac{(P_p/P_p^{\text{sat}} - 1)\sigma_s n P_s}{1 + 2P_s/P_s^{\text{sat}} + P_p/P_p^{\text{sat}}}, \tag{2}$$

$$\frac{dP_p}{dz} = -\frac{(P_s/P_s^{\text{sat}} + 1)\sigma_p n P_p}{1 + 2P_s/P_s^{\text{sat}} + P_p/P_p^{\text{sat}}}. \tag{3}$$

Here, σ_s and σ_p are the transition cross section at the signal and pump frequency ν_s and ν_p, respectively, n is the erbium ion population, and P_s^{sat} and P_p^{sat} are the saturation powers defined as

$$P_s^{\text{sat}} = \frac{A_{\text{eff},s} h\nu_s}{\sigma_s T}, \qquad P_p^{\text{sat}} = \frac{A_{\text{eff},p} h\nu_p}{\sigma_p T}, \tag{4}$$

where $A_{\text{eff},s}$ and $A_{\text{eff},p}$ are the effective areas of the signal and pump modes, respectively, and T is the lifetime of the upper state. The gain can then be obtained from the solution of Eqs. (2) and (3) as

$$G = \frac{P_s(L)}{P_s(0)}, \tag{5}$$

where L is the EDF length. We studied the transient evolution of the pulse in the cavity numerically, starting with the amplified spontaneous emission (ASE) noise as an initial condition. An optical filter that describes an LCoS filter and pulse broadening caused by fibers and optical elements were represented by the group velocity dispersion (GVD) element. A 30% output coupler was also assumed based on the experiment, and the output pulse was properly dispersion compensated depending on the α value.

A. AM Mode Locking

Simulation results obtained for $\alpha = 0$ are shown in Fig. 9, where parts (a)–(d) correspond to the spectral filter shape, the evolution of the Nyquist pulse from ASE noise to steady-state oscillation, the steady-state Nyquist waveform, and its optical spectrum, respectively. The filter shape given in Fig. 9(a) was set so that it was similar to the experimental setup shown in Fig. 3(b). The frequency bandwidth of 320 GHz in Fig. 9(a) corresponds to a spectral width of 2.58 nm in Fig. 3(b). In this condition, a stable steady-state waveform with a pulse width of 2.9 ps was obtained and the waveform was completely fitted with the theoretical Nyquist waveform shown by the dashed line. The simulation results agree well with the experimental results. Therefore, judging from the obtained waveform and the spectral profile, we can say that the output waveform is a Nyquist pulse with $\alpha = 0$.

Figure 10 shows the case for $\alpha = 0.5$, where the filter shape given in Fig. 10(a) was set so that it was similar to our experimental setup shown in Fig. 5(b). A frequency bandwidth of 370 GHz corresponds to a bandwidth of 3 nm in Fig. 5(b). A 2.8 ps Nyquist pulse with a small ripple was clearly obtained and agrees well with the experiment. The simulation results for $\alpha = 1$ are shown in Fig. 11, where the filter bandwidth was set at 525 GHz, which corresponds to a spectral width of 4.2 nm.

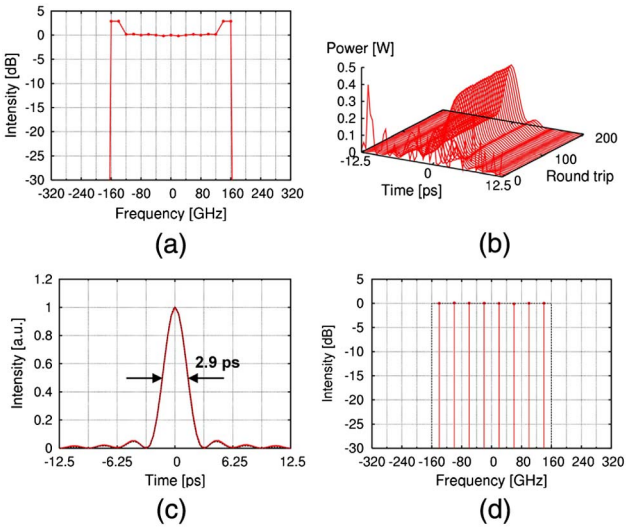

Fig. 9. Numerical results for the AM mode-locked Nyquist laser ($\alpha = 0$). (a) Filter profile, (b) transient evolution from ASE noise, (c) pulse waveform in the steady state (red) and the ideal Nyquist pulse waveform (black), (d) optical spectrum in the steady state (red) and the ideal Nyquist pulse spectrum (black).

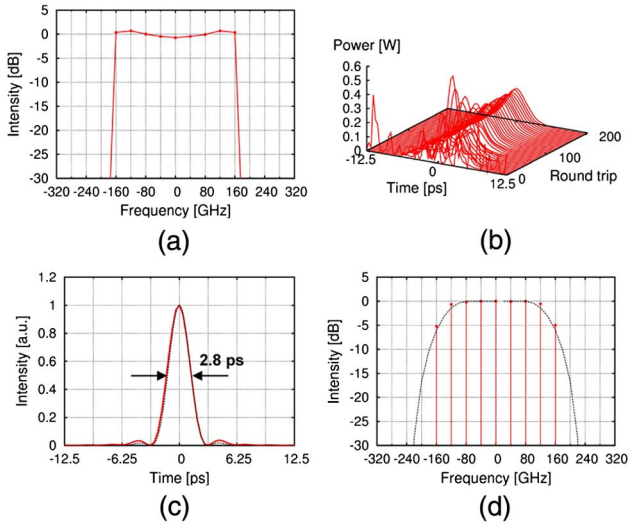

Fig. 10. Numerical results for the AM mode-locked Nyquist laser ($\alpha = 0.5$). (a) Filter profile, (b) transient evolution from ASE noise, (c) pulse waveform in the steady state (red) and the ideal Nyquist pulse waveform (black), (d) optical spectrum in the steady state (red) and the ideal Nyquist pulse spectrum (black).

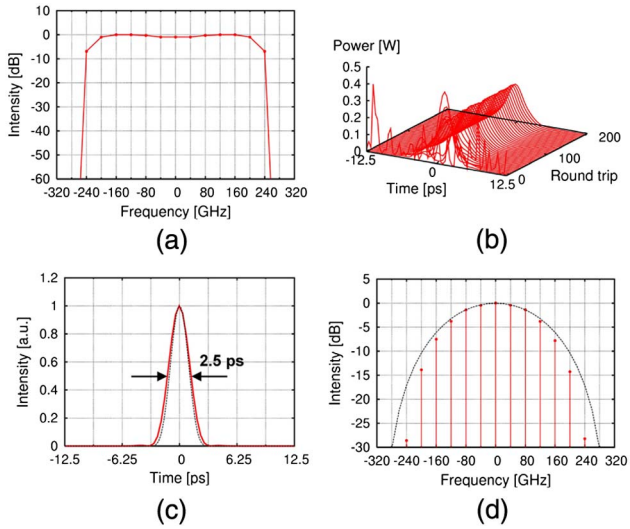

Fig. 11. Numerical results for the AM mode-locked Nyquist laser ($\alpha = 1$). (a) Filter profile, (b) transient evolution from ASE noise, (c) pulse waveform in the steady state (red) and the ideal Nyquist pulse waveform (black), (d) optical spectrum in the steady state (red) and the ideal Nyquist pulse spectrum (black).

The pulse width was 2.5 ps. The simulation results also agree well with the experimental results shown in Fig. 7.

In the simulation, we confirmed that stable Nyquist pulses were also obtained when the cavity dispersion had an opposite GVD value of −28.9 ps/km/nm. This indicates that the Nyquist pulse can be generated in the linear pulse propagation regime.

B. FM Mode Locking

As we experienced in the FM mode-locked Nyquist laser experiments, there was a large difference as regards the AM

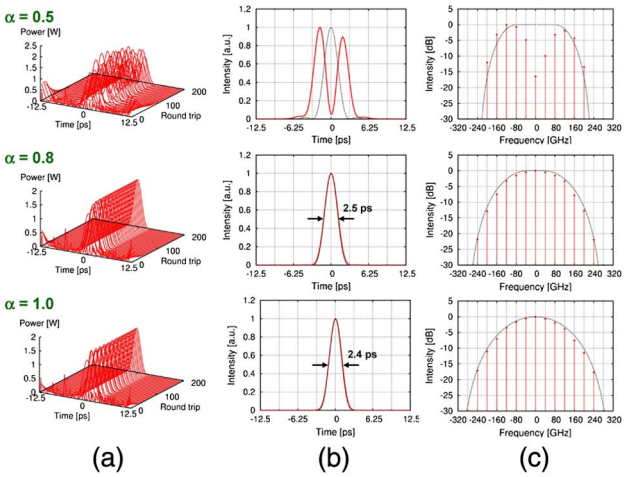

Fig. 12. Numerical results for the FM mode-locked Nyquist laser ($\alpha = 0.5$, 0.8, 1) with anomalous dispersion (28.9 ps/km/nm) in the cavity. (a) Transient evolution from ASE noise, (b) pulse waveform in the steady state (red) and the ideal Nyquist pulse waveform (black), and (c) optical spectrum in the steady state (red) and the ideal Nyquist pulse spectrum (black).

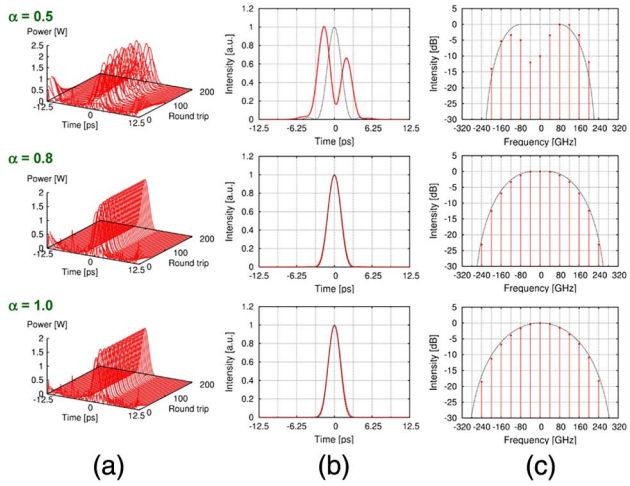

Fig. 14. Numerical results for the FM mode-locked Nyquist laser ($\alpha = 0.5$, 0.8, 1) with normal dispersion (−28.9 ps/km/nm) in the cavity. (a) Transient evolution from ASE noise, (b) pulse waveform in the steady state (red) and the ideal Nyquist pulse waveform (black), and (c) optical spectrum in the steady state (red) and the ideal Nyquist pulse spectrum (black).

mode locking. Here, we numerically investigate how the FM mode locking occurs at different α values under different dispersion conditions. Figures 12–14 correspond to conditions of anomalous GVD, zero GVD, and normal GVD, respectively, where we chose α values of 0.5, 0.8, and 1.0, respectively. In each figure, parts (a), (b), and (c) correspond to a waveform change toward a steady-state pulse, its steady-state waveform, and the corresponding spectral profile, respectively. For the anomalous dispersion shown in Fig. 12, the output pulse for $\alpha = 0.5$ was unstable and the spectral profile differed from the Nyquist shape, as we experienced in the experiment. For the smaller α values, the oscillation was also unstable. When we increased α to 0.8 and 1.0, we obtained stable pulse oscillations, and they could be fitted with the Nyquist profiles.

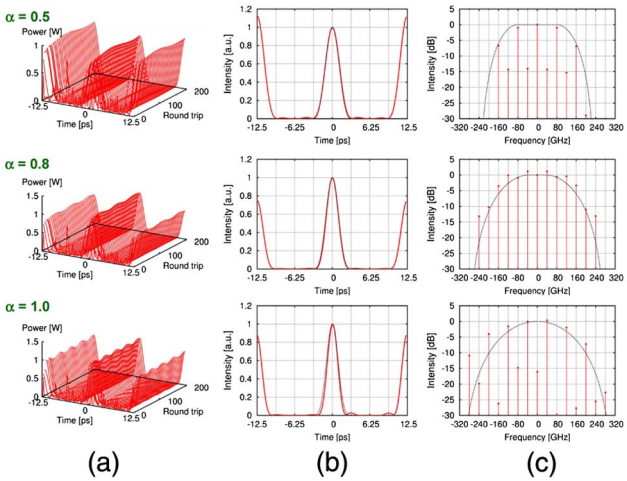

Fig. 13. Numerical results for the FM mode-locked Nyquist laser ($\alpha = 0.5$, 0.8, 1) with zero dispersion in the cavity. (a) Transient evolution from ASE noise, (b) pulse waveform in the steady state (red) and the ideal Nyquist pulse waveform (black), and (c) optical spectrum in the steady state (red) and the ideal Nyquist pulse spectrum (black).

Up-chirping in the phase modulation gave a stable oscillation to counterbalance the anomalous dispersion. These results indicate that it appears to be difficult to generate a sinc function Nyquist pulse with a flattop spectrum with FM mode locking, which is attributed to the fact that the phase in each longitudinal mode is different with phase modulation.

FM mode locking under zero GVD is shown in Fig. 13, where every case was unstable. This result is understandable, as the laser cavity has two possible oscillation conditions that occur every half-cycle due to up-chirping and down-chirping in the process of phase modulation. This causes unstable oscillation.

FM mode locking under a normal dispersion of −28.9 ps/km/nm is shown in Fig. 14. As with anomalous dispersion, stable Nyquist pulses were generated for α values of 0.8 and 1.0, but a stable pulse was not obtained when α was 0.5. It is important to note that the down-chirping of the phase modulation gave a stable pulse oscillation to counterbalance the normal dispersion.

5. SUMMARY

We proposed and demonstrated a Nyquist laser that can directly emit an optical Nyquist pulse train. The laser was based on a 1.55 μm regeneratively and harmonically mode-locked erbium fiber laser, where a special optical filter called an LCoS was installed to generate a Nyquist pulse as the output pulse. The peak power reached 125 mW at a repetition rate of 40 GHz and a pulse width of 3 ps. Various types of Nyquist pulses were generated by changing the spectral curvature of the filter with a roll-off factor α of between 0 and 1. A Fabry–Perot etalon was also installed in the laser cavity to select longitudinal modes with an FSR of 40 GHz, resulting in the suppression of mode hopping in the regenerative mode locking. Numerical analyses showed that there were stable Nyquist pulses in the laser cavity, and AM mode locking can generate better

Nyquist pulses with smaller α values than FM mode locking. The Nyquist laser makes it possible to realize coherent Nyquist OTDM transmission with a higher OSNR than conventional Nyquist pulse generation schemes, and thus is expected to constitute an attractive light source for ultrahigh-speed transmission with high-QAM multiplicity, which will lead to an ultrahigh SE of over 10 bit/s/Hz even at a single-channel bit rate beyond 1 Tbit/s.

REFERENCES

1. M. Nakazawa, K. Kikuchi, and T. Miyazaki, eds., *High Spectral Density Optical Transmission Technologies* (Springer, 2010).
2. D. Qian, M.-F. Huang, E. Ip, Y. Huang, Y. Shao, J. Hu, and T. Wang, "101.7 Tb/s (370 × 294 Gb/s) PDM-128QAM-OFDM transmission over 3 × 55 km SSMF using pilot-based phase noise mitigation," in *Optical Fiber Communication Conference/National Fiber Optic Engineers Conference* (Optical Society of America, 2011), paper PDPB5.
3. Y. Koizumi, K. Toyoda, M. Yoshida, and M. Nakazawa, "1024 QAM (60 Gbit/s) single-carrier coherent optical transmission over 150 km," Opt. Express **20**, 12508–12514 (2012).
4. S. Beppu, K. Kasai, M. Yoshida, and M. Nakazawa, "2048 QAM (66 Gbit/s) single-carrier coherent optical transmission over 150 km with a potential SE of 15.3 bit/s/Hz," in *Optical Fiber Communication Conference* (Optical Society of America, 2014), paper W1A.6.
5. M. Nakazawa, T. Hirooka, P. Ruan, and P. Guan, "Ultrahigh-speed 'orthogonal' TDM transmission with an optical Nyquist pulse train," Opt. Express **20**, 1129–1140 (2012).
6. T. Hirooka, P. Ruan, P. Guan, and M. Nakazawa, "Highly dispersion-tolerant 160 Gbaud optical Nyquist pulse TDM transmission over 525 km," Opt. Express **20**, 15001–15008 (2012).
7. T. Hirooka and M. Nakazawa, "Linear and nonlinear propagation of optical Nyquist pulses in fibers," Opt. Express **20**, 19836–19849 (2012).
8. D. O. Otuya, K. Kasai, T. Hirooka, M. Yoshida, and M. Nakazawa, "1.92 Tbit/s, 64 QAM coherent Nyquist pulse transmission over 150 km with a spectral efficiency of 7.5 bit/s/Hz," in *Optical Fiber Communication Conference* (Optical Society of America, 2014), paper W1A.4.
9. M. Nakazawa, E. Yoshida, and Y. Kimura, "Ultrastable harmonically and regeneratively modelocked polarization-maintaining erbium-doped fiber ring laser," Electron. Lett. **30**, 1603–1605 (1994).
10. H. A. Haus, "Mode-locking of lasers," IEEE J. Sel. Top. Quantum Electron. **6**, 1173–1185 (2000).
11. L. F. Mollenauer and R. H. Stolen, "The soliton laser," Opt. Lett. **9**, 13–15 (1984).
12. F. Ouellette and M. Piche, "Pulse shaping and passive mode-locking with a nonlinear Michelson interferometer," Opt. Commun. **60**, 99–103 (1986).
13. E. P. Ippen, H. A. Haus, and L. Y. Liu, "Additive pulse modelocking," J. Opt. Soc. Am. B **6**, 1736–1745 (1989).
14. D. E. Spence, P. N. Kean, and W. Sibbett, "60-fsec pulse generation from a self-mode-locked Ti: sapphire laser," Opt. Lett. **16**, 42–44 (1991).
15. D. J. Kuizenga and A. E. Siegman, "FM and AM mode locking of the homogeneous laser—part I: theory," IEEE J. Quantum Electron. **QE-6**, 694–708 (1970).
16. D. J. Kuizenga and A. E. Siegman, "FM and AM mode locking of the homogeneous laser—part II: experimental results in a Nd:YAG laser with internal FM modulation," IEEE J. Quantum Electron. **QE-6**, 709–715 (1970).
17. H. A. Haus, "A theory of forced mode locking," IEEE J. Quantum Electron. **QE-11**, 323–330 (1975).
18. H. Nyquist, "Certain topics in telegraph transmission theory," Trans. Am. Inst. Electr. Eng. **47**, 617–644 (1928).
19. G. Baxter, S. Frisken, D. Abakoumov, H. Zhou, I. Clarke, A. Bartos, and S. Poole, "Highly programmable wavelength selective switch based on liquid crystal on silicon switching elements," in *Optical Fiber Communication Conference* (Optical Society of America, 2006), paper OTuF2.
20. J. Schröder, S. Coen, T. Sylvestre, and B. J. Eggleton, "Dark and bright pulse passive mode-locked laser with in-cavity pulse-shaper," Opt. Express **18**, 22715–22721 (2010).
21. N. K. Metzger, W. Lubeigt, D. Burns, M. Griffith, L. Laycock, A. A. Lagatsky, C. T. A. Brown, and W. Sibbett, "Ultrashort-pulse laser with an intracavity phase shaping element," Opt. Express **18**, 8123–8134 (2010).
22. M. Yoshida, K. Kasai, and M. Nakazawa, "Mode-hop-free, optical frequency tunable 40 GHz mode-locked fiber laser," IEEE J. Quantum Electron. **43**, 704–708 (2007).
23. M. Nakazawa, E. Yoshida, and K. Tamura, "Ideal phase-locked loop (PLL) operation of a 10 GHz erbium-doped fiber laser using regenerative modelocking as an optical voltage controlled oscillator," Electron. Lett. **33**, 1318–1320 (1997).

Research Article Vol. 1, No. 1 / July 2014 / Optica 23

Time–bandwidth engineering

Bahram Jalali,[1,2,3,*] Jacky Chan,[1] and Mohammad H. Asghari[1]

[1]Department of Electrical Engineering, University of California, Los Angeles, 420 Westwood Plaza, Los Angeles, California 90095, USA

[2]Department of Bioengineering, University of California, Los Angeles, 420 Westwood Plaza, Los Angeles, California 90095, USA

[3]Department of Surgery, David Geffen School of Medicine, University of California, Los Angeles, 420 Westwood Plaza, Los Angeles, California 90095, USA

*Corresponding author: Jalali@ucla.edu

Received 2 April 2014; revised 20 May 2014; accepted 25 May 2014 (Doc. ID 209405); published 22 July 2014

We describe compression and expansion of the time–bandwidth product of signals and present tools to design optical data compression and expansion systems that solve bottlenecks in the real-time capture and generation of wideband data. Applications of this analog photonic transformation include more efficient ways to sample, digitize, and store optical data. Time–bandwidth engineering is enabled by the recently introduced Stretched Modulation (S_M) Distribution function, a mathematical tool that describes the bandwidth and temporal duration of signals after arbitrary phase and amplitude transformations. We demonstrate design of time–bandwidth engineering systems in both near-field and far-field regimes that employ engineered group delay (GD), and we derive closed-form mathematical equations governing the operation of such systems. These equations identify an important criterion for the maximum curvature of warped GD that must be met to achieve time–bandwidth compression. We also show application of the S_M Distribution to benchmark different GD profiles and to the analysis of tolerance to system nonidealities, such as GD ripples. © 2014 Optical Society of America

OCIS codes: (070.1170) Analog optical signal processing; (120.0120) Instrumentation, measurement, and metrology.

http://dx.doi.org/10.1364/OPTICA.1.000023

1. INTRODUCTION

With the quantity of data growing exponentially, new approaches to data capture and compression are urgently needed. With respect to the field of optics, this predicament arises in fiber optic communication and in real-time optical instruments [1]. Such instruments are used in study of optical rogue waves [2–5], in ultrafast signal measurement [6–12], and ultrafast imaging [13–15]. Owing to their high measurement rate, real-time instruments produce a fire hose volume of data that overwhelms even the most advanced computers [16]. This necessitates innovations in data management and inline processing techniques. As a case study, consider a dispersive Fourier transform (DFT)-based real-time spectrometer or camera, such as the time stretch microscopy [13] that captures single-shot optical spectra or images at a 100 MHz frame rate with each frame containing 1000 samples. Assuming each sample is digitized with 10 bits of accuracy, such a system produces 1 terabit of data each second [16]. This is equivalent to capturing and storing >10 h of full-HD movies each second! Time–bandwidth compression can alleviate this problem.

The generation of waveforms with wide instantaneous bandwidth can be a bottleneck in radar, communication systems, and laboratory instruments. To this end, photonic arbitrary waveform generation that employs spectrum to time mapping has been proposed as a potential solution [17–19]. These systems are limited by the time bandwidth of the component used for spectrum encoding. Time–bandwidth expansion may improve the performance in these applications.

The Stretched Modulation (S_M) Distribution is a recently introduced mathematical tool that describes the information bandwidth and the record length [20,21] of signal intensity after arbitrary transformations. It provides graphical and intuitive description of time–bandwidth transformation and can be used to benchmark different optical systems. It was recently used for the design and demonstration of the first optical real-time data compression system [22].

In this work, we present foundations of methods to manipulate the time bandwidth of optical signals using photonic platforms. We employ the S_M Distribution to design time–bandwidth engineering (TBE) systems in both near-field and far-field regimes. Using the S_M distribution we derive, for the first time to the best of our knowledge, the equations governing the TBE and identify an important criterion on the maximum curvature of warped group delay (GD) that must be met in order to achieve time–bandwidth compression. This criterion is then used to compare various GD profiles as it relates to their utility for TBE. We also show, for the first time to the best of our knowledge, that S_M Distribution can be used to analyze the effect of system nonidealities in TBE systems. In particular, we study the effect of experimentally measured GD ripples of a chirped fiber Bragg grating fabricated for optical real-time data compression application on the bandwidth compression factor and time–bandwidth product (TBP). S_M Distribution analysis of four optical systems indicate that the TBP in far-field operation is determined by GD ripples at lower frequencies, whereas, in the case of near-field operation, it is determined by ripples at higher frequencies.

2. STRETCH MODULATION DISTRIBUTION

The system block diagrams for general TPE systems are shown in Fig. 1. Input electric field $E_i(t)$ has a time duration of T_{in} and bandwidth of BW_{in}. The transformation is described by phase kernel $\tilde{K}(\omega)$ and a nonlinear operation, a simple example of which is the field-to-intensity conversion $E_i(t) \cdot E_i(t)^*$. In the case of TBP compression [Fig. 1(a)], the transformation matches the signal bandwidth to that of the back-end digitizer (e.g., an oscilloscope or spectrometer), while at the same time minimizing the record length to avoid generation of redundant data. In the case of expansion, the transformation increases the modulation TBP of a generated signal. Since this transformation intentionally warps the signal, it can be referred to as the anamorphic transform, a metaphoric reference to the technique of anamorphism in graphic arts [16].

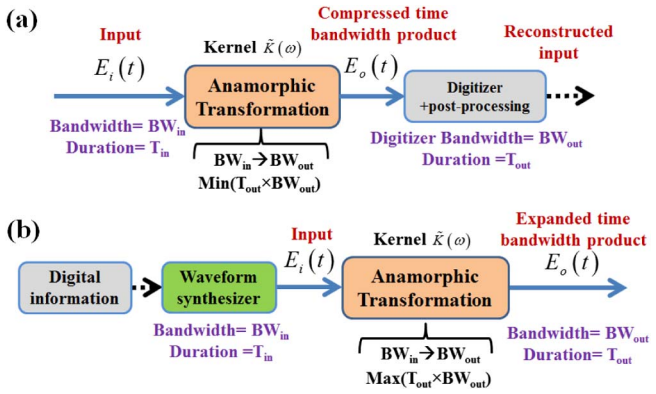

Fig. 1. System block diagrams for two applications of TBE of optical signals. (a) Real-time measurement. In such a system, optical signal bandwidth is compressed to match the backend digitizer speed, and, at the same time, the volume of data is reduced. After capturing and postprocessing, the input signal is digitally reconstructed by backpropagation. (b) Wideband waveform generation. In such a system, the transformation increases the TBP of a synthesized optical waveform.

The S_M Distribution is a complex-valued three-dimensional plot that allows one to design TBE systems. It describes the information bandwidth and duration of the signal intensity after a transformation that is mathematically described by the kernel of S_M. The Distribution can be written as [20,21]

$$S_M(\omega, t) = \int_{-\infty}^{\infty} \tilde{E}_i(\omega_1)\tilde{E}_i^*(\omega_1 + \omega)\tilde{K}(\omega_1)\tilde{K}^*(\omega_1 + \omega)e^{j\cdot\omega_1\cdot t}d\omega_1, \quad (1)$$

where t and ω are time and frequency variables, $\tilde{E}_i(\omega)$ is the input complex-field spectrum, and $\tilde{K}(\omega)$ is the operation kernel describing the photonic operation performed on the signal. The S_M Distribution provides a tool to design TBE systems through proper choice of the operation kernel. The top and bottom plots in Fig. 2 are schematics showing the S_M Distribution of input (top plot) and output (bottom plot) in an optical system where the kernel describes a filter with sublinear phase derivative (group delay). Such a system compresses the TBP of the information envelope [20–22].

Considering the Distribution as a cross correlation of the signal spectrum after transformation with its time-shifted waveform, the maximum absolute amount of time variable t at which the $S_M(\omega, t)$ function has non-zero values is the duration of output signal T_{out}. This is given by the half-height of the plot in S_M Distribution or half-extent in the temporal direction; see Fig. 2.

From Eq. (1), it can be shown that at $t = 0$ the cross section of the Distribution is the output modulation (intensity) spectrum:

$$S_M(\omega, 0) = FT\{|E_o(t)|^2\}, \quad (2)$$

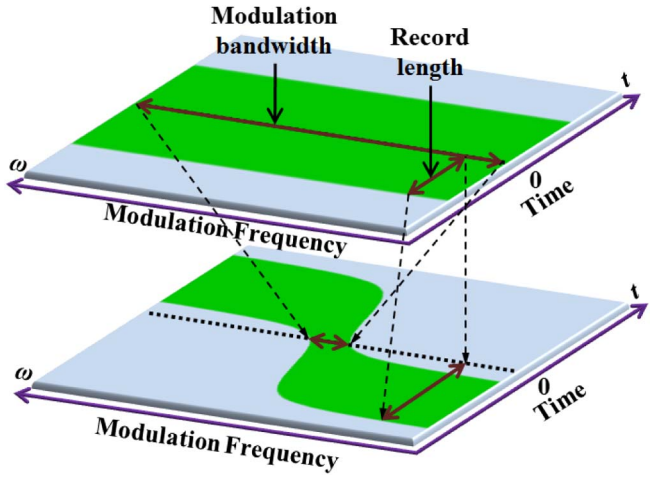

Fig. 2. S_M Distribution is a mathematical tool to design and benchmark optical TBE systems. At time = 0 (horizontal axis), the magnitude of the S_M function represents the intensity modulation bandwidth, and its half-extent along the time axis is the record length. The top and bottom plots are qualitative and show the magnitude of S_M Distribution of input and output signals in a system with a sublinear GD profile. The S_M Distribution shows how the TBP of the signal intensity can be engineered.

where FT is the Fourier transform. Thus, the width of the cross section at $t = 0$ gives the output modulation bandwidth; see Fig. 2.

The phase kernel $\tilde{K}(\omega)$, which is the transfer function of an optical system, allows one to engineer the TBP of the modulation envelope. Let the operation kernel be defined by a nonlinear phase operator:

$$\tilde{K}(\omega) = e^{j\cdot\beta(\omega)}. \tag{3}$$

The kernel's phase profile $\beta(\omega)$ is characterized by the phase derivative, i.e., the GD profile $\tau(\omega) = d\beta(\omega)/d\omega$. The information of the TBP can be manipulated by operating on the signal's complex field with a specific kernel followed by a nonlinear operation provided by the photo-detector.

3. DESIGN AND ANALYSIS OF TBE SYSTEMS

To show how the Distribution can be used to design and analyze TBE systems, we consider systems in which the operation kernel represents a phase filter with different GD profiles. In practice, the filter operation can be implemented with a dispersive optical element with a designed GD profile. After dispersion, the signal can be in the far-field or near-field regime, depending on whether the stationary phase approximation is satisfied or not. The far field is achieved for a large amount of GD dispersion and/or when the signal has a very large bandwidth, leading to one-to-one mapping of frequency into time. Conversely, the near field refers to the regime prior to the stationary phase approximation being satisfied. We note that in the far field there is warped (nonlinear or nonuniform) frequency-to-time mapping (warped dispersive Fourier transform), whereas in the near field there is no one-to-one mapping. Therefore, the near-field case, on its own, is not a Fourier transform or frequency–time mapping for arbitrary signals.

We consider three types of GD profiles, namely, linear, sub-linear, and super-linear. Here the sub-linear and super-linear profiles are defined as functions that grow slower or faster than a linear function when its argument becomes very large. Figure 3 shows qualitative profiles of these three types of GD. Here we compare the S_M Distribution plots associated with these three GDs. The input signal used for numerical simulations in this paper is shown in the time and spectral domains in Fig. 4. For this set of simulations, we have normalized the input signal to its maximum bandwidth. The input was designed to have a collection of different temporal features, such as coarse and fine temporal features, with different durations. It also includes both closely spaced as well as sparsely spaced features.

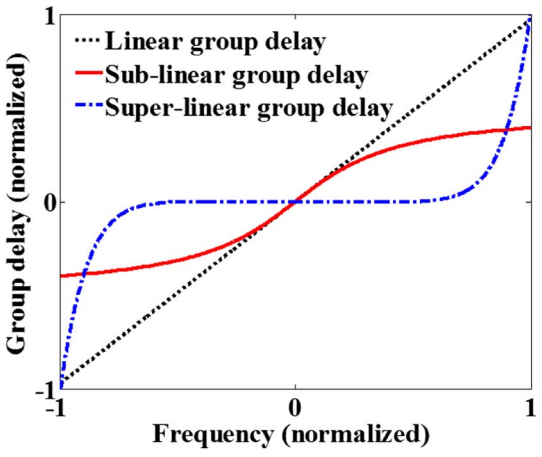

Fig. 3. Three different qualitative GD profiles that can be used to engineer the TBP of optical signals. S_M Distribution plots corresponding to these profiles are shown in Fig. 5.

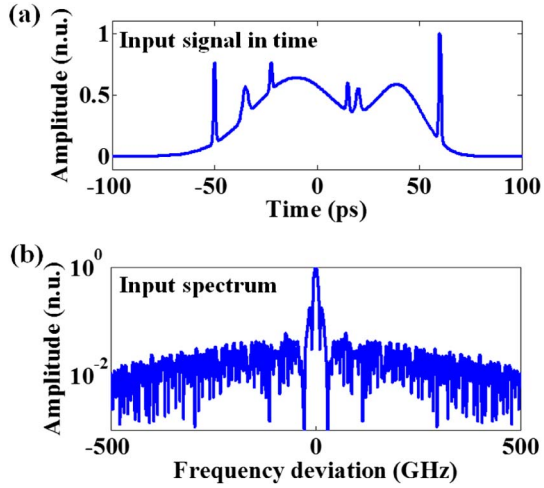

Fig. 4. Arbitrary input signal in (a) time and (b) spectral domains used in this paper.

Figure 5 shows the S_M Distribution of these three systems when operated in the near-field and far-field regimes. As shown in Fig. 5(a), when the GD has a linear profile, the Distribution is linearly tilted, resulting in a reduced modulation bandwidth. However, record length is proportionally increased. In this case, the TBP is either conserved (in the far-field regime) or expanded (in the near-field regime). However, if we cause a nonlinear tilt (i.e., a warp) having the shape shown in Fig. 5(b), corresponding to the sub-linear GD profile shown in Fig. 3, the bandwidth is reduced but the record length is not increased proportionally. In this case, one achieves TBP compression in both the near-field and far-field regimes. Finally, if the Distribution is warped in the manner shown in Fig. 5(c), corresponding to the super-linear GD profile shown in Fig. 3, the TBP is expanded in both the near-field and far-field regimes.

4. MATHEMATICAL FOUNDATIONS OF THE S_M DISTRIBUTION

Here we calculate the TBP of a bandwidth-limited signal $E(t)$ after propagation through a filter or a dispersive optical element with GD response $\tau(\omega) = d\beta(\omega)/d\omega$, where $\beta(\omega)$ is the phase profile of the system kernel. By substituting Eq. (3) into Eq. (1) and changing variables ($\omega_1 \rightarrow \omega_1 - \omega/2$), the absolute value of the S_M Distribution at the output can be represented as follows:

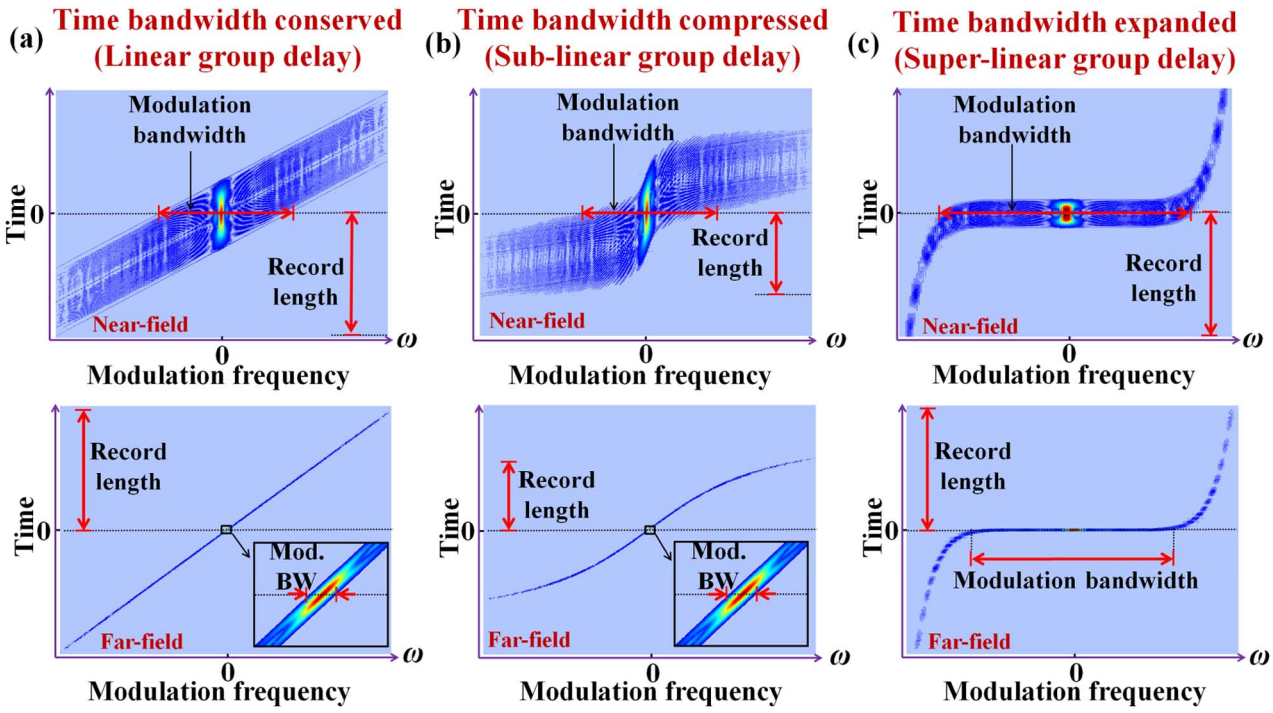

Fig. 5. S_M Distribution is used to design TBE systems with engineered TBP. The magnitude of S_M is shown here. At Time = 0 (horizontal axis), it represents the modulation bandwidth. The half-extent along the vertical direction is the record length. Here we have compared the Distribution for three cases: time–bandwidth (a) conserved, (b) compressed, and (c) expanded. In each case, we have shown operation in the near field and the far field. The input signal is shown in Fig. 4. The qualitative GD profile corresponding to each case is shown in Fig. 3.

$$|S_{M,out}(\omega,t)| = \left|\int_{-\infty}^{\infty}\tilde{E}_i\left(\omega_1-\frac{\omega}{2}\right)\tilde{E}_i^*\left(\omega_1+\frac{\omega}{2}\right)\cdot e^{j(\beta(\omega_1-\frac{\omega}{2})-\beta(\omega_1+\frac{\omega}{2}))}e^{j\cdot\omega_1\cdot t}\,d\omega_1\right|. \quad (4)$$

The phase term $[\beta(\omega_1 - \omega/2) - \beta(\omega_1 + \omega/2)]$ can be simplified by using their Taylor series expansion:

$$\begin{aligned}&\beta(\omega_1-\omega/2)-\beta(\omega_1+\omega/2)\\&=-2\cdot\omega_1\cdot\beta'(\omega/2)-\frac{\omega_1^3}{3}\cdot\beta'''(\omega/2)+\ldots\\&=-\sum_{n=0}^{\infty}\frac{2\cdot\omega_1^{2n+1}}{(2n+1)!}\frac{\partial^{2n}\tau(\omega_1)}{\partial\omega_1^{2n}}\bigg|_{\omega_1=\omega/2}.\end{aligned} \quad (5)$$

In deriving Eq. (5), we have used the assumption that the profile of the phase kernel, $\beta(\omega)$, is an even function. For the case that the GD curvature, $\tau''(\omega)$, is sufficiently small, i.e., $|\tau''(\omega/2)| \ll 24\cdot|\tau(\omega/2)|/\Delta\omega^2$, where $\Delta\omega$ is the input signal complex-field bandwidth, we have

$$\beta(\omega_1-\omega/2)-\beta(\omega_1+\omega/2)\approx-2\cdot\omega_1\cdot\tau(\omega/2). \quad (6)$$

In this case, Eq. (4) is simplified to

$$|S_{M,out}(\omega,t)| = |S_{M,in}(\omega,t+2\cdot\tau(\omega/2))|, \quad (7)$$

where $S_{M,in}(\omega, t)$ is the Distribution of the input signal without any filter. When $E_o(t) = E_i(t)$, it is easy to see that the function $S_{M,in}(\omega, t)$ is nonzero from $-T_{in}$ to T_{in}, where T_{in} is the input signal duration. Thus, by inserting $t = T_{in}$ into Eq. (7), one can calculate that, for systems with monotonic GD and for input signals with monotonic chirp or that are transform limited, the maximum range of time (i.e., vertical) features in $S_{M,out}$ Distribution is $T_{in} + 2.\tau(\Delta\omega/2)$. The condition on the curvature of GD described above must be met to achieve time–bandwidth compression. If not, the compression is compromised.

We showed earlier using Eq. (1) that the duration of the output signal is given by half-extent of the S_M Distribution. Thus, the following equation gives the output signal duration:

$$T_{out} = T_{in} + 2\tau(\Delta\omega/2). \quad (8)$$

We have graphically shown how the output signal duration is related to the input signal and the system kernel. This relation is shown in Fig. 6. Mathematically described by Eq. (8), it is valid for both the near-field and far-field regimes. In the far field, Eq. (8) can be approximated by $T_{out} \approx 2\cdot\tau(\Delta\omega/2)$.

As seen in Fig. 3 the modulation bandwidth, BW_{out} or $\Delta\omega_m$, is the $t = 0$ intercept of the S_M plot. Mathematically, it is equivalent to finding the minimum frequency at which the input duration plus the GD shift is larger than zero:

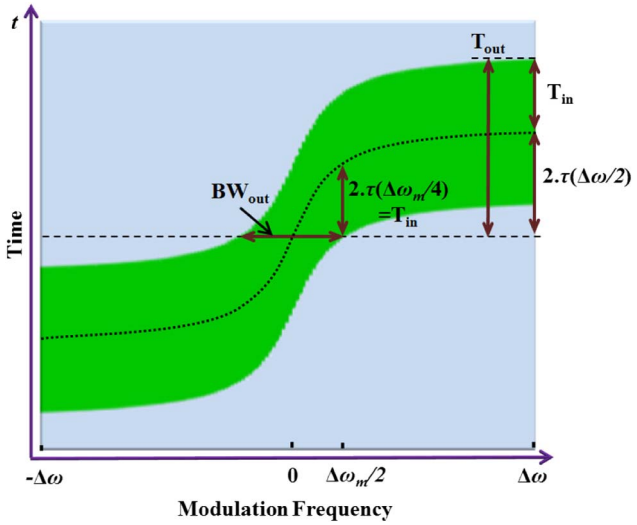

Fig. 6. The magnitude of the S_M Distribution describes the output signal duration and modulation bandwidth after passing through a TBE system.

$$-\mathrm{T_{in}} + 2\tau(\Delta\omega_m/4) = 0$$
$$\Rightarrow \Delta\omega_m = 4\cdot\tau^{-1}(\mathrm{T_{in}}/2). \quad (9)$$

This is the estimated output intensity bandwidth assuming that the input signal has infinite bandwidth. Because in a physical system the maximum output intensity bandwidth is limited by twice the input bandwidth, the $\Delta\omega_m$ is the minimum amount of input signal bandwidth and the amount estimated for $\Delta\omega_m$ with infinite input bandwidth given by Eq. (9):

$$\Delta\omega_m = \min\left\{4\cdot\tau^{-1}\left(\frac{\mathrm{T_{in}}}{2}\right), 2\cdot\Delta\omega\right\}. \quad (10)$$

The output TBP can then be calculated as follows:

$$\mathrm{TBP_{out}} = (\mathrm{T_{in}} + 2\cdot\tau(\Delta\omega/2)) \cdot \min\left\{4\cdot\tau^{-1}\left(\frac{\mathrm{T_{in}}}{2}\right), 2\cdot\Delta\omega\right\}. \quad (11)$$

The above conclusion assumes that the signal is broadband, comprising both fast and slow features, i.e., high and low instantaneous frequencies with respect to the bandwidth of the GD. Such a signal has redundancy in the time domain (see Fig. 4). If the signal has only high frequencies, then the effect of GD will be different than that described above. Also, as with any other data compression method, the maximum compression that can be achieved is signal dependent. In particular, it will depend on the amount of redundancy in the signal, a quantity that will be reflected in the probability distribution function of the signal instantaneous frequency.

To examine the output TBP, we have compared the calculated value from Eq. (11) to numerical simulations. The input optical signal is shown in the time and spectral domains in Fig. 4. The input signal has duration of 200 ps and complex-field bandwidth of 1 THz. Duration and the bandwidth here are defined as the 1% value (from peak). We have considered three systems with different types of GD profiles, i.e., with linear, sub-linear, and super-linear GD profiles shown in Fig. 7(a). The super-linear case has the same total GD as the linear case and the sub-linear case has the same slope as the linear case at the origin. The GD profiles of these functions are given by

$$\begin{aligned} \textit{Linear GD}{:}\tau(\omega) &= k\cdot A\cdot B\cdot\omega, \\ \textit{Super-linear GD}{:}\tau(\omega) &= k\cdot A\cdot\tan(B/2\cdot\omega), \\ \textit{Sub-linear GD}{:}\tau(\omega) &= k\cdot A\cdot\tan^{-1}(B\cdot\omega), \end{aligned} \quad (12)$$

where tan is the tangent function, $\tan^{-1}$ is the inverse tangent function, $A = 2.81$ ns, $B = 0.22$ ns, and k is the dispersion strength factor. We have plotted the numerically calculated output TBP using Eq. (11) in each case as a function of

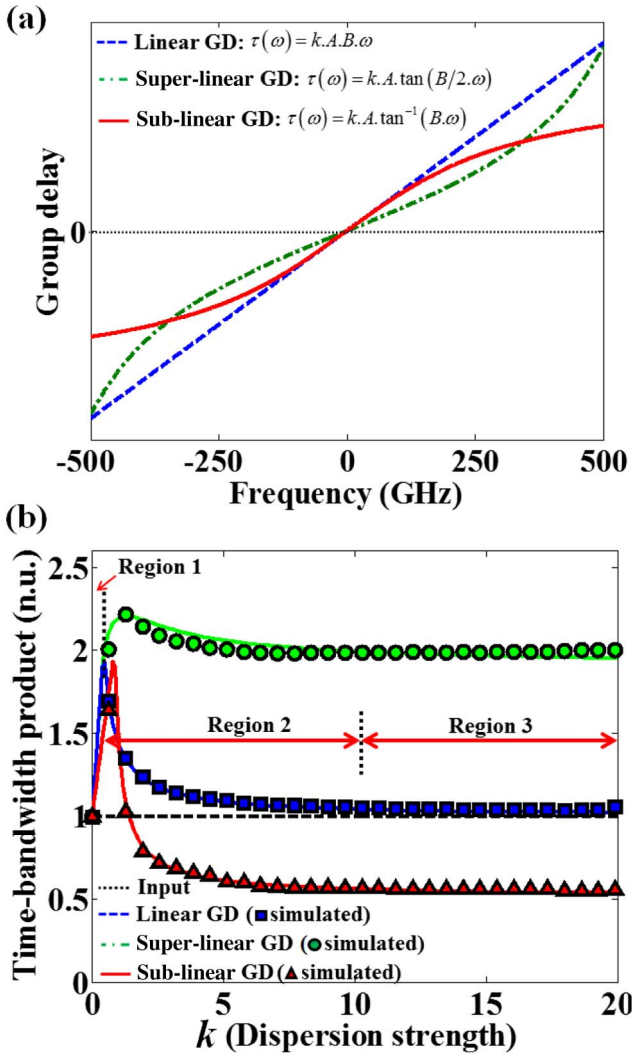

Fig. 7. (a) Three different GD profiles to engineer the TBP of optical signals. $A = 2.81$ ns, $B = 0.22$ ns, and k is the dispersion strength variable. (b) Simulated output TBP as a function of dispersion strength, k, compared to the calculated TBP using Eq. (11). Examples of S_M Distributions in three regions for the case of linear GD are shown in Fig. 8.

the k factor in Fig. 7(b). Calculated TBP of the linear, super-linear, and sub-linear cases are shown with red solid, green dashed–dotted, and blue dashed lines, respectively. The TBP in each case is normalized to the input signal TBP. Small k factors correspond to the near-field regime and large k factors correspond to the far-field regime. We have also simulated the output signal in each case and calculated the output signal TBP and compared them to predictions by Eq. (11) in Fig. 7(b). Simulated output signal TBP for the linear, super-linear, and sub-linear cases are shown with red triangles, green circles, and blue squares, respectively. As seen from the simulation results, there is an excellent agreement with the output TBP equations given by Eq. (11).

We can identify three regions of operation spanning the near- to far-field regimes. For the case of linear GD, an example of S_M Distribution in each region is shown in Fig. 8. Region 1 ($k < 0.5$) corresponds to the case when $\Delta\omega_m = 2 \cdot \Delta\omega$. Since in this region the output bandwidth is fixed but the output duration is increased [given by Eq. (8)], the TBP is enlarged as shown in Fig. 8(a). However, in Regions 2 and 3, the TBP gets close to unity as dispersion is increased [see Figs. 7(b), 8(b), and 8(c)].

5. PHYSICAL IMPLEMENTATION

The system block diagram for a simple optical TBE system is shown in Fig. 9(a). The desired phase kernel profile for TBE can be obtained using a chirped fiber Bragg grating (CFBG). A CFBG offers great flexibility in dispersion profile and has low insertion loss. An example of a designed CFBG period profile along grating distance to demonstrate a sub-linear GD profile is shown in Fig. 9(b). This reflection CFBG is 100 cm long, its nominal period is 504.54 nm, and the effective refractive index of the fiber is 1.54. The measured GD profile of a fabricated CFBG using this CFBG design is shown in Fig. 9(c). CFBGs exhibit GD ripples, which are problematic. There are demonstrated techniques for mitigating the effect of ripples that can be employed in our technique to calibrate the GD ripples in post-processing analysis [12,23]. We note that the transformed signal has both phase and amplitude requiring complex field recovery before reconstruction in the digital domain [20–22].

Finally, we note that, if the carrier wavelength is moved away from the center of symmetry of the GD curve, a different characteristic for the TBE system is achieved. In particular,

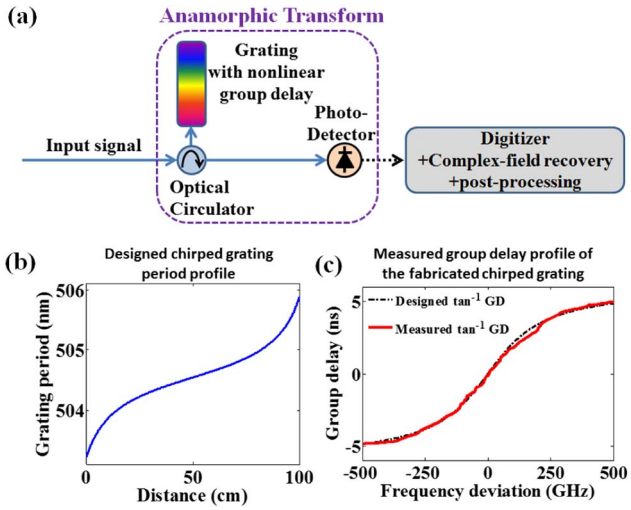

Fig. 9. (a) System block diagram for a simple experimentally demonstrated analog optical TBE (compression and expansion) system [22]. In this implementation, the desired phase kernel profile for TBE is obtained using a CFBG. The transformed signal has both phase and amplitude requiring complex field recovery before reconstruction in the digital domain. (b) Example of designed grating period profile to realize time–bandwidth compression using a sub-linear GD profile. (c) Experimentally measured GD profile of the fabricated chirp grating compared to the target sub-linear GD profile using the grating design in (b). This system is able to operate analog optical real-time data compression.

"sub-linear" and "super-linear" descriptions imply the carrier wavelength is at the center of symmetry. If the carrier is moved away from the center of symmetry, the sub-linear curve will no longer be sub-linear and the effect on the TBP will change. The S_M Distribution can be used to study such effects.

6. ANALYSIS OF TOLERANCE TO SYSTEM NONIDEALITIES

The Distribution function can also be used to assess the impact of nonidealities in the performance of TBE. In a dispersive TBE system, nonidealities include GD ripple, polarization dependence, and temperature fluctuations. The S_M Distribution visualizes the effect of nonidealities on information bandwidth and record length and provides insight into how to mitigate them.

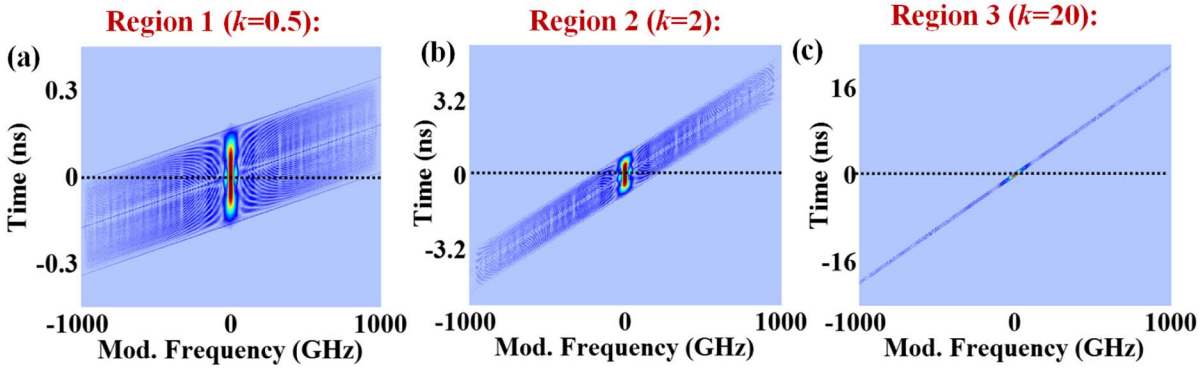

Fig. 8. Examples of S_M Distribution in three regions shown in Fig. 7(b) for a kernel with linear GD.

In the examples studied here, we consider four systems with GD profiles shown in Fig. 10. We consider operation in the far field [Figs. 10(a) and 10(b)] as well as the near field [Figs. 10(c) and 10(d)]. In each regime we consider two cases: GD ripples of less than ±4% and ±8% of the maximum GD. The far-field GD profile with 4% ripples is the experimentally measured result for a fabricated grating that was recently used to demonstrate optical real-time data compression [22] [see Fig. 10(a)]. The grating was designed to compress the bandwidth of a signal with 1 THz bandwidth to 8 GHz so it can be digitized in real time, and at the same time to compress the record length and, hence, the digital data size. For the far-field example with 8% GD ripples [Fig. 10(b)], we have simulated a GD profile with the same profile but twice the ripple amplitude. For the near-field examples, Figs. 10(c) and 10(d), we have scaled down the measured profiles in Figs. 10(a) and 10(b) 20 times.

The time domain and spectrum of the input signal are shown in Fig. 4. Figure 11 shows the S_M Distribution corresponding to the large GD profiles with 4% and 8% ripples. Since in both cases the system is operating in the far-field regime, the expected output duration is 10 ns which is the total system GD. The S_M Distribution shows that systems with 4% and 8% ripples have similar output durations (10 ns), suggesting that the effect of GD ripples on the output signal duration is very small. The S_M Distribution also shows that, in the case with 4% GD ripples, the bandwidth is compressed to the desired 8 GHz baseband bandwidth (16 GHz passband bandwidth). However, the case with 8% GD ripples results in 27 GHz bandwidth.

The S_M Distribution suggests that, depending on its relative magnitude, GD ripples can dramatically impact the TBP in a TBE system. In the present example, limiting tolerances to 4% ensures the system reaches the desired 8 GHz output bandwidth. The Distributions depicted in Fig. 11 also show that the output bandwidth in the far-field regime is mostly related to the GD ripples around the carrier frequency. This can be seen by comparing the Distribution plots in Figs. 11(a) and 11(b) to their corresponding GD profiles in Fig. 10(a) and 10(b). The large ripple in the right side in Figs. 10(a) and 10(b) results in the new track seen in their S_M plots in Fig. 11, as indicated with triangles.

The small ripple in the left side of the GD profiles in Figs. 10(a) and 10(b) results in the new track seen in their S_M plots in Fig. 11, indicated with squares. These Distributions show that these two ripples do not contribute to the output bandwidth; however, the ripples around the carrier frequency ([see zoomed plots in Figs. 10(a) and 10(b)] dramatically impact the output bandwidth [see zoomed plots in Figs. 11(a) and 11(b)].

We have also investigated the use of S_M plots to analyze the effect of ripples on the TBP in the near field. The near-field GD profiles with 4% and 8% GD ripples are shown in Figs 10(c) and 10(d). The corresponding S_M Distributions are shown in Figs. 12(a) and 12(b). In this case the Distribution plots also show that effect of GD ripples on the output duration is small and the main impact is on the output modulation bandwidth. In particular, in the case with 4% ripples the bandwidth is compressed to 200 GHz (400 GHz intensity bandwidth), as opposed to 380 GHz in the 8% case. When comparing the S_M plots in Figs. 12(a) and 12(b) to their corresponding GD profiles in Figs. 10(c) and 10(d), we find

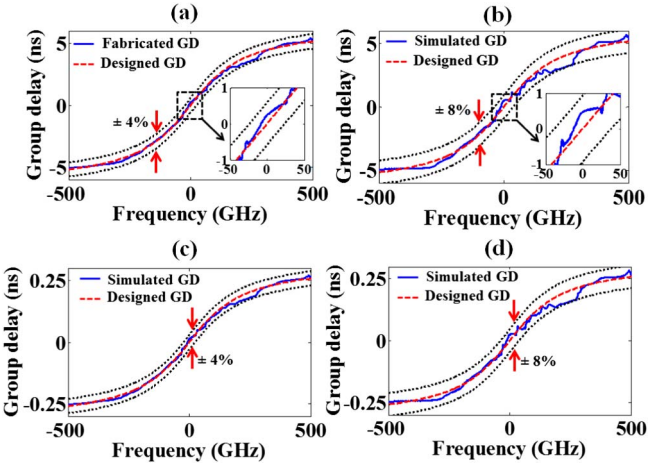

Fig. 10. Four different GD profiles used to study the effect of GD ripples on the performance of TBE systems. We consider operation in (a) and (b) the far field as well as (c) and (d) the near field. In each regime we consider two cases: GD ripples of less than ±4% and ±8% of the maximum GD. S_M Distribution plots corresponding to these profiles are shown in Figs. 11 and 12.

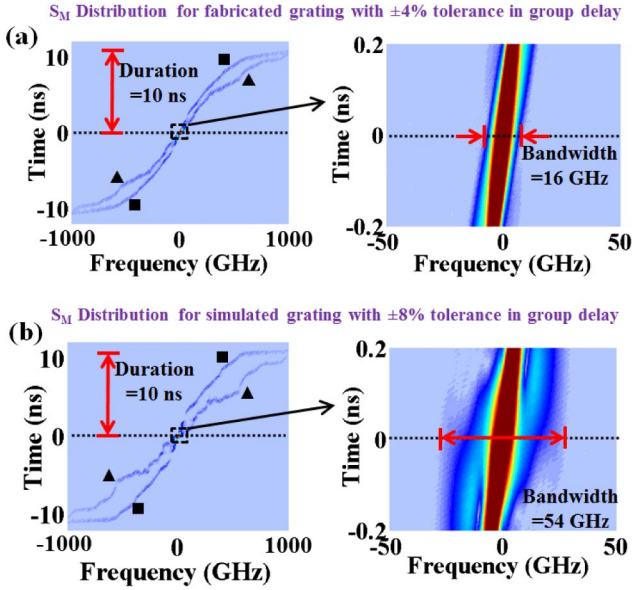

Fig. 11. S_M Distribution can be used to analyze the effect of nonidealities on the performance of TBE systems. Here we have compared S_M plots for two systems operating in the far field with (a) 4% and (b) 8% GD ripples. The GD profiles are shown in Figs. 10(a) and 10(b). The large ripple in the right side of the GD profiles in Figs. 10(a) and 10(b) results in the new track seen in their S_M plots, indicated with triangles. The small ripple in the left side of GD profiles in Figs. 10(a) and 10(b) results in the new track seen in their S_M plots, indicated with squares. This figure shows that the output modulation bandwidth in the far-field regime is determined mainly by the GD ripples at lower frequencies.

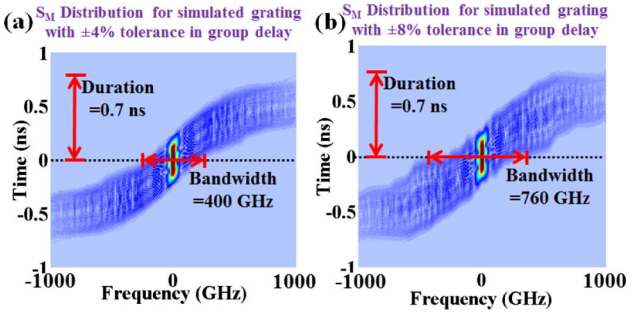

Fig. 12. Comparison of S_M Distribution plots for two systems operating in the near field with (a) 4% and (b) 8% GD ripples. The GD profiles are shown in Figs. 10(c) and 10(d). This figure shows that the output modulation bandwidth in the far-field regime is determined mainly by the GD ripples at higher frequencies.

that the large GD ripples on the right side of the profile in Fig. 10(d) have resulted in a dramatic increase in the output bandwidth. In contrast to the far-field regime, the S_M plots show that the modulation bandwidth in the near field is determined mainly by the GD ripples at higher frequencies.

7. RELATION TO ANAMORPHIC STRETCH TRANSFORM

The S_M Distribution has been used to design an anamorphic stretch transform (AST), which is a new way of compressing analog and digitized data by selectively stretching and warping the signal in the frequency domain [20,21]. AST has been used to demonstrate the first analog optical real-time data compression instrument [22]. This analog compression is achieved in an open-loop fashion, without prior knowledge of the input waveform. The discrete implementation in the form of an algorithm has been applied to digital image compression, where it has shown superior performance compared to standard image compression techniques [24].

8. RELATION TO ANAMORPHIC TEMPORAL IMAGING

The S_M Distribution has been recently used to design an analog optical transform, called anamorphic temporal imaging, for engineering the time bandwidth within a temporal imaging system. In temporal imaging systems [8,25,26], the TBP is not changed, whereas the anamorphic temporal imaging system can compress or expand the TBP [27,28].

When placed in front of a spectrometer, this technique enhances the spectral resolution $\delta\omega$ and the update rate by performing optical real-time data compression without losing information. Figure 13(a) shows a block diagram of anamorphic temporal imaging implementation. In this technique, the signal is warped in the time lens by mixing it with a local oscillator (LO) that has a nonlinear instantaneous frequency. Two power spectrum measurements are used for complex-field detection of the output signal [29]. S_M Distribution is used to design the instantaneous frequency profile in the warped time lens that leads to time–bandwidth compression. Figure 3(b) shows the qualitative S_M plots before and after an anamorphic

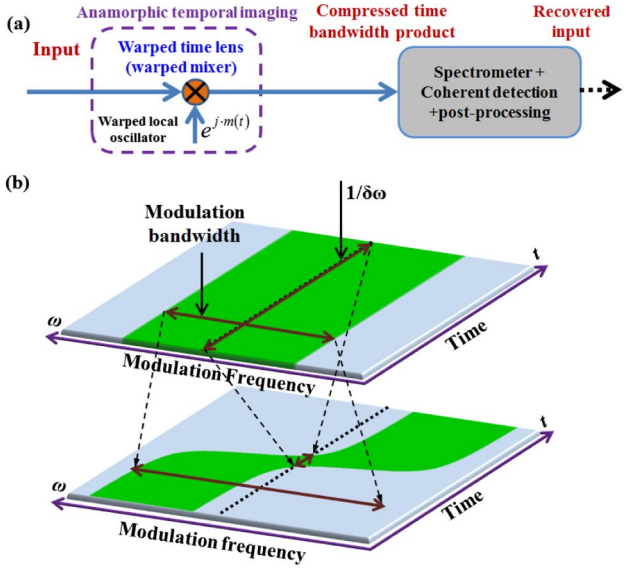

Fig. 13. (a) Block diagram of an optical anamorphic temporal imaging system for TBE using a warped optical time lens [27,28]. In this technique the signal is mixed with a local oscillator with nonlinear instantaneous frequency. (b) Qualitative S_M Distribution plots before (top) and after (bottom) anamorphic temporal imaging showing how to engineer the TBP using anamorphic temporal imaging. Using this method, spectral resolution is increased without proportional increase in the bandwidth, i.e., time–bandwidth compression. An anamorphic temporal imaging system can be also used to increase the TBP.

temporal imaging system with an LO with a sub-linear instantaneous frequency profile. As seen, spectral resolution $\delta\omega$ is increased, but the bandwidth is not expanded proportionally, i.e., time–bandwidth compression.

9. RELATION TO OTHER TIME–FREQUENCY DISTRIBUTIONS

The S_M Distribution belongs to general class of time–frequency distribution functions that includes short-time Fourier transform [30], Wigner distribution [31], and the ambiguity function [32]. Short-time Fourier transform and Wigner distribution analyze the time and frequency dependence of the signal's electric field. In contrast, S_M Distribution describes the signal's modulation intensity envelope. The ambiguity function, used mainly in pulsed radar and sonar, is a two-dimensional function of time delay and Doppler frequency [32]. None of these functions are designed for or have been used for TBE. Unique to the S_M Distribution, the built-in operation kernel enables the Distribution to show how the time duration and information bandwidth are affected when the signal is transformed by a nonlinear phase operation.

10. SUMMARY

We have described foundations of optical methods to engineer the time bandwidth of information-carrying signals. Here the time represents the record length and the bandwidth is the modulation, i.e., the information bandwidth. To design such systems, we use the S_M Distribution, a mathematical tool that describes the bandwidth and temporal duration of the signal

intensity (instantaneous power) before and after operation with a phase filter with an arbitrary GD. We provided closed-form mathematical expressions that describe how the signal's duration and bandwidth are shaped by the GD characteristics. We also showed how the Distribution can provide visual insight and tolerances to nonidealities, such as GD ripples. Finally, the mathematical tools presented in this paper offer opportunities for follow-up work directed to detailed study of different implementations of the TBE system, including studying and benchmarking various GD profiles.

FUNDING INFORMATION

Office of Naval Research (ONR) (N00014-13-1-0678).

ACKNOWLEDGMENT

The program manager for the ONR MURI program funding was Dr. Steve Pappert.

REFERENCES

1. B. Jalali, D. R. Solli, K. Goda, K. Tsia, and C. Ropers, "Real-time measurements, rare events, and photon economics," Eur. Phys. J. Spec. Top. **185**, 145–157 (2010).
2. D. R. Solli, C. Ropers, P. Koonath, and B. Jalali, "Optical rogue waves," Nature **450**, 1054–1057 (2007).
3. N. Akhmediev, A. Ankiewicz, and M. Taki, "Waves that appear from nowhere and disappear without a trace," Phys. Lett. A **373**, 675–678 (2009).
4. B. Kibler, J. Fatome, C. Finot, G. Millot, F. Dias, G. Genty, N. Akhmediev, and J. M. Dudley, "The Peregrine soliton in nonlinear fibre optics," Nat. Phys. **6**, 790–795 (2010).
5. B. Wetzel, A. Stefani, L. Larger, P. A. Lacourt, J. M. Merolla, T. Sylvestre, A. Kudlinski, A. Mussot, G. Genty, F. Dias, and J. M. Dudley, "Real-time full bandwidth measurement of spectral noise in supercontinuum generation," Sci. Rep. **2**, 882 (2012).
6. R. M. Fortenberry, W. V. Sorin, H. Lin, S. A. Newton, J. K. Andersen, and M. N. Islam, "Low-power ultrashort optical pulse characterization using linear dispersion," in *Conference on Optical Fiber Communication* (1997), pp. 290–291.
7. P. V. Kelkar, F. Coppinger, A. S. Bhushan, and B. Jalali, "Time-domain optical sensing," Electron. Lett. **35**, 1661–1662 (1999).
8. M. A. Foster, R. Salem, D. F. Geraghty, A. C. Turner-Foster, M. Lipson, and A. L. Gaeta, "Silicon-chip-based ultrafast optical oscilloscope," Nature **456**, 81–84 (2008).
9. Y. Han and B. Jalali, "Photonic time-stretched analog-to-digital converter: Fundamental concepts and practical considerations," J. Lightwave Technol. **21**, 3085–3103 (2003).
10. G. C. Valley, "Photonic analog-to-digital converters," Opt. Express **15**, 1955–1982 (2007).
11. J. Stigwall and S. Galt, "Signal reconstruction by phase retrieval and optical backpropagation in phase-diverse photonic time-stretch systems," J. Lightwave Technol. **25**, 3017–3027 (2007).
12. M. H. Asghari, Y. Park, and J. Azaña, "Complex-field measurement of ultrafast dynamic optical waveforms based on real-time spectral interferometry," Opt. Express **18**, 16526–16538 (2010).
13. K. Goda, K. K. Tsia, and B. Jalali, "Serial time-encoded amplified imaging for real-time observation of fast dynamic phenomena," Nature **458**, 1145–1149 (2009).
14. F. Qian, Q. Song, E. Tien, S. K. Kalyoncu, and O. Boyraz, "Real-time optical imaging and tracking of micron-sized particles," Opt. Commun. **282**, 4672–4675 (2009).
15. C. Zhang, Y. Qiu, R. Zhu, K. K. Y. Wong, and K. K. Tsia, "Serial time-encoded amplified microscopy (STEAM) based on a stabilized picosecond supercontinuum source," Opt. Express **19**, 15810–15816 (2011).
16. B. Jalali and M. H. Asghari, "Anamorphic stretch transform; putting the squeeze on big data," Opt. Photon. News **25**(2), 24–31 (2014).
17. B. Jalali, P. Kelkar, and V. Saxena, "Photonic arbitrary waveform generator," in *Proceedings of 14th IEEE Annual Meeting* (2001), pp. 253–254.
18. J. D. McKinney, D. S. Seo, and A. M. Weiner, "Photonically assisted generation of continuous arbitrary millemetre electromagnetic waveforms," Electron. Lett. **39**, 309–311 (2003).
19. J. Yao, F. Zeng, and Q. Wang, "Photonic generation of ultrawideband signals," J. Lightwave Technol. **25**, 3219–3235 (2007).
20. M. H. Asghari and B. Jalali, "Anamorphic transformation and its application to time-bandwidth compression," arXiv:1307.0137v4 (2013).
21. M. H. Asghari and B. Jalali, "Anamorphic transformation and its application to time-bandwidth compression," Appl. Opt. **52**, 6735–6743 (2013).
22. M. H. Asghari and B. Jalali, "Experimental demonstration of optical real-time data compression," Appl. Phys. Lett. **104**, 111101 (2014).
23. G. A. Sefler and G. C. Valley, "Mitigation of group-delay-ripple distortions for use of chirped fiber-Bragg gratings in photonic time-stretch ADCs," J. Lightwave Technol. **31**, 1093–1100 (2013).
24. M. H. Asghari and B. Jalali, "Discrete anamorphic transform for image compression," IEEE Signal Process. Lett. **21**, 829–833 (2014).
25. Y. Okawachi, R. Salem, M. A. Foster, A. C. Turner-Foster, M. Lipson, and A. L. Gaeta, "High-resolution spectroscopy using a frequency magnifier," Opt. Express **17**, 5691–5697 (2009).
26. D. H. Broaddus, M. A. Foster, O. Kuzucu, K. W. Koch, and A. L. Gaeta, "Ultrafast, single-shot phase and amplitude measurement via a temporal imaging approach," in *Conference on Lasers and Electro-Optics* (Optical Society of America, 2010), paper CMK6.
27. M. H. Asghari and B. Jalali, "Warped time lens in temporal imaging for optical real-time data compression," Chin. Sci. Bull., doi:10.1007/s11434-014-0352-0 (to be published).
28. M. H. Asghari and B. Jalali, "Anamorphic temporal imaging using a warped time lens," presented at the Conference on Lasers and Electro-Optics, San Jose, Calif., 8–14 June 2014.
29. J. Azana, Y. Park, T.-J. Ahn, and F. Li, "Simple and highly sensitive optical pulse characterization method based on electro-optic spectral signal differentiation," Opt. Lett. **33**, 437–439 (2008).
30. J. B. Allen, "Short time spectral analysis, synthesis, and modification by discrete Fourier transform," IEEE Trans. Acoust. Speech Signal Process. **25**, 235–238 (1977).
31. E. P. Wigner, "On the quantum correction for thermodynamic equilibrium," Phys. Rev. **40**, 749–759 (1932).
32. P. M. Woodward, *Probability and Information Theory, with Applications to Radar* (Pergamon, 1953).

Research Article Vol. 1, No. 1 / July 2014 / Optica 32

Radiative cooling of solar cells

Linxiao Zhu,[1] Aaswath Raman,[2] Ken Xingze Wang,[1] Marc Abou Anoma,[3] and Shanhui Fan[2,*]

[1]Department of Applied Physics, Stanford University, Stanford, California 94305, USA

[2]Department of Electrical Engineering, Ginzton Laboratory, Stanford University, Stanford, California 94305, USA

[3]Department of Mechanical Engineering, Stanford University, Stanford, California 94305, USA

*Corresponding author: shanhui@stanford.edu

Received 31 March 2014; revised 13 May 2014; accepted 17 May 2014 (Doc. ID 209022); published 22 July 2014

Standard solar cells heat up under sunlight. The resulting increased temperature of the solar cell has adverse consequences on both its efficiency and its reliability. We introduce a general approach to radiatively lower the operating temperature of a solar cell through sky access, while maintaining its solar absorption. We first present an ideal scheme for the radiative cooling of solar cells. For an example case of a bare crystalline silicon solar cell, we show that the ideal scheme can passively lower its operating temperature by 18.3 K. We then demonstrate a microphotonic design based on real material properties that approaches the performance of the ideal scheme. We also show that the radiative cooling effect is substantial, even in the presence of significant convection and conduction and parasitic solar absorption in the cooling layer, provided that we design the cooling layer to be sufficiently thin. © 2014 Optical Society of America

OCIS codes: (350.6050) Solar energy; (230.5298) Photonic crystals; (290.6815) Thermal emission.

http://dx.doi.org/10.1364/OPTICA.1.000032

From Shockley and Queisser's analysis, a single junction solar cell has a theoretical upper limit for power conversion efficiency of around 33.7% [1] under the AM1.5 solar spectrum. Thus, while a solar cell absorbs most incident solar irradiance [2,3], there is intrinsically a significant portion of absorbed solar irradiance that is not converted into electricity, and instead generates heat that, in turn, heats up the solar cell. In practice, the operating temperature of a solar cell in outdoor conditions is typically 50°C–55°C or higher [4–6]. This heating has significant adverse consequences for the performance and reliability of solar cells. The conversion efficiency of solar cells typically deteriorates at elevated temperatures. For crystalline silicon solar cells, every temperature rise of 1 K leads to a relative efficiency decline of about 0.45% [7]. Furthermore, the aging rate of a solar cell array doubles for every 10 K increase in its operating temperature [8]. Therefore, there is a critical need to develop effective strategies for solar cell cooling. Current approaches include conduction of heat to dissipation surfaces [9], forced air flow [10], hot water generation in combined photovoltaic/thermal systems [11], and heat-pipe-based systems [12,13].

In this paper, we propose the use of radiative cooling to passively lower the temperature of solar cells operating under direct sunlight. The basic idea is to place a thin material layer that is transparent over solar wavelengths but strongly emissive over thermal wavelengths on top of the solar cell. Such a layer does not degrade the optical performance of the solar cell, but does generate significant thermal radiation that results in solar cell cooling by radiatively emitting heat to outer space.

The Earth's atmosphere has a transparency window between 8 and 13 μm, which coincides with the wavelength range of thermal radiation from terrestrial bodies at typical temperatures. Terrestrial bodies can therefore cool down by sending thermal radiation into outer space. Both nighttime [14–23] and daytime [15,24–27] radiative cooling has been studied previously. Most of these studies sought to achieve an equilibrium temperature that is below the ambient air temperature. In daytime, achieving radiative cooling below ambient temperature requires reflecting over 88% of incident solar irradiance [24]. Solar cells, on the other hand, must absorb sunlight. Thus, unlike most previous radiative cooling works [15,24–26], we do not seek to achieve an equilibrium

temperature that is below the ambient. Instead, for a solar cell with a given amount of heat generated by solar absorption, our objective is to lower its operating temperature as much as possible, while maintaining its solar absorptance.

Without loss of generality, we consider crystalline silicon solar cells, representing about 90% [28] of solar cells produced worldwide in 2008. Crystalline silicon can absorb a considerable amount of solar irradiance, and has a very small extinction coefficient at thermal wavelengths at typical terrestrial temperatures. Thus, crystalline silicon solar cells represent a worst-case scenario as far as radiative cooling is concerned since they emit very small amounts of thermal radiation. In our simulations, as a model of the optical and thermal radiation properties of a silicon solar cell, we consider the structure shown in Fig. 1(a), which consists of a 200-μm-thick crystalline Si layer [29] on top of an aluminum (Al) backreflector. The silicon is p-doped with a concentration of 1.5×10^{16} cm^{-3}, which represents the typical base material of a crystalline silicon solar cell [29]. The dielectric constant of the doped silicon for optical simulation is obtained from [30]. To achieve radiative cooling of the cell, we then add a variety of structures on top of the solar cell and facing the sky, as shown in Figs. 1(b)–1(d). These additional structures are typically made of silica.

To analyze the cooling properties of each of the structures shown in Fig. 1, we use the following procedure, which integrates electromagnetic and thermal simulations. We start with an electromagnetic (EM) simulation of the structure using the rigorous coupled wave analysis (RCWA) method [31]. At thermal wavelengths, the simulation results in an absorptivity/emissivity spectrum $\epsilon(\lambda, \Omega)$. This spectrum is then used to compute the cooling power:

$$P_{\mathrm{cooling}}(T_{\mathrm{Emit}}) = P_{\mathrm{rad}}(T_{\mathrm{Emit}}) - P_{\mathrm{atm}}(T_{\mathrm{amb}}), \quad (1)$$

where

$$P_{\mathrm{rad}}(T_{\mathrm{Emit}}) = \int \mathrm{d}\Omega \cos\theta \int_0^\infty \mathrm{d}\lambda I_{BB}(T_{\mathrm{Emit}}, \lambda)\epsilon(\lambda, \Omega) \quad (2)$$

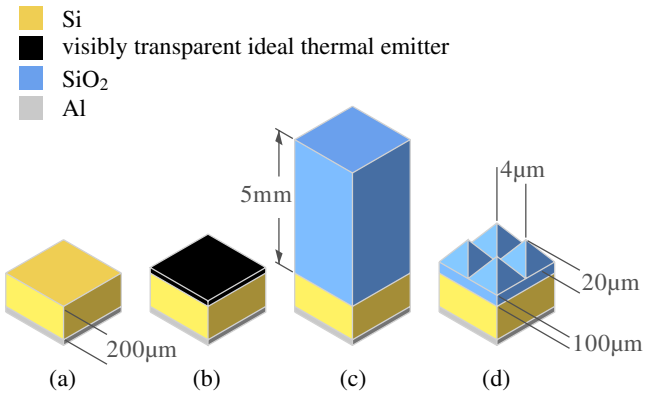

Fig. 1. 3D crystalline silicon solar cell structures. (a) Bare solar cell with 200-μm-thick uniform silicon layer, on top of an Al backreflector. (b) Thin visibly transparent ideal thermal emitter on top of the bare solar cell. (c) 5-mm-thick uniform silica layer on top of the bare solar cell. (d) 2D square lattice of silica pyramids and a 100-μm-thick uniform silica layer, on top of the bare solar cell.

is the power radiated by the structure per unit area. Here T_{Emit} is taken to be the temperature of the top surface and will be determined self-consistently when we combine the EM and thermal simulations. $\int \mathrm{d}\Omega$ is the solid angle integral over a hemisphere. $I_{BB}(T, \lambda)$ is the spectral radiance of a blackbody at temperature T, and

$$P_{\mathrm{atm}}(T_{\mathrm{atm}}) = \int \mathrm{d}\Omega \cos\theta \int_0^\infty \mathrm{d}\lambda I_{BB}(T_{\mathrm{amb}}, \lambda)\epsilon(\lambda, \Omega)\epsilon_{\mathrm{atm}}(\lambda, \Omega) \quad (3)$$

is the power absorbed from the ambient atmosphere. The angle-dependent emissivity of the atmosphere is given by [19] as $\epsilon_{\mathrm{atm}}(\lambda, \Omega) = 1 - t(\lambda)^{1/\cos\theta}$, where $t(\lambda)$ is the atmospheric transmittance in the zenith direction [32,33]. To evaluate the cooling power, we calculate the emissivity/absorptivity with a spectral resolution of 2 nm from 3 to 30 μm, and with 5 deg angular resolution across the hemisphere. With these spectral and angular resolutions, the cooling power has converged within 0.5% relative accuracy. We note that we take into account the temperature dependence of the permittivity of doped silicon [30] in the electromagnetic simulations, and the absorptivity/emissivity spectra are calculated for various temperatures of solar cells. The permittivity of silica has negligible temperature dependence.

We also use the electromagnetic simulation to determine the solar absorption profile within the silicon solar cell structure. By assuming a total heating power of the solar cell, which in practice corresponds to the difference between the absorbed solar power and extracted electrical power, we can then determine a spatially dependent heat generation rate $\dot{q}(z)$ within the silicon solar cell region.

The results from the electromagnetic simulations are then fed into a finite-difference-based thermal simulator, where we simulate the temperature distribution within the structure by solving the steady-state heat diffusion equation:

$$\frac{d}{dz}\left[\kappa(z)\frac{dT(z)}{dz}\right] + \dot{q}(z) = 0, \quad (4)$$

where $T(z)$ is the temperature distribution. In this equation, the thermal conductivity κ of silicon and of silica are taken to be 148 W/m/K and 1.4 W/m/K, respectively [34]. The schematic of the simulation is shown in Fig. 2, where the vertical direction aligns with the z axis.

The simulated region consists of the silicon solar cell and the silica structure on top of it. At the upper surface, we assume, as a boundary condition,

$$-\kappa(z)\frac{dT(z)}{dz}\Big|_{\mathrm{top}} = P_{\mathrm{cooling}}(T_{\mathrm{Emit}}) + h_1(T_{\mathrm{Emit}} - T_{\mathrm{amb}}) \quad (5)$$

to take into account both the cooling effect due to radiation, as well as additional nonradiative heat dissipation due to convection and conduction, as characterized by h_1. At the lower surface, we assume a boundary condition

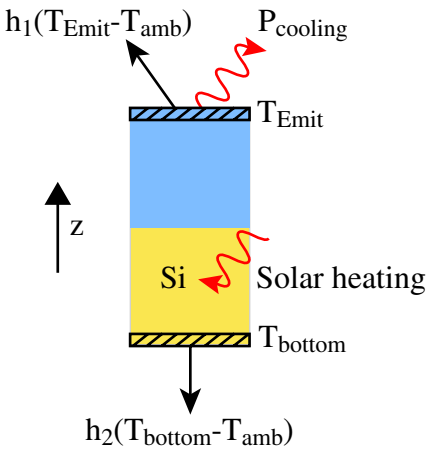

Fig. 2. Schematic of thermal simulation. h_1 and h_2 are the nonradiative heat exchange coefficients at the upper and lower surfaces, respectively. Ambient temperature is T_{amb}.

$$\kappa \frac{dT(z)}{dz}|_{bottom} = h_2(T_{bottom} - T_{amb}) \quad (6)$$

to characterize the nonradiative heat loss of the lower surface. The solution of the heat equation results in a temperature distribution T. The temperature of the upper surface is then used as T_{Emit} in Eq. (5) and input back into the boundary condition; the heat equation is then solved again. This process is iterated until self-consistency is reached, i.e., until the temperature of the upper surface no longer changes with iteration. The operating temperature of the solar cell is then defined as the spatially averaged temperature inside the silicon region.

We use a 1D thermal model for such a 3D structure because the temperature variation in the horizontal direction is sufficiently small. As a simple estimation, consider the temperature difference ΔT between the center of the pyramid and the edge for the structure in Fig. 1(d). Such a temperature difference results in a power flow of $\kappa \Delta T/d$, where $d \approx 2$ μm is the distance between the center and the edge. Such a power flow should be less than the cooling power of the device, which is 208 W/m^2 at $T = 300$ K, and 554 W/m^2 at $T = 350$ K, with $T_{amb} = 300$ K. Thus, we estimate $\Delta T \approx 8 \times 10^{-4}$ K. This is sufficiently small to justify the use of a 1D thermal model.

As a typical scenario, we consider the ambient on both sides of solar cell to be at 300 K. The nonradiative heat exchange coefficients are $h_1 = 12$ W/m^2/K and $h_2 = 6$ W/m^2/K, corresponding to wind speeds of 3 m/s and 1 m/s [25]. The annual average wind speed at a height of 30 m in most parts of the United States is at or below 4 m/s [35]. The wind speed at a height of 10 m, which is more relevant to solar cell installations, can be estimated from the horizontal wind speed at 30 m by using the 1/7 power law [36], to be below $4 \times (10/30)^{1/7} = 3.4$ m/s. h_2 is chosen to reflect the fact that the wind speed on the unexposed rear side of solar cells is smaller than the exposed front side [5].

Using the numerical procedure outlined above, we now present simulation results on the configurations shown in Fig. 1. Without any radiative cooling structure on top, the solar cell structure shown in Fig. 1(a) (which we will refer to as the "bare solar cell" below) heats up substantially above the ambient for various solar heating powers (Fig. 3, blue curve). At 800 W/m^2 solar heating power, corresponding approximately to the expected heat output of a crystalline solar cell under peak unconcentrated solar irradiance, the bare solar cell operates at 42.3 K above ambient.

To radiatively cool the solar cell, our design principle is to place on top of the bare solar cell a layer that emits strongly in the thermal wavelength range, while being transparent at solar wavelengths. To illustrate the theoretical potential of this idea, we first consider the ideal scenario [Fig. 1(b)] where the added layer has unity emissivity in the wavelength range above 4 μm, and has zero emissivity below 4 μm. Such a layer has maximal thermal radiative power, and, in the meantime, does not absorb sunlight; hence, it has maximal cooling power. With such an ideal layer added, the solar cell operates at a substantially lower temperature (Fig. 3, green curve), as compared to the bare solar cell case. At 800 W/m^2 solar heating power, the solar cell with the ideal cooling layer operates at a temperature that is 18.3 K lower as compared to the bare solar cell. The calculation here points to the significant theoretical potential of using radiative cooling in solar cells.

To implement the concept of radiative cooling for solar cells we consider the use of silica as the material for the cooling layer. Pure silica is transparent over solar wavelengths and has pronounced phonon–polariton resonances, and hence emissivity, at thermal wavelengths. Standard solar panels are typically covered with glass, which contains 70% to 80% silica [37] and, therefore, potentially provide some radiative cooling benefit already. As we will show here, however, the cooling performance of a thick and flat layer of silica is significantly lower than the theoretical potential. Moreover, as we discuss later, typical solar absorption in glass significantly counteracts the potential radiative benefit it provides. Emulating the geometry of a typical solar panel cover glass, we examine a thermal emitter design consisting of a 5-mm-thick uniform *pure* silica

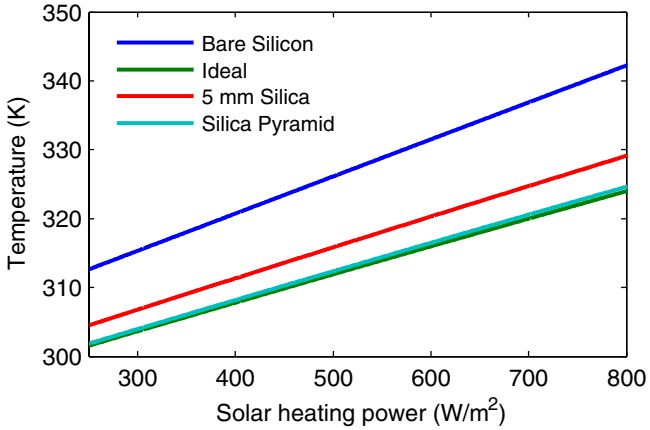

Fig. 3. Operating temperature of solar cells with the thermal emitter designs in Fig. 1, for different solar heating power. The nonradiative heat exchange coefficients are $h_1 = 12$ W/m^2/K (corresponding to 3 m/s), and $h_2 = 6$ W/m^2/K (corresponding to 1 m/s). The ambient temperatures at the top and the bottom are both 300 K.

layer on top of the bare solar cell [Fig. 1(c)]. The use of the 5-mm-thick uniform silica layer (Fig. 3, red curve) does enable an operating temperature considerably lower than that of the bare solar cell. However, the radiative cooling performance of 5-mm-thick uniform silica is inferior to the ideal case. At 800 W/m^2 solar heating power, solar cell with 5-mm-thick uniform silica operates at a temperature 5.2 K higher than the ideal case (Fig. 3, green curve).

We now present a microphotonic design, shown in Fig. 1(d), that has performance that approaches the ideal case. The thermal emitter design consists of a 2D square lattice of silica pyramids, with 4 μm periodicity and 20 μm height, on top of a 100-μm-thick uniform silica layer. We refer to this design as a "silica pyramid" design. Such a silica pyramid design substantially lowers the temperature of the solar cell (Fig. 3, cyan curve). It considerably outperforms the 5-mm-thick uniform silica design, and has performance nearly identical to the ideal scheme. At 800 W/m^2 solar heating power, the temperature reduction of the silica pyramid design is 17.6 K, compared with the bare solar cell. Using [7], we estimate that such a temperature drop should result in a relative efficiency increase of about 7.9%. If the solar cell efficiency is 20%, this temperature drop corresponds to a 1.6% absolute efficiency increase, which is a significant improvement of solar cell efficiency.

To reveal the mechanism underlying the different cooling performance, we examine the emissivity spectra of the different designs at thermal wavelengths in Fig. 4. The bare solar cell has only small emissivity at thermal wavelengths (Fig. 4, blue curve). Accordingly, the solar cell heats up substantially.

For the ideal case (Fig. 4, green curve), the emissivity at thermal wavelengths is unity, which enables the structure to radiatively cool maximally.

For the uniform silica layer (Fig. 4, red curve), the emissivity at thermal wavelengths is considerable. However, the emissivity spectrum shows two large dips near 10 and 20 μm. These dips correspond to the phonon–polariton resonances of silica. At these wavelengths, silica has a large extinction coefficient, and there is a strong impedance mismatch between silica and air. The large impedance mismatch results in large reflectivity, and accordingly small absorptivity/emissivity. These dips coincide with the 8–13 μm atmospheric transmission window and a secondary atmospheric transmission window at 20–25 μm [26], respectively. Moreover, the dip near 10 μm coincides with the peak blackbody radiation wavelength of 9.7 μm for the typical terrestrial temperature of 300 K. Therefore, the cooling capability of 5-mm-thick uniform silica is inferior to the ideal case.

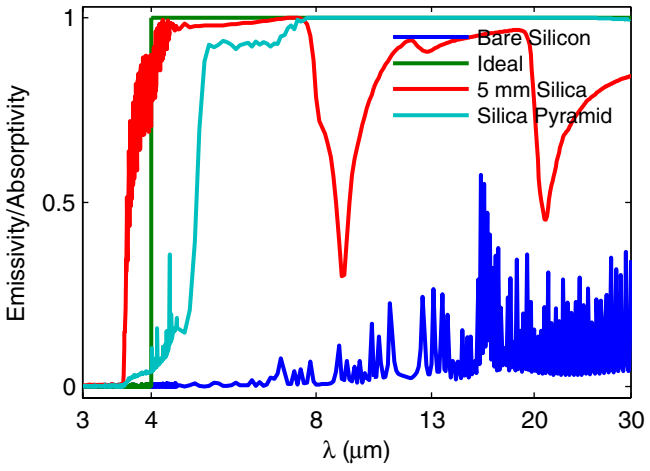

Fig. 4. Emissivity and absorptivity spectra of solar cells with different thermal emitter designs in Fig. 1, for normal direction and after averaging over polarizations. The temperature of solar cells is 300 K.

The silica pyramid design, however, has emissivity very close to unity at the whole range of thermal wavelengths (Fig. 4, cyan curve). Comparing with the uniform silica structure, we observe that the use of the pyramid eliminates the two dips near 10 and 20 μm. In the silica pyramid design, the absence of sharp resonant features associated with silica phonon–polariton resonances and, hence, broadband near-unity absorption is achieved because the pyramids provide a gradual refractive index change to overcome the impedance mismatch between silica and air at a broad range of wavelengths, including the phonon–polariton resonant wavelengths.

We have focused on designing a thin material layer that generates significant thermal radiation, while being optically transparent so that it does not degrade the optical performance of the solar cell. The silica pyramid has a size of several micrometers, and is significantly larger than wavelengths in the solar spectrum. Due to this strong size contrast, the silica pyramid does not degrade solar absorptivity. This remains true even in the presence of an antireflection layer. As an example, we show that, for a solar cell with a 75 nm silicon nitride layer on top as antireflection coating, the silica pyramid design does not degrade the solar absorptivity (see Supplement 1). Our proposed silica pyramid structure for enhancing thermal radiation is thus compatible with antireflection coating design, by not degrading the solar absorptivity of the solar cell.

Practical solar cell structures cool down through nonradiative cooling. The top surface of the cell structure may be exposed to wind, while additional cooling systems may be put at the bottom of the cell. These nonradiative cooling mechanisms are characterized by the h_1 and h_2 coefficients in Eqs. (5) and (6). Here we evaluate the impact of radiative cooling as we vary the strength of these nonradiative cooling mechanisms. As an example, we fix the solar heating power to be 800 W/m^2. In general, as expected, as we increase the strength of nonradiative cooling mechanisms, the solar cell temperature decreases. The impact of radiative cooling, as measured by the temperature difference between the bare solar cell and the cell structures with radiative cooling layers, also decreases. Nevertheless, even in the presence of significant nonradiative cooling, radiative cooling can still have a significant impact. For example, as shown in Fig. 5(a), with $h_1 = 40$ W/m^2/K, which corresponds to a wind speed of 12 m/s on the top surface [25], the temperature difference between the bare solar cell and the cell with silica pyramid is still as high as 5.3 K. We also note that, in the presence of strong nonradiative cooling, the impact of radiative cooling is more significant in the thin silica pyramid structure as compared to the thicker uniform silica structure. This is related to

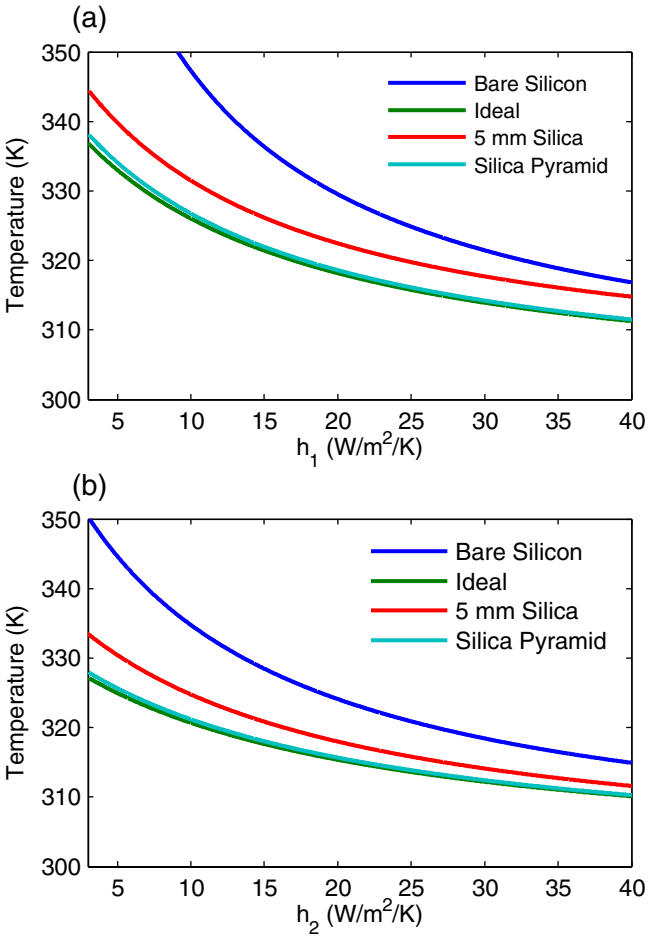

Fig. 5. (a) Operating temperature of the solar cell under different emitter designs, for different h_1, and fixed $h_2 = 6$ W/m^2/K. (b) Operating temperature of the solar cell under different emitter designs, for different h_2, and fixed $h_1 = 12$ W/m^2/K. The ambient temperature at both sides of the solar cell is 300 K. The solar heating power is 800 W/m^2.

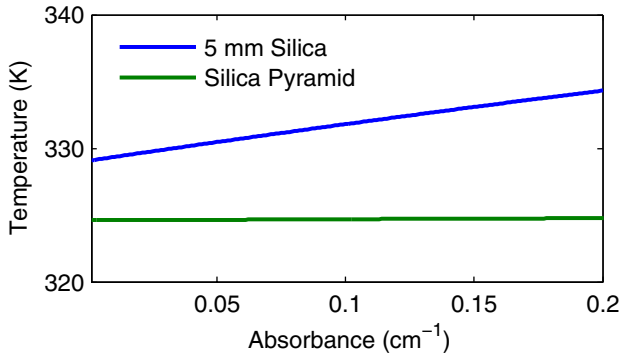

Fig. 6. Solar cell operating temperature, with a 5-mm-thick uniform silica layer (blue curve) and with the silica pyramid structure (green curve), where a constant absorbance at solar wavelengths has been artificially added to the material silica. $h_1 = 12$ m/s, $h_2 = 6$ m/s. The ambient temperatures at both sides of the solar cell is 300 K. The solar heating power is 800 W/m^2.

the larger thermal resistance in the thicker silica structure, which further diminishes the benefits of the radiative cooling.

In the simulations above, we have assumed the use of silica that is transparent in the solar wavelength range. In practice, the glass used as solar panel cover contains 70%–80% silica, with the rest being Na_2O, CaO, MgO, Al_2O_3, B_2O_3, K_2O, and Fe_2O_3 [37]. Glass, therefore, has a non-negligible amount of absorption in the solar wavelength range. To assess the sensitivity of the radiative cooling performance to absorption of solar irradiance inside the thermal emitter, we add a constant absorbance to the dielectric function of silica at solar wavelengths, for the devices in Figs. 1(c) and 1(d), and compute the resulting solar cell temperature as a function of the absorbance in the silica region, as shown in Fig. 6. In Fig. 6, the 5-mm-thick uniform silica design is sensitive to possible absorption of solar irradiance inside the thermal emitter. With a relatively small absorbance of 0.2 cm^{-1}, its operating temperature increases by 5.2 K, reducing by nearly half the radiative cooling benefit of using 5-mm-thick silica. In contrast, the performance of the silica pyramid design remains unchanged for this level of absorbance of solar irradiance inside the thermal emitter. The large contrast in the sensitivities to solar absorption inside the thermal emitter between the two designs results from the contrast in the thickness of the thermal emitter.

In summary, we have introduced the principle of radiative cooling of solar cells. We identify the ideal scheme as placing a thin, visibly transparent ideal thermal emitter atop the solar cell. While conventional solar cells have a thick cover glass panel, we show that such a glass panel can have only limited cooling performance due to its inherent thermal resistance and solar absorption. We have designed a thin, microphotonic thermal emitter based on silica pyramid arrays that approaches the performance of the ideal thermal emitter.

We remark on a few practical aspects related to our proposal. First of all, the choice of a crystalline silicon solar cell is not intrinsic to the performance of the radiative cooling, and the idea of utilizing microphotonic design to enhance thermal emission for solar cell radiative cooling should also apply to other types of solar cells. Second, in terms of experimental fabrication, nanocone or microcone structures with aspect ratio similar to our proposed pyramid structure here can be fabricated using various methods, including Langmuir–Blodgett assembly and etching [38,39] and metal-dotted pattern and etching [40]. Therefore, our proposed pyramid structure should be within the regime where fabrication can be conducted. Third, it has been demonstrated in solar cells that a microstructure patterning [41] with aspect ratio similar to the silica pyramid, or nanostructure patterning [42], has superhydrophobicity and self-cleaning functionality. This functionality prevents dust accumulation, which would otherwise block sunlight and impair solar cell performance. Furthermore, patterning of microscale pyramids with rounded tips [43], or microcone patterning [44], has been shown to have superhydrophobicity and self-cleaning properties. Therefore, our proposed silica pyramid structure may readily have self-cleaning functionality, which prevents dust accumulation on solar cells, after a surface hydrophobilization process. As the surface hydrophobilization process only involves bonding a single-layer of hydrophobic molecules, it maintains optical transparency. Finally, the strict periodicity of the silica pyramid

structure may not be necessary, as long as the structure possesses a spatial gradient in effective dielectric function to overcome the impedance mismatch between silica and air at thermal wavelengths.

Our study exploits an untapped degree of freedom for improving solar cell efficiency by engineering the thermal emission of solar cells through microphotonic design. Our analysis is based on direct simulation of 3D structures with realistic material properties, representing typical terrestrial photovoltaic operating conditions. The photonic thermal emitter design that approaches the maximal radiative cooling capability for solar cells may also provide additional opportunity for improving solar cell performance in space applications, where thermal radiation is the only cooling mechanism.

FUNDING INFORMATION

Advanced Research Projects Agency-Energy, U.S. Department of Energy (ARPA-E) (DE-AR0000316).

See Supplement 1 for supporting content.

REFERENCES

1. W. Shockley and H. J. Queisser, "Detailed balance limit of efficiency of p-n junction solar cells," J. Appl. Phys. **32**, 510–519 (1961).
2. R. Santbergen and R. van Zolingen, "The absorption factor of crystalline silicon PV cells: a numerical and experimental study," Sol. Energy Mater. Sol. Cells **92**, 432–444 (2008).
3. R. Santbergen, J. Goud, M. Zeman, J. van Roosmalen, and R. van Zolingen, "The AM1.5 absorption factor of thin-film solar cells," Sol. Energy Mater. Sol. Cells **94**, 715–723 (2010).
4. J. Ingersoll, "Simplified calculation of solar cell temperatures in terrestrial photovoltaic arrays," J. Sol. Energy Eng. **108**, 95–101 (1986).
5. A. Jones and C. Underwood, "A thermal model for photovoltaic systems," Sol. Energy **70**, 349–359 (2001).
6. M. W. Davis, A. H. Fanney, and B. P. Dougherty, "Prediction of building integrated photovoltaic cell temperatures," J. Sol. Energy Eng. **123**, 200–210 (2001).
7. E. Skoplaki and J. Palyvos, "On the temperature dependence of photovoltaic module electrical performance: a review of efficiency/power correlations," Sol. Energy **83**, 614–624 (2009).
8. D. Otth and R. E. Ross, Jr., "Assessing photovoltaic module degradation and lifetime from long term environmental tests," Proceedings of the 1983 Institute of Environmental Sciences 29th Annual Meeting, Los Angeles, CA, April 19–21 1983, pp. 121–126.
9. A. Luque and G. Araújo, *Solar Cells and Optics for Photovoltaic Concentration*, Adam Hilger Series on Optics and Optoelectronics (Institute of Physics Publishing, 1989).
10. H. Teo, P. Lee, and M. Hawlader, "An active cooling system for photovoltaic modules," Appl. Energy **90**, 309–315 (2012).
11. G. Mittelman, A. Kribus, and A. Dayan, "Solar cooling with concentrating photovoltaic/thermal (CPVT) systems," Energy Convers. Manage. **48**, 2481–2490 (2007).
12. A. Akbarzadeh and T. Wadowski, "Heat pipe-based cooling systems for photovoltaic cells under concentrated solar radiation," Appl. Therm. Eng. **16**, 81–87 (1996).
13. A. Royne, C. Dey, and D. Mills, "Cooling of photovoltaic cells under concentrated illumination: a critical review," Sol. Energy Mater. Sol. Cells **86**, 451–483 (2005).
14. F. Trombe, "Perspectives sur l'utilisation des rayonnements solaires et terrestres dans certaines régions du monde," Rev. Gen. Therm. **6**, 1285–1314 (1967).
15. S. Catalanotti, V. Cuomo, G. Piro, D. Ruggi, V. Silvestrini, and G. Troise, "The radiative cooling of selective surfaces," Sol. Energy **17**, 83–89 (1975).
16. B. Bartoli, S. Catalanotti, B. Coluzzi, V. Cuomo, V. Silvestrini, and G. Troise, "Nocturnal and diurnal performances of selective radiators," Appl. Energy **3**, 267–286 (1977).
17. A. Harrison and M. Walton, "Radiative cooling of TiO_2 white paint," Sol. Energy **20**, 185–188 (1978).
18. C. G. Granqvist and A. Hjortsberg, "Letter to the editor," Sol. Energy **24**, 216 (1980).
19. C. G. Granqvist, "Radiative cooling to low temperatures: general considerations and application to selectively emitting SiO films," J. Appl. Phys. **52**, 4205–4220 (1981).
20. P. Berdahl, "Radiative cooling with MgO and/or LiF layers," Appl. Opt. **23**, 370–372 (1984).
21. G. Smith, "Amplified radiative cooling via optimised combinations of aperture geometry and spectral emittance profiles of surfaces and the atmosphere," Sol. Energy Mater. Sol. Cells **93**, 1696–1701 (2009).
22. A. R. Gentle and G. B. Smith, "Radiative heat pumping from the Earth using surface phonon resonant nanoparticles," Nano Lett. **10**, 373–379 (2010).
23. A. Gentle, J. Aguilar, and G. Smith, "Optimized cool roofs: integrating albedo and thermal emittance with R-value," Sol. Energy Mater. Sol. Cells **95**, 3207–3215 (2011).
24. T. M. Nilsson, G. A. Niklasson, and C. G. Granqvist, "A solar reflecting material for radiative cooling applications: ZnS pigmented polyethylene," Sol. Energy Mater. Sol. Cells **28**, 175–193 (1992).
25. T. M. Nilsson and G. A. Niklasson, "Radiative cooling during the day: simulations and experiments on pigmented polyethylene cover foils," Sol. Energy Mater. Sol. Cells **37**, 93–118 (1995).
26. E. Rephaeli, A. Raman, and S. Fan, "Ultrabroadband photonic structures to achieve high-performance daytime radiative cooling," Nano Lett. **13**, 1457–1461 (2013).
27. L. Zhu, A. Raman, and S. Fan, "Color-preserving daytime radiative cooling," Appl. Phys. Lett. **103**, 223902 (2013).
28. T. Saga, "Advances in crystalline silicon solar cell technology for industrial mass production," NPG Asia Mater. **2**, 96–102 (2010).
29. A. Goetzberger, J. Knobloch, and B. Voss, "High efficiency solar cells," in *Crystalline Silicon Solar Cells* (Wiley, 1998), Chap. 6, p. 122.
30. C. Fu and Z. Zhang, "Nanoscale radiation heat transfer for silicon at different doping levels," Int. J. Heat Mass Transfer **49**, 1703–1718 (2006).
31. V. Liu and S. Fan, "S4: A free electromagnetic solver for layered periodic structures," Comput. Phys. Commun. **183**, 2233–2244 (2012).
32. S. D. Lord, "A new software tool for computing Earth's atmospheric transmission of near- and far-infrared radiation," NASA Technical Memorandum 103957 (1992).
33. Gemini Observatory, IR Transmission Spectra, http://www.gemini.edu/?q=node/10789.
34. W. Haynes, *CRC Handbook of Chemistry and Physics*, 94th ed. (Taylor & Francis, 2013).
35. United States Department of Energy, United States Residential-Scale 30-Meter Wind Maps, http://apps2.eere.energy.gov/wind/windexchange/windmaps/residential_scale.asp.
36. E. Peterson and J. P. Hennessey, Jr., "On the use of power laws for estimates of wind power potential," J. Appl. Meteorol. **17**, 390–394 (1978).
37. C. R. Kurkjian and W. R. Prindle, "Perspectives on the history of glass composition," J. Am. Ceram. Soc. **81**, 795–813 (1998).
38. C.-M. Hsu, S. T. Connor, M. X. Tang, and Y. Cui, "Wafer-scale silicon nanopillars and nanocones by Langmuir–Blodgett assembly and etching," Appl. Phys. Lett. **93**, 133109 (2008).
39. S. Wang, B. D. Weil, Y. Li, K. X. Wang, E. Garnett, S. Fan, and Y. Cui, "Large-area free-standing ultrathin single-crystal silicon as processable materials," Nano Lett. **13**, 4393–4398 (2013).
40. H. Toyota and K. Takahara, "Fabrication of microcone array for antireflection structured surface using metal dotted pattern," Jpn. J. Appl. Phys. **40**, L747–L749 (2001).

41. Y.-B. Park, H. Im, M. Im, and Y.-K. Choi, "Self-cleaning effect of highly water-repellent microshell structures for solar cell applications," J. Mater. Chem. **21**, 633 (2011).
42. J. Zhu, C.-M. Hsu, Z. Yu, S. Fan, and Y. Cui, "Nanodome solar cells with efficient light management and self-cleaning," Nano Lett. **10**, 1979–1984 (2010).
43. M. Nosonovsky and B. Bhushan, "Roughness-induced superhydrophobicity: a way to design non-adhesive surfaces," J. Phys. Condens. Matter **20**, 225009 (2008).
44. E. Hosono, S. Fujihara, I. Honma, and H. Zhou, "Superhydrophobic perpendicular nanopin film by the bottom-up process," J. Am. Chem. Soc. **127**, 13458–13459 (2005).

Research Article Vol. 1, No. 1 / July 2014 / Optica 39

Tabletop nanometer extreme ultraviolet imaging in an extended reflection mode using coherent Fresnel ptychography

MATTHEW D. SEABERG,* BOSHENG ZHANG, DENNIS F. GARDNER, ELISABETH R. SHANBLATT, MARGARET M. MURNANE, HENRY C. KAPTEYN, AND DANIEL E. ADAMS

JILA, University of Colorado at Boulder, Boulder, Colorado 80309, USA

**Corresponding author: matthew.seaberg@colorado.edu*

Received 27 March 2014; revised 27 May 2014; accepted 6 June 2014 (Doc. ID 208940); published 22 July 2014

We demonstrate the first (to our knowledge) general purpose full-field reflection-mode extreme ultraviolet (EUV) microscope based on coherent diffractive imaging. This microscope is capable of nanoscale amplitude and phase imaging of extended surfaces at an arbitrary angle of incidence in a noncontact, nondestructive manner. We use coherent light at 29.5 nm from high-harmonic upconversion to illuminate a surface, directly recording the scatter as the surface is scanned. Ptychographic reconstruction is then combined with tilted plane correction to obtain an image with amplitude and phase information. The image quality and detail from this diffraction-limited tabletop EUV microscope compares favorably with both scanning electron microscope and atomic force microscope images. The result is a general and completely extensible imaging technique that can provide a comprehensive and definitive characterization of how light at any wavelength scatters from a surface, with imminent feasibility of elemental imaging with few-nanometer resolution. © 2014 Optical Society of America

OCIS codes: (120.5050) Phase measurement; (180.0180) Microscopy; (180.7460) X-ray microscopy; (190.2620) Harmonic generation and mixing.

http://dx.doi.org/10.1364/OPTICA.1.000039

1. INTRODUCTION

Dramatic advances in coherent diffractive imaging (CDI) using light in the extreme ultraviolet (EUV) and x-ray regions of the spectrum over the past 15 years have resulted in near-diffraction-limited imaging capabilities using both large- and small-scale light sources [1,2]. In CDI, also called "lensless imaging," coherent light illuminates a sample, and the scattered light is directly captured by a detector without any intervening imaging optic. Phase retrieval algorithms are then applied to the data set to recover an image. CDI has already been used to study a variety of biological and materials systems [3–7]. However, the potential for harnessing the power of CDI for imaging complex nanostructured surfaces, which requires the use of a reflection geometry for imaging, has been much less studied. Surfaces are critical in nanoscience and nanotechnology, for example, in catalysis, energy harvesting systems, or nanoelectronics. A few successful demonstrations have applied EUV/x-ray CDI to reflection-mode imaging. However, work to date has either been limited to highly reflective EUV lithography masks in a normal incidence geometry [8], restricted to a low numerical aperture through the use of a transmissive mask [9], or restricted to isolated objects [10,11].

Here we demonstrate the most general reflection-mode CDI to date using any light source, by combining curved-wavefront ptychography CDI [12–14] with tilted plane correction [15]. This allows extended (nonisolated) objects to be imaged at any angle, which will enable tomographic imaging of surfaces. Previously, reflection-mode ptychography was limited to a normal-incidence geometry [8,16]. This work also represents the first non-isolated-object, high-fidelity, tabletop EUV coherent reflection imaging, which expands the scope of applications for CDI significantly to a very broad range of

science and technology. First, our approach removes restrictions on the numerical aperture, sample, and angle, so that general extended objects can be imaged in reflection mode at any angle of incidence. Second, illumination of the sample with a strongly curved wavefront removes the need for a zero-order beam stop by reducing the dynamic range of the diffraction patterns. The curved illumination also allows the size of the beam to vary according to the sample size, alleviating the need for a large number of scan positions. This also results in fewer necessary scan positions when imaging a large field of view. Third, reflection ptychography produces surface images containing quantitative amplitude and phase information about the sample that are in excellent agreement with atomic force microscopy (AFM) and scanning electron microscopy (SEM) images, and also removes all negative effects of nonuniform illumination of the sample or imperfect knowledge of the sample position as it is scanned [17]. The result is a general and extensible imaging technique that can provide a comprehensive and definitive characterization of how light at any wavelength scatters from an object, with the resolution limited only by the wavelength and the numerical aperture of the system. This complete amplitude and phase characterization, thus, is fully capable of pushing full-field optical imaging to its fundamental limit. Finally, because we use a tabletop high harmonic generation (HHG) 30 nm source [18], in the future it will be possible to image energy, charge, and spin transport with nanometer spatial and femtosecond temporal resolution on nanostructured surfaces or buried interfaces, which is a grand challenge in nanoscience and nanotechnology [19,20].

It is worth briefly reviewing the relationship between our work presented here and that of Bragg ptychography CDI [21,22], which has become a very useful technique for quantitative visualization of nanoscale strain in crystalline structures. The experimental geometry for Bragg ptychography CDI is qualitatively similar to that presented here; a surface is illuminated in an off-axis geometry, with diffraction intensities measured in the far field. However, this technique requires an object with a crystalline structure to be illuminated by x-ray light with a wavelength shorter than the lattice constant, and is therefore complementary.

2. EXPERIMENT

The experimental geometry for reflection-mode Fresnel ptychography is shown in Fig. 1. A Ti:sapphire laser beam with wavelength ≈785 nm (1.5 mJ pulse energy, 22 fs pulse duration, 5 kHz repetition rate) is coupled into a 5 cm long, 200 μm inner diameter hollow waveguide filled with 60 Torr of argon. Bright harmonics of the fundamental laser are produced near a center wavelength of 29.5 nm (27th harmonic), since the HHG process is well phase matched [23], ensuring strong coherent signal growth and high spatial coherence. The residual fundamental laser light, which is collinear with the high harmonic beam, is filtered out using a combination of two silicon mirrors (placed near Brewster's angle for 785 nm light) and two 200 nm thick aluminum filters. The EUV beam is then sent through an adjustable ≈1 mm aperture placed ≈1 m upstream of the sample to remove any stray light outside

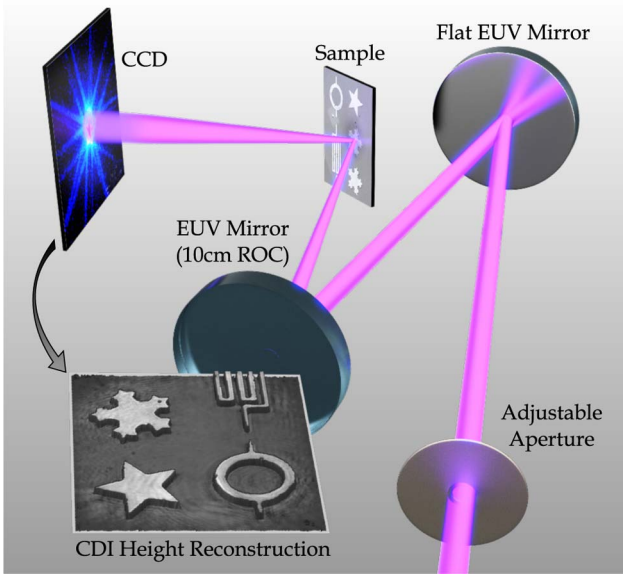

Fig. 1. Experimental setup for reflection-mode Fresnel ptychography. The EUV beam propagates through an adjustable ≈1 mm aperture; a single harmonic is selected using a pair of multilayer mirrors centered at 29.5 nm and focused onto the sample. The scattered light is collected on a CCD detector placed directly after the sample. The inset shows a height profile reconstructed through ptychography.

the beam radius. A pair of Mg/SiC multilayer mirrors then select the 27th harmonic of the Ti:sapphire laser at 29.5 nm. The first mirror is flat, while the second mirror has a radius of curvature (ROC) of 10 cm. This mirror pair focuses the HHG beam onto the sample at an angle of incidence of 45°. The focus position is 300 μm downstream of the sample, so that the HHG beam wavefront at the sample plane has significant curvature. The angle of incidence on the curved mirror is approximately 2°, which introduces small amounts of astigmatism and coma onto the HHG beam.

The sample consisted of ≈30 nm thick titanium patterned on a silicon substrate using e-beam lithography (see Supplement 1, Appendix C). An SEM image of this object is shown in Fig. 2(b). The scattered light from the object was measured using an EUV-sensitive CCD detector (Andor iKon, 2048 × 2048, 13.5 μm square pixels) placed 67 mm from the object and oriented so that the detector surface was normal to the specular reflection of the beam. The sample was positioned 300 μm before the circle of least confusion along the beam axis, so that the beam diameter incident on the sample was approximately 10 μm. Diffraction patterns were measured at each position of 10 adjacent 3 × 3 grids, with a 2.5 μm step size between positions. The positions were randomized by up to 1 μm in order to prevent periodic artifacts from occurring in the ptychographic reconstruction [24].

3. RESULTS AND DISCUSSION

Due to the non-normal angle-of-incidence on the sample, the patterns must be remapped onto a grid that is linear in spatial frequencies of the sample plane, in order to use fast Fourier transforms in the data analysis. We used tilted plane correction

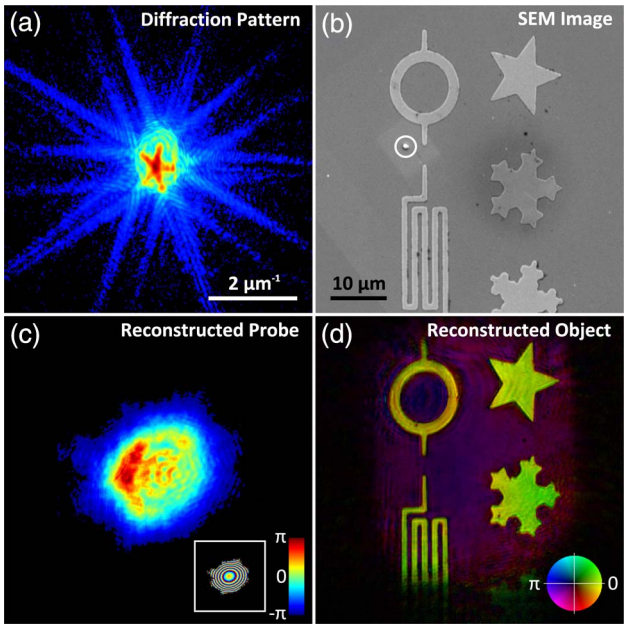

Fig. 2. Diffraction data and ptychographic reconstruction. (a) Representative diffraction pattern, scaled to the 1/4 power, taken from the 90-scan dataset. (b) SEM image of the Ti-patterned Si sample. Note that the large defect circled in the SEM image resulted from contamination after the ptychography measurement. (c) Reconstructed amplitude (thresholded at 5%) of the HHG beam. The inset shows the reconstructed phase (displayed modulo-2π). (d) Ptychographic reconstruction of the object shown in part (b). The reconstruction is plotted as the complex amplitude, where brightness represents reflected amplitude and hue represents the phase of the reconstruction. Note that the majority of defects seen in the SEM image of the Ti nanostructures are reproduced in the ptychographic reconstruction. The scale bar in (b) is shared among (b)–(d).

to accomplish this [15]. An example of a corrected diffraction pattern is shown in Fig. 2(a). The diffraction patterns were cropped such that the effective numerical aperture was 0.1, enabling a half-pitch resolution of 150 nm. The image was reconstructed using the extended ptychographical iterative engine (ePIE), along with the subpixel position determination method [17,25] (see Supplement 1, Appendix C, for details). A starting guess for the probe was calculated based on the estimated distance of the sample from the focus. The reconstructed complex amplitude of the object is shown in Fig. 2(d). During the course of the reconstruction, the algorithm was used to further solve for the complex amplitude of the probe as well, resulting in the illumination shown in Fig. 2(c). As discussed in Supplement 1, Appendix A, the reconstructed probe is completely consistent with a measurement of the unscattered beam at the detector. The high fidelity of the CDI reconstruction is evident in the fact that the majority of small defects visible in the SEM image of the Ti patterns [Fig. 2(b)] are also clearly visible in the CDI reconstruction [Fig. 2(d)]. Note that the large defect circled in the SEM image in Fig. 2(b) was the result of sample contamination after the ptychography measurement. Supplement 1, Appendix B, contains a more detailed comparison between the defects seen in the CDI reconstruction and those seen in the SEM and AFM images (Fig. S3). Small artifacts are present at the periphery of the reconstruction, due to fewer overlapping scan positions in this region. With a larger scan, these artifacts will be completely eliminated for any structure of interest that is not near the edge of the scan range.

Ptychography solves for the complex amplitudes of both the object and the probe (or incident beam) simultaneously [12,24]. As a result, reliable quantitative information about the object can be obtained from the reconstruction, since the effect of the probe on the diffraction patterns is essentially divided out. Quantitative surface relief information can be obtained from the phase of the reconstructed object as well. The titanium was patterned at a thickness of approximately 30 nm. The round-trip path difference of the reflected light is $-2h\cos\theta$, where h is the height above a reference (such as the substrate) and θ is the angle of incidence. At a 45° angle of incidence for a feature thickness of 30 nm, the round-trip path length difference between the silicon substrate and the patterned titanium features is 42.4 nm. At a 29.5 nm wavelength, this corresponds to between one and two wavelengths' path length difference. Additionally, the phase change upon reflection can be highly variable for absorbing materials. In the case of this sample, both silicon and titanium have native oxide layers that must be taken into account when calculating this phase change. Thus, some prior knowledge is required in order to retrieve the absolute height of the features. The method for calculating the phase change upon reflection from a thin-film system with complex indices of refraction is described in Born and Wolf [26]. The indices of refraction at the 29.5 nm wavelength necessary for this calculation were obtained from the Center for X-Ray Optics [27]. The thickness of the silicon oxide layer was measured using ellipsometry to be 3.0(1) nm (described in Supplement 1, Appendix C), and the thickness of the titanium oxide layer was assumed to be 2.9 (2) nm based on the literature [28,29]. For the SiO_2/Si region, the phase change δ_{Si} was calculated to be −1.22(3) rad and the theoretical reflectivity was calculated to be 0.33%. For the TiO_2/Ti patterns, the phase change δ_{Ti} was calculated to be −1.92(9) rad and the theoretical reflectivity was calculated to be 10.9%. The difference in reflectivities for titanium versus silicon means that theoretically, the ratio of reflected field amplitudes (square root of intensity) should be 5.7, assuming no surface roughness. The object reconstruction shows a range for the ratio of the reflected amplitudes of 3.0–6.7, with a median ratio of 4.0. The measured ratio is based on a histogram of the reconstructed amplitude shown in Fig. 2(d) and is in reasonable agreement with the calculated reflectivities: it is not unexpected that the median is lower, since the theoretical reflectivity ratio assumed no surface roughness.

A polynomial subtraction was applied to the reconstructed phase of the silicon substrate, similar to that used in AFM image flattening [30]. We first excluded the titanium features from the image and then fit a polynomial function to the remaining phase values. This function was subtracted from the full image, resulting in constant values across the silicon substrate. The peak-to-valley height variation of the subtracted surface fit was <4 nm over the full 35 μm × 40 μm field of view. After flattening, the reconstruction shows an average of 4.26 rad of phase difference between the titanium and

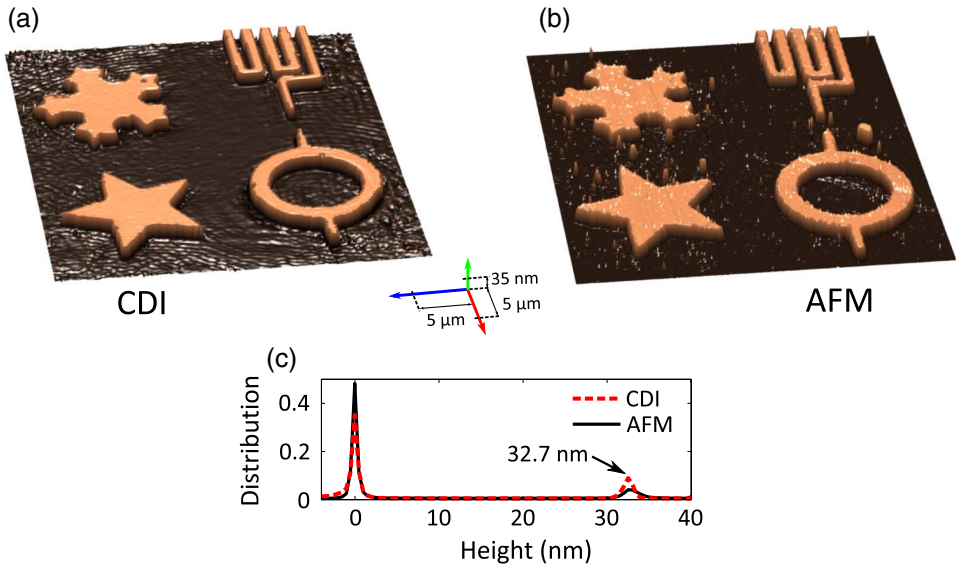

Fig. 3. Height profile comparison between CDI and AFM. (a) 3D profile of the object based on ptychographic reconstruction and (b) 3D profile of the object based on an AFM measurement. Any features taller than 40 nm were thresholded to 40 nm for the 3D rendering. (c) Histograms of the height profiles shown in (a) and (b). The histograms were used to calculate the average feature thickness of 32.7 nm based on the both the CDI and AFM measurements. The scale axis shown in (a) is shared by both (a) and (b). Note that the large debris spot on the right of the AFM image was introduced after the CDI image was taken.

silicon surfaces, corresponding to a 46.2(7) nm path length difference (when 2π is added and after taking the phase changes upon reflection into account). This corresponds to a 32.7(5) nm average thickness of the titanium patterns. A height map of the sample could then be produced by assuming that 2π should be added to any part of the reconstruction that exhibited an amplitude above 25% of the maximum (based on the relative reflectivities of titanium and silicon, as discussed above). Additionally, the reflection phases δ_{Si} and δ_{Ti} were subtracted from the Si and Ti regions using the same criteria. The result of this analysis is displayed in Fig. 3(a) and represents a significant improvement in image quality compared with all tabletop coherent reflective imaging to date. After the ptychography measurements were taken, an independent height map of the sample was obtained using a Digital Instruments Dimension 3100 AFM. The resulting AFM height map is shown in Fig. 3(b), after applying the same flattening method as that used for the CDI reconstruction. The AFM measurement shows an average height for the titanium features of 32.7 nm, which agrees exactly with the ptychography result within error bars.

Many small pieces of debris are visible in the AFM image shown in Fig. 3(b), with heights above that of the patterned titanium. None of the EUV work was done in a cleanroom environment. The reason these are not visible in the CDI height map [Fig. 3(a)] is that the 3D information relies on the phase difference of light reflecting from the substrate versus the features (at 45°) and not on the absolute height difference. While the debris locations are still evident in the CDI reconstruction [Fig. 2(d)], the modulo 2π ambiguity of the phase information combined with the very short wavelength prevents us from extracting the absolute height information of all features. However, a tomographic or multiwavelength approach would enable full 3D reconstructions of all features on a surface [31].

We find that for ptychographic grids of 3×3 and larger with sufficient overlap between adjacent probe positions (60%–70% area overlap [12]), the algorithm converges to a consistent result for the probe provided that the phase curvature of the starting guess differs by no more than 50% of the actual phase curvature. Even this condition is relaxed entirely in the case of isolated objects. To demonstrate this, we performed a separate ptychographic retrieval of the probe by scanning a 5 μm diameter pinhole across the beam near the focus. The probe that is retrieved using this method can be propagated to the sample plane for comparison to the probe found in the course of the sample reconstruction. We found very good agreement between the two probe reconstructions, independent of the accuracy of the starting guess for the probe. More details of this comparison can be found in Supplement 1, Appendix A.

4. CONCLUSIONS

We have demonstrated the first general tabletop full-field reflection-mode CDI microscope, capable of imaging extended nanosurfaces at arbitrary angles in a noncontact, nondestructive manner. This technique is directly scalable to shorter wavelengths and higher spatial and temporal resolution, as well as tomographic imaging of surfaces. By combining reflection-mode CDI with HHG sources in the kilo-electron-volt photon energy region, it will be possible to capture nanoscale surface dynamics with femtosecond temporal and nanometer spatial resolution. Moreover, full characterization of the curved wavefront of the illuminating HHG beam at the sample plane through ptychography opens up the possibility for reflection keyhole CDI [32,33]. This is significant for dynamic studies,

since in contrast to ptychography CDI, which requires overlapping diffraction patterns, keyhole CDI needs only one diffraction pattern and therefore requires no scanning of the sample.

FUNDING INFORMATION

Defense Advanced Research Projects Agency (DARPA) (DARPA-BAA-12-63); National Science Foundation (NSF) (COSI IGERT, ERC in EUV Science and Technology); National Security Science and Engineering Faculty Fellowship; Semiconductor Research Corporation (SRC) (2013-OJ-2443).

See Supplement 1 for supporting content.

REFERENCES

1. J. Miao, P. Charalambous, and J. Kirz, "Extending the methodology of x-ray crystallography to allow imaging of micrometre-sized noncrystalline specimens," Nature **400**, 342–344 (1999).
2. M. D. Seaberg, D. E. Adams, E. L. Townsend, D. A. Raymondson, W. F. Schlotter, Y. Liu, C. S. Menoni, L. Rong, C.-C. Chen, J. Miao, H. C. Kapteyn, and M. M. Murnane, "Ultrahigh 22 nm resolution coherent diffractive imaging using a desktop 13 nm high harmonic source," Opt. Express **19**, 22470–22479 (2011).
3. H. Jiang, C. Song, C.-C. Chen, R. Xu, K. S. Raines, B. P. Fahimian, C.-H. Lu, T.-K. Lee, A. Nakashima, J. Urano, T. Ishikawa, F. Tamanoi, and J. Miao, "Quantitative 3D imaging of whole, unstained cells by using x-ray diffraction microscopy," Proc. Natl. Acad. Sci. USA **107**, 11234–11239 (2010).
4. J. Nelson, X. Huang, J. Steinbrener, D. Shapiro, J. Kirz, S. Marchesini, A. M. Neiman, J. J. Turner, and C. Jacobsen, "High-resolution x-ray diffraction microscopy of specifically labeled yeast cells," Proc. Natl. Acad. Sci. USA **107**, 7235–7239 (2010).
5. J. N. Clark, L. Beitra, G. Xiong, A. Higginbotham, D. M. Fritz, H. T. Lemke, D. Zhu, M. Chollet, G. J. Williams, M. Messerschmidt, B. Abbey, R. J. Harder, A. M. Korsunsky, J. S. Wark, and I. K. Robinson, "Ultrafast three-dimensional imaging of lattice dynamics in individual gold nanocrystals," Science **341**, 56–59 (2013).
6. J. J. Turner, X. Huang, O. Krupin, K. A. Seu, D. Parks, S. Kevan, E. Lima, K. Kisslinger, I. McNulty, R. Gambino, S. Mangin, S. Roy, and P. Fischer, "X-ray diffraction microscopy of magnetic structures," Phys. Rev. Lett. **107**, 033904 (2011).
7. R. Xu, H. Jiang, C. Song, J. A. Rodriguez, Z. Huang, C.-C. Chen, D. Nam, J. Park, M. Gallagher-Jones, S. Kim, S. Kim, A. Suzuki, Y. Takayama, T. Oroguchi, Y. Takahashi, J. Fan, Y. Zou, T. Hatsui, Y. Inubushi, T. Kameshima, K. Yonekura, K. Tono, T. Togashi, T. Sato, M. Yamamoto, M. Nakasako, M. Yabashi, T. Ishikawa, and J. Miao, "Single-shot 3D structure determination of nanocrystals with femtosecond x-ray free electron laser pulses," arXiv:1310.8594 (2013).
8. T. Harada, M. Nakasuji, Y. Nagata, T. Watanabe, and H. Kinoshita, "Phase imaging of extreme-ultraviolet mask using coherent extreme-ultraviolet scatterometry microscope," Jpn. J. Appl. Phys. **52**, 06GB02 (2013).
9. S. Roy, D. Parks, K. A. Seu, R. Su, J. J. Turner, W. Chao, E. H. Anderson, S. Cabrini, and S. D. Kevan, "Lensless x-ray imaging in reflection geometry," Nat. Photonics **5**, 243–245 (2011).
10. M. Zürch, C. Kern, and C. Spielmann, "XUV coherent diffraction imaging in reflection geometry with low numerical aperture," Opt. Express **21**, 21131–21147 (2013).
11. T. Sun, Z. Jiang, J. Strzalka, L. Ocola, and J. Wang, "Three-dimensional coherent x-ray surface scattering imaging near total external reflection," Nat. Photonics **6**, 586–590 (2012).
12. A. M. Maiden and J. M. Rodenburg, "An improved ptychographical phase retrieval algorithm for diffractive imaging," Ultramicroscopy **109**, 1256–1262 (2009).
13. D. J. Vine, G. J. Williams, B. Abbey, M. A. Pfeifer, J. N. Clark, M. D. de Jonge, I. McNulty, A. G. Peele, and K. A. Nugent, "Ptychographic Fresnel coherent diffractive imaging," Phys. Rev. A **80**, 063823 (2009).
14. M. J. Humphry, B. Kraus, A. C. Hurst, A. M. Maiden, and J. M. Rodenburg, "Ptychographic electron microscopy using high-angle dark-field scattering for sub-nanometre resolution imaging," Nat. Commun. **3**, 730 (2012).
15. D. F. Gardner, B. Zhang, M. D. Seaberg, L. S. Martin, D. E. Adams, F. Salmassi, E. Gullikson, H. Kapteyn, and M. Murnane, "High numerical aperture reflection mode coherent diffraction microscopy using off-axis apertured illumination," Opt. Express **20**, 19050–19059 (2012).
16. D. Claus, D. J. Robinson, D. G. Chetwynd, Y. Shuo, W. T. Pike, J. J. De, J. T. Garcia, and J. M. Rodenburg, "Dual wavelength optical metrology using ptychography," J. Opt. **15**, 035702 (2013).
17. F. Zhang, I. Peterson, J. Vila-comamala, A. Diaz, R. Bean, B. Chen, A. Menzel, I. K. Robinson, and J. M. Rodenburg, "Translation position determination in ptychographic coherent diffraction imaging," Opt. Express **21**, 13592–13606 (2013).
18. T. Popmintchev, M.-C. Chen, D. Popmintchev, P. Arpin, S. Brown, S. Alisauskas, G. Andriukaitis, T. Balciunas, O. D. Mücke, A. Pugzlys, A. Baltuska, B. Shim, S. E. Schrauth, A. Gaeta, C. Hernández-García, L. Plaja, A. Becker, A. Jaron-Becker, M. M. Murnane, and H. C. Kapteyn, "Bright coherent ultrahigh harmonics in the keV x-ray regime from mid-infrared femtosecond lasers," Science **336**, 1287–1291 (2012).
19. D. Nardi, M. Travagliati, M. E. Siemens, Q. Li, M. M. Murnane, H. C. Kapteyn, G. Ferrini, F. Parmigiani, and F. Banfi, "Probing thermomechanics at the nanoscale: impulsively excited pseudosurface acoustic waves in hypersonic phononic crystals," Nano Lett. **11**, 4126–4133 (2011).
20. S. Mathias, C. La-o-vorakiat, J. M. Shaw, E. Turgut, P. Grychtol, R. Adam, D. Rudolf, H. T. Nembach, T. J. Silva, M. Aeschlimann, C. M. Schneider, H. C. Kapteyn, and M. M. Murnane, "Ultrafast element-specific magnetization dynamics of complex magnetic materials on a table-top," J. Electron Spectrosc. Relat. Phenom. **189**, 164–170 (2013).
21. P. Godard, G. Carbone, M. Allain, F. Mastropietro, G. Chen, L. Capello, A. Diaz, T. H. Metzger, J. Stangl, and V. Chamard, "Three-dimensional high-resolution quantitative microscopy of extended crystals," Nat. Commun. **2**, 568 (2011).
22. S. O. Hruszkewycz, M. V. Holt, C. E. Murray, J. Bruley, J. Holt, A. Tripathi, O. G. Shpyrko, I. McNulty, M. J. Highland, and P. H. Fuoss, "Quantitative nanoscale imaging of lattice distortions in epitaxial semiconductor heterostructures using nanofocused x-ray Bragg projection ptychography," Nano Lett. **12**, 5148–5154 (2012).
23. R. A. Bartels, A. Paul, H. Green, H. C. Kapteyn, M. M. Murnane, S. Backus, I. P. Christov, Y. Liu, D. Attwood, and C. Jacobsen, "Generation of spatially coherent light at extreme ultraviolet wavelengths," Science **297**, 376–378 (2002).
24. P. Thibault, M. Dierolf, O. Bunk, A. Menzel, and F. Pfeiffer, "Probe retrieval in ptychographic coherent diffractive imaging," Ultramicroscopy **109**, 338–343 (2009).
25. A. M. Maiden, M. J. Humphry, F. Zhang, and J. M. Rodenburg, "Superresolution imaging via ptychography," J. Opt. Soc. Am. A **28**, 604–612 (2011).
26. M. Born and E. Wolf, *Principles of Optics*, 7th ed. (Cambridge University, 1999).
27. B. L. Henke, E. M. Gullikson, and J. C. Davis, "X-ray interactions: photoabsorption, scattering, transmission, and reflection at E = 50–30,000 eV, Z = 1-92," At. Data Nucl. Data Tables **54**, 181–342 (1993).
28. T. Ohtsuka, M. Masuda, and N. Sato, "Ellipsometric study of anodic oxide films on titanium in hydrochloric acid, sulfuric acid, and phosphate solution," J. Electrochem. Soc. **132**, 787–792 (1985).

29. M. Advincula, X. Fan, J. Lemons, and R. Advincula, "Surface modification of surface sol-gel derived titanium oxide films by self-assembled monolayers (SAMs) and non-specific protein adsorption studies," Colloids Surf. B: Biointerfaces **42**, 29–43 (2005).
30. G. Haugstad, *Atomic Force Microscopy: Understanding Basic Modes and Advanced Applications* (Wiley, 2012).
31. D. J. Batey, D. Claus, and J. M. Rodenburg, "Information multiplexing in ptychography," Ultramicroscopy **138**, 13–21 (2014).
32. B. Abbey, K. A. Nugent, G. J. Williams, J. N. Clark, A. G. Peele, M. A. Pfeifer, M. de Jonge, and I. McNulty, "Keyhole coherent diffractive imaging," Nat. Phys. **4**, 394–398 (2008).
33. B. Zhang, M. D. Seaberg, D. E. Adams, D. F. Gardner, E. R. Shanblatt, J. M. Shaw, W. Chao, E. M. Gullikson, F. Salmassi, H. C. Kapteyn, and M. M. Murnane, "Full field tabletop EUV coherent diffractive imaging in a transmission geometry," Opt. Express **21**, 21970–21980 (2013).

Review Article Vol. 1, No. 1 / July 2014 / Optica 45

Third-generation femtosecond technology

Hanieh Fattahi,[1,2] Helena G. Barros,[2] Martin Gorjan,[1,2] Thomas Nubbemeyer,[2] Bidoor Alsaif,[1,3,4] Catherine Y. Teisset,[5] Marcel Schultze,[5] Stephan Prinz,[5] Matthias Haefner,[5] Moritz Ueffing,[2] Ayman Alismail,[2,3] Lénárd Vámos,[2,6] Alexander Schwarz,[1,2] Oleg Pronin,[2] Jonathan Brons,[2] Xiao Tao Geng,[1,7] Gunnar Arisholm,[8] Marcelo Ciappina,[1] Vladislav S. Yakovlev,[1,2,9] Dong-Eon Kim,[7] Abdallah M. Azzeer,[3] Nicholas Karpowicz,[1] Dirk Sutter,[10] Zsuzsanna Major,[1,2] Thomas Metzger,[5] and Ferenc Krausz[1,2,*]

[1]Max-Planck Institut für Quantenoptik, Hans-Kopfermann-Str. 1, D-85748 Garching, Germany

[2]Department für Physik, Ludwig-Maximilians-Universität München, Am Coulombwall 1, D-85748 Garching, Germany

[3]Physics and Astronomy Department, King Saud University, Riyadh 11451, Saudi Arabia

[4]Current address: Electrical Engineering, Computer, Electrical and Mathematical Sciences and Engineering Division, Building 1, 4700 King Abdullah University of Science and Technology, Thuwal 23955-6900, Saudi Arabia

[5]TRUMPF Scientific Lasers GmbH + Co. KG, Feringastr. 10, 85774 München-Unterföhring, Germany

[6]Wigner Research Center for Physics, Konkoly-Thege Miklós út 29-33, H-1121 Budapest, Hungary

[7]Physics Department, POSTECH, San 31 Hyoja-Dong, Namku, Pohang, Kyungbuk 790-784, South Korea

[8]FFI (Norwegian Defence Research Establishment), Postboks 25, NO-2027 Kjeller, Norway

[9]Current address: Center for Nano-Optics (CeNO), Georgia State University, Atlanta, Georgia 30303, USA

[10]TRUMPF Laser GmbH + Co. KG, Aichhalder Str. 39, 78713 Schramberg, Germany

*Corresponding author: krausz@lmu.de

Received 23 May 2014; revised 25 June 2014; accepted 26 June 2014 (Doc. ID 212665); published 22 July 2014

Femtosecond pulse generation was pioneered four decades ago using mode-locked dye lasers, which dominated the field for the following 20 years. Dye lasers were then replaced with titanium-doped sapphire (Ti:Sa) lasers, which have had their own two-decade reign. Broadband optical parametric amplifiers (OPAs) appeared on the horizon more than 20 years ago but have been lacking powerful, cost-effective picosecond pump sources for a long time. Diode-pumped ytterbium-doped solid-state lasers are about to change this state of affairs profoundly. They are able to deliver 1 ps scale pulses at kilowatt-scale average power levels, which, in thin-disk lasers, may come in combination with terawatt-scale peak powers. Broadband OPAs pumped by these sources hold promise for surpassing the performance of current femtosecond systems so dramatically as to justify referring to them as the next generation. Third-generation femtosecond technology (3FST) offers the potential for femtosecond light tunable over several octaves, multi-terawatt few-cycle pulses, and synthesized multi-octave light transients. Unique tunability, temporal confinement, and waveform variety in combination with unprecedented average powers will extend nonlinear optics and laser spectroscopy to previously inaccessible wavelength domains, ranging from the far IR to the x-ray regime. Here we review the underlying concepts, technologies, and proof-of-principle experiments. A conceptual design study of a prototypical tunable and wideband source demonstrates the potential of 3FST for pushing the frontiers of femtosecond and attosecond science. © 2014 Optical Society of America

OCIS codes: (140.0140) Lasers and laser optics; (140.3480) Lasers, diode-pumped; (190.4970) Parametric oscillators and amplifiers; (320.7160) Ultrafast technology; (140.3615) Lasers, ytterbium; (230.4480) Optical amplifiers.

http://dx.doi.org/10.1364/OPTICA.1.000045

2334-2536/14/010045-19$15/0$15.00 © 2014 Optical Society of America

1. INTRODUCTION

Femtosecond technology was born in the 1970s, when passively mode-locked dye lasers produced the first pulses shorter than 1 ps [1–3]. Subsequent advances led to pulse durations of a few tens of femtoseconds directly from laser oscillators [4–7]. The poor energy storage capability of laser dyes limited amplification to microjoule energies and megawatt peak powers [8,9]. This first-generation femtosecond technology (1FST) opened the door for direct time-domain investigations of hitherto immeasurably fast processes such as molecular dynamics, chemical reactions, and phase transitions in condensed matter [10,11].

Broadband solid-state lasers with large energy storage capabilities appeared by the end of the 1980s [12–14]. They offered the potential for further pulse shortening as well as boosting the pulse energy and peak power by many orders of magnitude. Second-generation femtosecond technology (2FST), based on chirped-pulse amplification (CPA) [15] in solid-state lasers, in particular, in Ti:sapphire-based systems [16–18], and dispersion control by chirped multilayer mirrors (henceforth, for brevity, chirped mirrors) [19–21] paved the way for the emergence of entirely new research fields and technologies such as attosecond science [22] and laser-driven particle acceleration [23].

2FST is now capable of providing pulses with ultrahigh (petawatt) peak power at moderate average power [24] and moderate-peak-power (gigawatt) pulses at ultrahigh (approaching the kilowatt scale) average power levels [25]; see Fig. 1. Based on optical parametric chirped-pulse amplification (OPCPA) [26] driven by terawatt-scale pulses from ytterbium lasers at kilowatt-scale average power, third-generation femtosecond technology (3FST) will, as a defining characteristic, *combine high (terawatt-scale) peak powers with high (kilowatt-scale) average powers* in ultrashort optical pulse generation for the first time. This unprecedented parameter combination will allow us to explore extreme nonlinearities of matter and extend ultrashort pulse generation to short (nanometer to subnanometer) as well as long (multimicrometer) wavelengths at unprecedented flux levels, holding promise for yet another revolution in ultrafast science. Figure 1 shows a summary of the performance of 1FST, 2FST, and 3FST systems.

OPCPA requires intense optical pulses for pumping the nonlinear medium used for the parametric conversion. The optimum duration of these pulses is of the order of 1 ps, constituting a trade-off between a high resistance to optical damage (decreasing for longer pulses [27–29]) and a small temporal walk-off [30,31] between pump and signal pulses relative to their duration (increasing for shorter pulses). OPCPA pumped by 1-ps-scale pulses offers octave-spanning light amplification with unprecedented efficiency, not accessible by any other technique known to date. Moreover, for very similar physical reasons, these pulse durations appear to be ideal for efficient frequency conversion of the pump light via low-order harmonic generation and/or frequency mixing [32,33]. Hence, a reliable, cost-effective, and power-scalable source of high-energy 1-ps-scale laser pulses would constitute the ideal basis

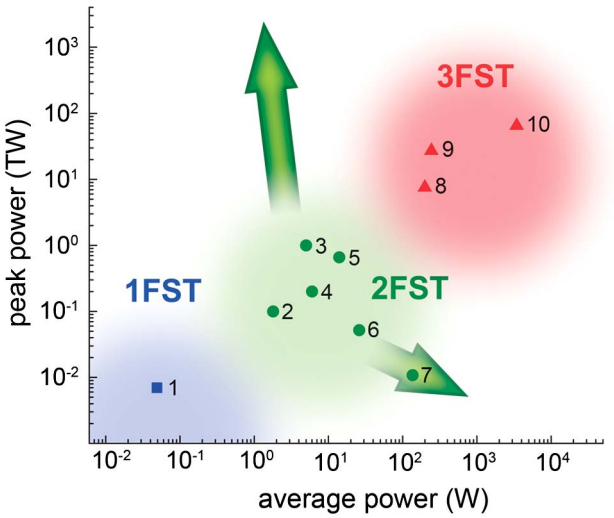

	τ_{pulse}	E_{pulse}	P_{peak}	$P_{average}$
system 8	5 fs	40 mJ	7.5 TW	200 W
system 9	1.7 fs	49 mJ	27 TW	245 W
system 10	5 fs	345 mJ	65 TW	3450 W

Fig. 1. Summary of recorded performances of 1FST and 2FST and the expected performance of 3FST, in terms of average and peak powers. These systems are reviewed in detail in Supplement 1. The blue square represents the best performance achieved by dye-laser technology (1, corresponding to Ref. [9]), the green dots show femtosecond CPA solid-state technology (2–7, corresponding to Refs. [60,71,66,18,67], and [25], respectively), and the red triangles represent the simulated results for OPCPA based on pump sources under development (8 and 9, pumped by a 1 ps, 5 kHz, 200 mJ Yb:YAG thin-disk laser) and envisioned (10, based on a future 1 ps, 10 kHz, 2 J Yb:YAG thin-disk laser system). Systems 8 and 10 use one OPCPA channel in the NIR, whereas in system 9 the output of three OPCPA channels in the VIS–NIR–IR are added for coherent synthesis of a subcycle waveform. The table summarizes the predicted output parameters of these systems. The relevant pump source architectures and multichannel OPCPA system are discussed in Section 2 and Section 3, respectively. OPCPA systems pumped by Yb:YAG slab and fiber amplifier systems [108,110] have been demonstrated in the performance range of 2FST and are not displayed in the figure.

for exploiting the full potential of OPCPA for ultrashort pulse amplification at a variety of wavelengths.

In this work we show that diode-pumped Yb-doped thin-disk lasers based on a technology well established in industrial environments fulfill all these requirements and offer a promising route to implementing 3FST in the conceptual architecture outlined in Fig. 2. In addition to simultaneously reaching peak and average power levels that will outperform 1FST and 2FST by several orders of magnitude (Fig. 1), 3FST systems allow a variety of operational modes, offering multicycle pulses tunable over several octaves, few-cycle pulses at different carrier wavelengths, and multi-octave synthesis of light waveforms.

Our discussion in this paper focuses on powerful ultrashort-pulse generation at high (≥1 kHz) repetition rates; ultrahigh-intensity lasers emitting a few pulses per second or less as well as sources delivering moderate-power pulses at high average power are out of the scope of this work (for a review, the

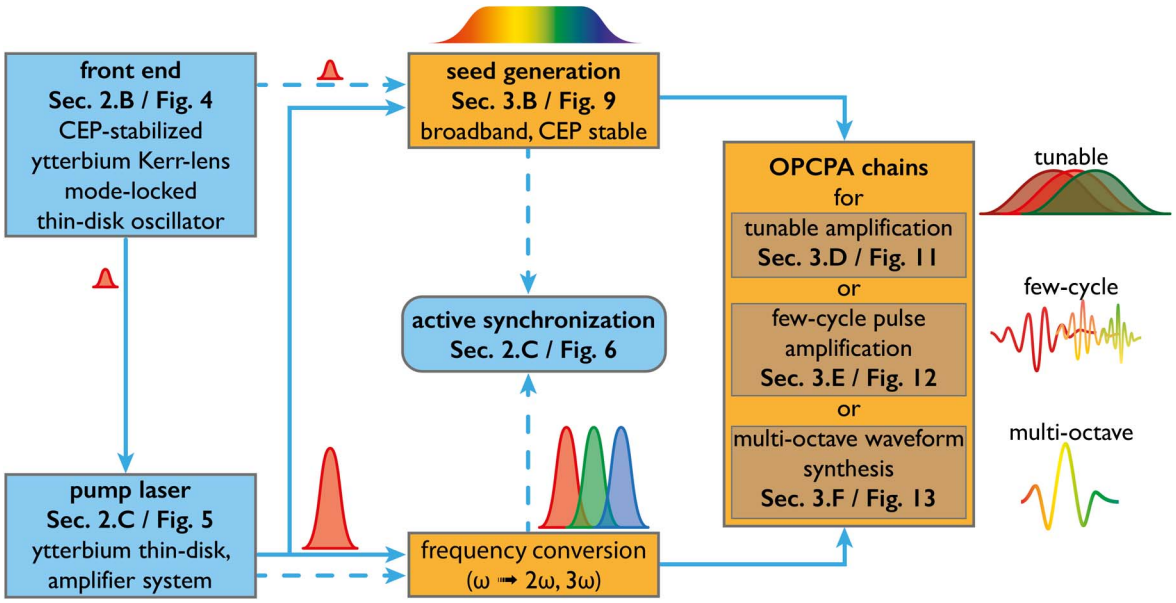

Fig. 2. Basic conceptual architecture of a 3FST system. A subpicosecond ytterbium laser oscillator seeds the pump source. The broadband seed can be generated either from the output of the picosecond pump laser (solid arrows) or directly from the oscillator (dashed arrows). In the latter case an active temporal synchronization is needed between the pump and seed pulses of the OPCPA chain. The 3FST source can be operated to generate (i) widely tunable pulses of a few tens of femtoseconds duration, (ii) few-cycle pulses in different spectral ranges, or (iii) multi-octave controlled waveforms with a sub-optical-cycle structure. The building blocks of the 3FST system are discussed in detail in the respective sections as indicated in the figure.

interested reader is kindly referred to relevant reviews in [23] and [34], respectively). A brief historical overview of 1FST [1–9,35–45] and 2FST [12–21,45–73] is presented in Supplement 1. The remaining part of the introduction addresses some of the major milestones of OPCPA history.

A. Conceptual Basis for 3FST

Optical parametric amplification (OPA) was discovered in the 1960s [74,75], but only nonlinear crystals with a high second-order nonlinear susceptibility and high resistance to optical damage, such as β-barium borate (BBO) [76] along with the invention of OPCPA by Piskarskas and co-workers [26] opened the prospect for efficient amplification of femtosecond laser pulses via this mechanism. A prerequisite for OPA being able to provide a competitive alternative to femtosecond laser amplifiers is the availability of power-scalable pump sources with a good wall-plug efficiency. So far, only lasers with pulse durations much longer than 1 ps have been able to meet this requirement. The instantaneous nature of the OPA pump-to-signal energy conversion calls for a signal pulse that is temporally stretched to match the duration of the pump pulse for efficient OPA and then recompressed after amplification.

The bandwidth of OPCPA can be enhanced by a noncollinear pump-signal beam propagation geometry, utilizing the slightly different propagation directions of the interacting beams to compensate the effect of material dispersion in the nonlinear medium [77,78]. Drawing on these basic concepts and a variety of pump and seed sources, a large number of OPA experiments aiming at efficient amplification of ultrashort pulses have been performed over the past 20 years. Their review is beyond the scope of this paper; we refer the interested reader to a number of excellent review articles on this subject [79–83].

OPCPA has been demonstrated to be capable of amplifying pulses as short as 4 fs [84], achieving peak-power levels of 16 TW from a tabletop system [85], approaching the petawatt frontier when pumped by large-scale lasers [86–92], and reaching average power levels as high as 22 W at a 1 MHz repetition rate [93]. However, none of these systems have been capable of achieving high peak and average powers simultaneously. The most powerful OPCPA system of this kind reported to date delivers 0.49 TW pulses at an average power of 2.7 W [94], which is still inferior to state-of-the-art Ti:Sa systems. The pump laser technology described in Section 2 holds promise for changing this state of affairs dramatically.

In what follows, Section 2 reviews near-1-ps pulse amplification and its implementation with thin-disk lasers, scalable to high peak as well as average powers. Section 3 is devoted to conceptual design studies demonstrating the potential of 3FST for creating a source of femtosecond light with unprecedented characteristics, and Section 4 addresses some of the expected implications.

2. NEAR-1-PS YTTERBIUM LASERS

Near-1-ps laser pulses with high peak power have long been available from flashlamp-pumped passively mode-locked neodymium-doped glass lasers—however, only at a very low repetition rate and hence low average power level [95–97]. High average powers ranging from tens to hundreds of watts recently became available from diode-pumped fiber, slab, and cryogenically cooled thick-disk lasers [98–109]. Because of excessive accumulation of nonlinearly induced phase shifts in their long gain media, their scaling to much higher energies requires large-aperture (meter-scale) and hence extremely

Table 1. Performance of Yb-Doped Few-Picosecond High Average and High Peak Power Systems[a]

P_{peak}	P_{avg}	E_{pulse}/τ_{pulse}	f_{rep}	Reference
		Fiber laser systems		
12 MW	830 W	10.6 μJ/640 fs	78 MHz	[100]
0.75 GW	93 W	93 μJ/81 fs	1 MHz	[102]
1.8 GW	530 W	1.3 mJ/670 fs	400 kHz	[106]
		Slab laser systems		
37 MW[b]	140 W	43 μJ/1.1 ps	3.25 MHz	[108]
80 MW	1.1 kW	55 μJ/615 fs	20 MHz	[99]
23 GW[b]	250 W	20 mJ/830 fs	12.5 kHz	[110]
		Cryogenically cooled laser systems		
0.65 MW[b]	430 W	8.6 μJ/12.4 ps	50 MHz	[104]
8.7 MW[b]	93 W	93 μJ/10 ps	1 MHz	[105]
73 MW	19.4 W	1 mJ/11.7 ps	20 kHz	[98]
7 GW[b]	60 W	12 mJ/1.6 ps	5 kHz	[103]
2 GW[b]	64 W	32 mJ/15 ps	2 kHz	[101]
170 GW	100 W	1 J/5.1 ps	100 Hz	[109]
		Thin-disk laser systems		
1.4 GW[b]	200 W	2 mJ/1.3 ps	100 kHz	[206]
17.6 GW[b]	300 W	30 mJ/1.6 ps	10 kHz	[147]
38.8 GW[b]	200 W	40 mJ/0.97 ps	5 kHz	Fig. 5(b)
27.6 GW[b]	100 W	50 mJ/1.7 ps	2 kHz	[134]
—	—	200 mJ	5 kHz	under development
—	—	2 J	10 kHz	envisioned

[a]Peak power (P_{peak}), average power (P_{avg}), pulse energy (E_{pulse}), pulse duration (τ_{pulse}), and repetition rate (f_{rep}) of selected Yb:YAG fiber, slab, cryogenically cooled, and thin-disk amplifier systems delivering pulses with a duration of a few picoseconds or shorter. The data are taken from the corresponding references.

[b]Peak powers have been calculated assuming a Gaussian pulse shape ($P_{peak} \approx 0.94 * E_{pulse}/\tau_{pulse}$).

expensive diffraction gratings for implementing CPA [102,106,110] or complex architectures, such as the coherent combination of a large number of parallel beams [111], or possibly coherent pulse stacking [112]. Diode-pumped ytterbium-doped thin-disk lasers offer energy and peak-power scalability from simple, cost-effective assemblies. Therefore, in what follows we focus on this technology as a promising candidate for driving broadband OPA systems scalable to high average and peak powers. Nevertheless, we stress that diode-pumped fiber, cryogenically cooled thick-disk, and slab lasers constitute a highly competitive alternative at high repetition rates and moderate peak power levels, and we kindly refer the reader to recent reviews of these approaches [33,107,113–116]. Table 1 summarizes the parameters of some of the best-performing systems based on Yb-doped fiber, slab, cryogenically cooled thick-disk, and thin-disk technology.

A. Toward High Peak and Average Powers

Ever since its first demonstration in 1994 [117], the thin-disk laser has been one of the most promising concepts for scaling sub-picosecond pulses to the highest peak and average powers. In this section we briefly summarize the basic features of thin-disk technology and refer the reader to Supplement 1 and recent reviews [118–120] for a more detailed discussion of performance, limitations and ways of overcoming them.

In a thin-disk laser the active medium is a thin and relatively large-diameter disk, typically tens to hundreds of micrometers in thickness and few (tens) millimeters in diameter. Crystals are used due to their favorable thermal and mechanical properties compared to glasses, with ytterbium-doped yttrium aluminium garnet (Yb:YAG) being the paradigm material of choice to date, although thin-disk lasers using different disk materials such as Yb:Lu_2O_3 [121,122], Yb:CALGO [123], and ceramic Yb:YAG disks [124,125] have also been demonstrated.

A Yb:YAG laser disk is coated on the back side to act as a high-reflective (HR) mirror for both the pump and the laser wavelengths. The other (front) side is antireflection (AR) coated for both wavelengths [see Fig. 3(a)]. The HR-coated side of the disk is firmly fixed onto a supporting substrate, which, in turn, is mounted on a water-cooled assembly. To achieve good (90% or more) absorption of the pump light, the pump beam is delivered at an angle from the front side and reflected in a number of passes using a special imaging multipass assembly [Fig. 3(b)]. Heat removal from the crystal is realized along the optical axis of the resonator. This minimizes thermally induced changes in the optical properties of the laser medium across the laser beam and allows for extremely high pump power densities reaching and exceeding 10 kW/cm^2 [118,126,127]. Energy and power scaling can be accomplished by scaling the diameter of the disk along with the pump and laser beams, which is eventually limited by amplified spontaneous emission (ASE) [128,129].

The small length of the gain medium greatly suppresses nonlinear focusing during the amplification of ultrashort pulses as compared to other laser geometries. As a result, CPA can be implemented with substantially smaller temporal stretching, requiring smaller, less expensive diffraction gratings as compared to other solid-state ultrashort pulse amplifiers [99,107]. These superior features of the thin-disk laser geometry come at the expense of a low single-pass gain of typically 10%–15% (small signal). This shortcoming can be mitigated by multiple passages and/or the serial combination of several disks [118,130,131].

Thin-disk gain modules have been used for ultrashort pulse generation in mode-locked oscillators [132,133] and regenerative [134] and multipass [135] amplifiers. Thousands of them have been tried and tested in 24/7 service for industry. This mature technology constitutes an ideal basis for scaling subpicosecond pulses to unprecedented combinations of peak

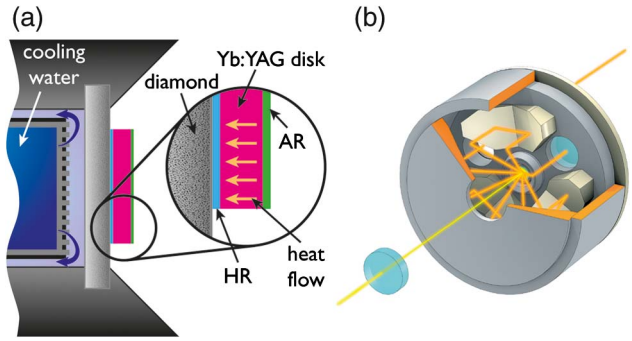

Fig. 3. Schematics of thin-disk laser technology. (a) Cold finger with substrate showing the cooling mechanism in a disk laser head, (b) disk laser head showing the principle of the pump light reimaging technique onto the thin-disk active medium (courtesy of TRUMPF Laser GmbH).

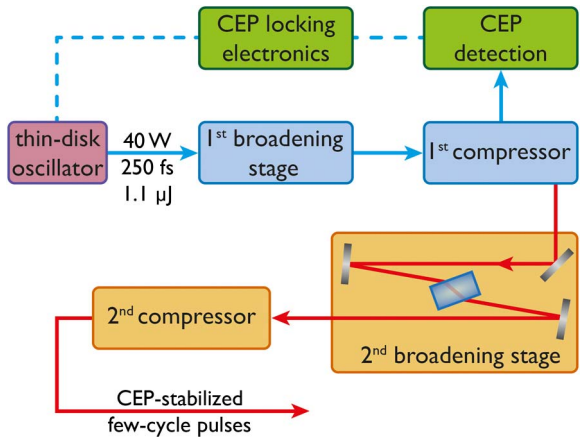

Fig. 4. Schematic of a KLM Yb:YAG laser system. Pulses from the oscillator centered at 1030 nm with an energy of 1.1 μJ and a duration of 250 fs at a repetition rate of 38 MHz are passed through a two-stage compressor made up of a solid-core large-mode-area fiber (first broadening stage), a bulk crystal as the nonlinear media (second broadening stage), and chirped mirrors forming the dispersive delay lines (first and second compressors), resulting in carrier-envelope-phase (CEP)-stabilized few-cycle output pulses [144].

and average power levels for driving OPAs in 3FST [136]. The remaining part of this section reveals how this technology can provide both the broadband seed and the high-power pump pulses in a perfectly synchronized fashion to this end.

B. Mode-Locked Ytterbium-Doped Thin-Disk Oscillators

Ultrashort pulse generation from a diode-pumped Yb-doped thin-disk laser oscillator was first demonstrated by Keller and co-workers at the turn of the millennium [137]. The technology was subsequently advanced to average power levels of hundreds of watts [138], pulse energies of several microjoules [130,139,140], and pulse durations shorter than 100 fs [131,141] directly from the oscillator. Kerr-lens mode locking (KLM) [49] and semiconductor saturable absorber mirrors [142] have been the methods of choice for mode locking [137,143].

Figure 4 shows the schematic of a KLM Yb:YAG thin-disk-oscillator-based few-cycle source [144]. The system delivers reproducible waveform-controlled few-cycle pulses at an average power exceeding that of few-cycle Ti:Sa oscillators by more than an order of magnitude.

The average power of KLM Yb:YAG thin-disk oscillators was recently increased by nearly an order of magnitude to deliver 14 μJ, 330 fs pulses at a 19 MHz repetition rate [140]. These advances open up the prospect of a megahertz source of near-infrared (NIR) femtosecond continua with a peak power of several hundred megawatts at average power levels of the order of 100 W and, if needed, with a controlled waveform. Such a source holds promise for greatly expanding the range of applications of ultrashort pulsed laser oscillators (as a stand-alone system) and for serving as a front end for gigawatt-to-terawatt 3FST architectures (see Fig. 2 and discussion in Section 3).

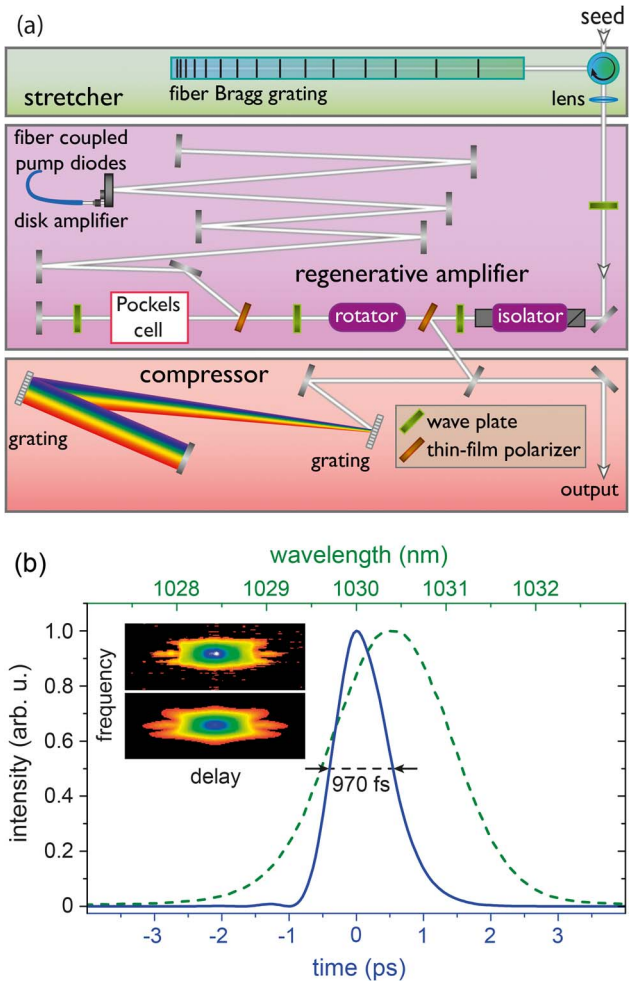

Fig. 5. Thin-disk regenerative amplifier. (a) Typical schematic layout. The subpicosecond seed pulse is temporally stretched before entering the thin-disk Yb:YAG regenerative amplifier. The amplified pulses are recompressed in a grating compressor. (b) Measured spectrum (green dashed line) and temporal intensity profile (blue line) from a system equipped with two disk modules (disk parameters: doping concentration >7%, thickness ~100 μm, beveled and roughened edge, TRUMPF Laser GmbH). These 0.97 ps pulses carry an energy of 40 mJ at a repetition rate of 5 kHz, corresponding to an average power of 200 W. The corresponding measured (top) and reconstructed (bottom) FROG traces are shown as insets (G error: 0.0024).

C. Thin-Disk Regenerative Amplifiers for Pumping OPCPA

The first thin-disk-based regenerative amplifier was demonstrated in 1997 and generated 2.3 ps pulses with energies up to 0.18 mJ and an average power of the order of 1 W [145]. A decade of development work advanced the technology into the multimillijoule, tens of watts regime [146]. By drawing on commercial Yb:YAG thin-disk modules originally designed for multikilowatt-class cw products, continued efforts led to near-1-ps pulses with energies as high as 30 mJ and average powers reaching 300 W at repetition rate of 10 kHz [147]. Milestones of this evolution are listed in Table 1, and a schematic of the architecture of state-of-the-art systems is shown in Fig. 5(a). All results on picosecond CPA with thin-disk lasers

referred to or reported directly in this work have so far been achieved with standard Yb:YAG thin-disk laser modules designed and fabricated for industrial lasers. This suggests that there may be some room left for further optimization of thin-disk Yb:YAG chirped-pulse amplifiers.

Thanks to their superior thermal management and low B integral, Yb:YAG thin-disk regenerative amplifiers deliver their near-bandwidth-limited pulses in a near-diffraction-limited beam ($M^2 < 1.1$) with excellent pulse-energy stability characterized by a drift smaller than 1% over 12 h. Figure 5(b) presents the measured optical spectrum and the retrieved temporal profile showing a full width at half-maximum (FWHM) pulse duration of 0.97 ps of an Yb:YAG thin-disk regenerative amplifier composed of two thin-disk amplifying modules within one resonator, delivering 40 mJ pulses at a repetition rate of 5 kHz.

While 40 mJ at 200 W and 30 mJ at 300 W [147] represent current records in high-energy 1-ps-scale pulse generation with high average power, none of these values individually appear to even come close to the ultimate limits of picosecond thin-disk laser technology. In fact, a regenerative amplifier followed by a multipass amplifier recently boosted the energy of sub-2-ps pulses to more than 500 mJ at a repetition rate of 100 Hz [148]. At a much higher repetition rate (800 kHz), 7 ps pulses from a commercial thin-disk laser were amplified to an average power of 1.1 kW [135]. An amplifier chain containing two thin-disk-based multipass amplifiers as final stages delivers 14 kW, 140 mJ in a 10 Hz burst mode [149].

Thanks to their optimum pulse duration of the order of 1 ps and excellent beam quality, thin-disk Yb:YAG regenerative amplifiers allow for efficient generation of second-harmonic and third-harmonic light by $\chi^{(2)}$ processes [second-harmonic generation (SHG) and sum-frequency generation (SFG), respectively]. As an example, results achieved with 1.3 ps, 1030 nm pulses from a multikilohertz Yb:YAG thin-disk laser demonstrate a second-harmonic conversion efficiency as high as 74% in a 1.5 mm thick LiB_3O_5 (LBO) crystal ($\theta = 90°$, $\varphi = 12.9°$).

OPA relies on a spatial as well as temporal overlap of the pump and seed pulses for efficient amplification. Hence, pump and seed pulses are derived from the same femtosecond laser [136,150] serving as the common front end. However, the pump pulse suffers a delay of several microseconds upon passage through the regenerative and/or multipass amplifier(s). This delay is compensated for by selecting a correspondingly delayed seed pulse from the train delivered by the common front end. Already fractional changes as small as 10^{-7} 10^{-8} (by air turbulences, mechanical vibrations, and expansion due to temperature drifts) in the microsecond delay of the pump and seed pulses suffered upon passage through different optical systems may cause an excessive timing jitter [151] and require active stabilization.

Spectrally resolved cross correlation of the seed and the pump pulses offers a powerful means of active synchronization [152]. A possible implementation of this concept is based on stretching a small fraction of the broadband seed pulse to a duration of several picoseconds and mixing this pulse with the narrowband pump pulse in a nonlinear crystal. Changes in the carrier wavelength of the resultant sum-frequency output are unambiguously related to the relative timing between pump and seed pulses. In its first demonstration, this stretched-pulse cross-correlation technique was capable of reducing the RMS timing jitter to $\sigma = 24$ fs over the frequency band of 20 mHz to 1.5 kHz [153].

Recently, this method was improved by replacing the sum-frequency generator by an OPA stage and deriving the timing information (optical error signal) from the spectrally resolved amplified signal output [154]. For this approach it is sufficient to split off only ~2 pJ of the seed pulse energy, since with the amplification of the seed pulse the OPA inherently delivers an amplified error signal. The concept is schematically depicted in Fig. 6(a). Its first implementation yielded pump–seed timing stabilization with a record residual RMS jitter of less than 2 fs over the frequency band ranging from 0.1 Hz to 1 kHz as well as long-term timing stability [Fig. 6(b)], ensuring ideal conditions for stable OPCPA operation.

D. Scaling Thin-Disk Amplifiers—Future Prospects

Present-day industrial thin-disk laser technology is capable of transforming diode-laser light of poor beam quality into kilowatts of power delivered in a diffraction-limited laser beam. The overriding question is to what extent this tremendous potential can be exploited for *simultaneously* boosting the energy *and* average power of near-1-ps laser pulses. Scaling of power and energy have already been demonstrated *separately*

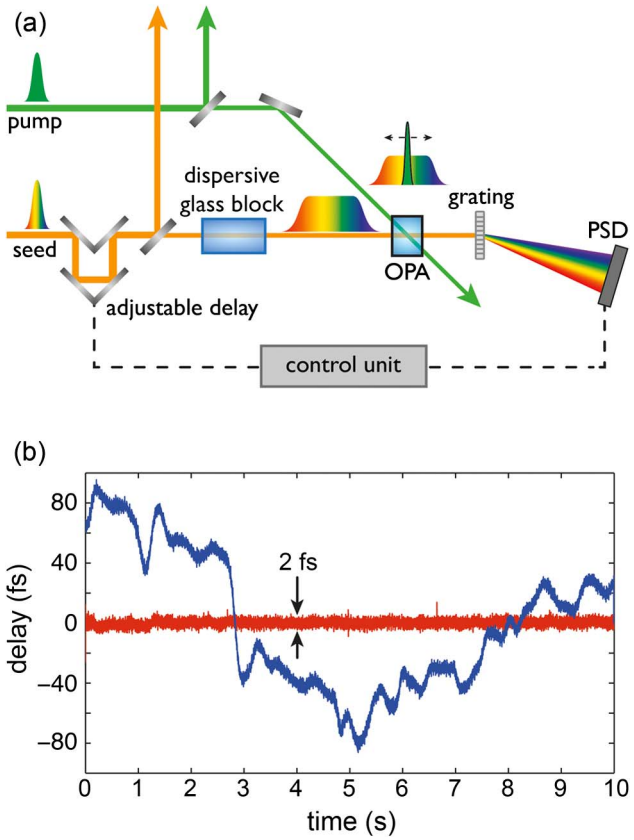

Fig. 6. Active pump-seed temporal synchronization system. (a) Schematic layout. PSD, position sensitive detector. (b) Timing fluctuations on the order of ±100 fs are reduced to a residual RMS jitter of less than 1.9 fs; for details, see [154].

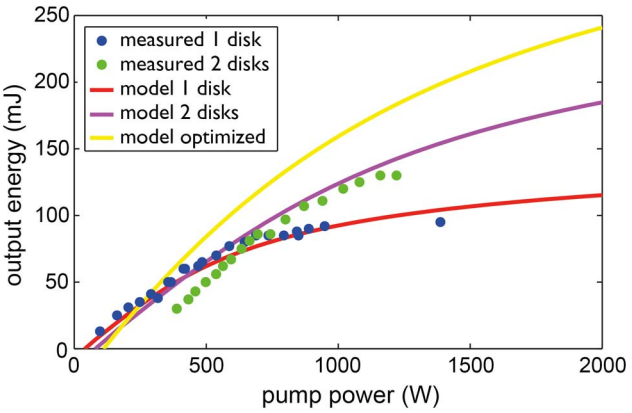

Fig. 7. Performance of cw diode-pumped regenerative amplifiers utilizing commercial thin-disk modules (disk parameters: doping concentration >9%, thickness ~120 μm, beveled and roughened edge, TRUMPF Laser GmbH). In a linear cavity setup, 95 mJ output energy was demonstrated at a 1 kHz repetition rate with one standard disk pumped at 940 nm (blue dots). While there were indications of energy saturation, the energy was boosted to 130 mJ by adding a second disk (green dots). By further optimization of both disk parameters and the pump design, more than 200 mJ energy at 5 kHz can be achieved (yellow line).

beyond 1 kW [135] and up to 1 J [155–157], respectively. Achieving these values of both energy and average power in the same thin-disk laser system will require optimal scaling of the disk diameter (increasing the available energy but also the depopulation losses) and disk thickness (increasing the available energy and the deleterious thermal effects) [118].

A regenerative amplifier equipped with commercial Yb:YAG thin-disk modules is being developed in our laboratory for generating 200 mJ pulses at a 5 kHz repetition rate. In preliminary experiments with a linear cavity amplifier, 95 and 130 mJ pulses at a repetition rate of 1 kHz have been demonstrated, with one and two disk modules, respectively (Fig. 7), with the latter being limited by thermal effects in the Faraday isolator preventing feedback into the front end [158]. The use of a ring cavity will remove this limitation and—based on these preliminary results—holds promise for achieving the above target parameters. A rate-equation model of thin-disk laser energy that takes into account the decrease in the upper level lifetime, caused by ASE [120] and the disk temperature, shows good agreement with the measurements and indicates that the same energy can be extracted up to 5 kHz with the current disks. An optimized design with increased disk thickness pumped at 969 nm can further increase the extracted energy, using the same beam size of 5 mm.

Much higher energies and powers can be expected from larger apertures [159]. The feasibility of scaling near-1-ps thin-disk amplifiers to the 1 J frontier was recently demonstrated [155–157]. Further discussion on how careful engineering of large-aperture Yb:YAG disk amplifier modules for minimizing ASE and temperature control could permit scaling of the amplified energy to the joule-kilowatt level is given in Supplement 1.

Such large-aperture Yb:YAG disks have been shown to be capable of handling more than 10 kW of diode laser power [160]. Merely a couple of thin-disk amplifier modules equipped with 20-mm-diameter Yb:YAG disks and pumped by approximately 30 kW of cw diode laser light each will be sufficient to boost the energy of the 0.2 J seed pulses—delivered by two 5 kHz regenerative amplifiers in a parallel architecture—to the level of 2 J at a 10 kHz repetition rate. A possible approach to this goal is schematically illustrated in Fig. 8. Should scaling to this energy level encounter unexpected difficulties, coherent combination of several amplifiers [25,161–163] or the concept of pulse stacking [112] might provide a remedy. These developments may open the door for a kilowatt-class 3FST source of few-cycle or tunable multiterawatt femtosecond pulses.

3. BROADBAND OPCPA PUMPED BY NEAR-1-PS PULSES

With robust nonlinear crystals and a reliable, cost-effective, and power-scalable short-pulsed pump-laser technology along with methods for accurate pump-seed timing synchronization in place (see Section 2.C), near-1-ps-pulse-pumped OPCPA offers several advantages over *both* long-pulse-driven OPCPA *and* conventional CPA implemented in solid-state laser amplifiers. First, the amplifier crystals can be pumped at much higher intensities [27–29], allowing high gains to be realized with very thin crystals, i.e., in combination with broad amplification bandwidths. Second, the short pump window also greatly simplifies the implementation of CPA and dispersion control and, finally and most importantly, improves the temporal contrast of the amplified signal dramatically on the nanosecond to few-picosecond time scale.

The gain bandwidth can be even further extended, up to several octaves, by using different crystals or crystals with different orientations yielding shifted gain bands and utilizing multiple pump beams [164] at all wavelengths where they can be made available with good wall-plug efficiency, i.e., at 1030 nm and its low-order harmonics at 515 and 343 nm. This constitutes the basis for developing the prototypical broadband or broadly tunable sources of 3FST. The very same front end and multicolor pump source may be utilized for both purposes. In what follows, we shall discuss the feasibility of these 3FST sources and their expected performance when being pumped with several-kilohertz, kilowatt-class thin-disk lasers recently demonstrated [147] and systems that are currently under development [158].

A. Basic Theory

In the OPA process, energy is transferred from a high-frequency, high-intensity (pump) beam to a low-frequency, low-intensity (seed or signal) beam in a birefringent [165] nonlinear crystal, while a third beam, the idler, is generated. By polarizing the pump along the fast axis and the signal or idler or both along the slow axis, conservation of energy and momentum of the participating (pump, signal, idler, labeled with p, s, and i, respectively) photons can be simultaneously fulfilled:

$$\hbar\omega_p - \hbar\omega_s - \hbar\omega_i = 0, \quad (1)$$

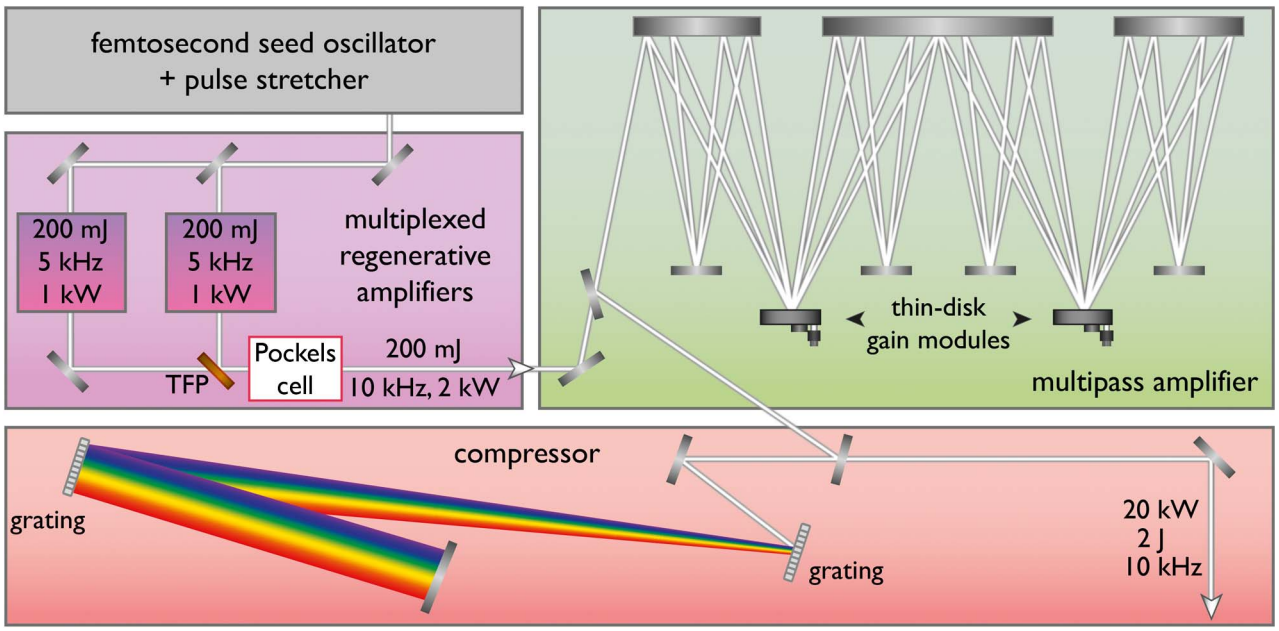

Fig. 8. Schematic layout of the multikilowatt, joule-class picosecond laser setup. A regenerative amplifier and a subsequent multipass amplification stage are used for generating multikilowatt, joule-class picosecond pulses (TFP, thin-film polarizer). Pulses from a front end comprising an oscillator and a pulse stretcher (cf. Fig. 5) are used to seed two regenerative amplifiers working at a 5 kHz repetition rate. The 200 mJ amplified pulses from both amplifiers are interleaved in time to produce a 10 kHz, 200 mJ pulse train. These pulses are then guided to a multipass amplifier using two thin-disk laser heads. Finally, the amplified pulses are compressed in a grating compressor.

$$\vec{k}_p - \vec{k}_s - \vec{k}_i = 0. \tag{2}$$

In the classical description of the process, Eqs. (1) and (2) account for the parametric frequency downconversion and phase (velocity) matching of the participating waves, respectively. Due to dispersion, these conditions can be fulfilled over a limited range of signal frequencies only, which manifests itself in a finite parametric gain bandwidth $\Delta\nu$ [166,167]:

$$\Delta\nu = \frac{2(\ln 2)^{1/2}}{\pi}\left(\frac{\Gamma}{L}\right)^{1/2}\left|\frac{1}{v_{gi}} - \frac{1}{v_{gs}}\right|^{-1}, \tag{3}$$

where L is the length of the nonlinear medium, Γ is the parametric gain coefficient proportional to the pump-field amplitude and the effective nonlinear optical coefficient, and $\nu_{gi,s}$ stand for the group velocity of the idler and the signal, respectively [166]. Equation (3) suggests that temporal walk-off between the amplified pulses limits the achievable gain bandwidth.

In sharp contrast with lasers, the central frequency and the width of the OPA gain band can be manipulated by changing the orientation or temperature of the crystal, and/or by the pump-signal propagation geometry. These degrees of freedom can be used to produce tunable femtosecond pulses. Alternatively, degenerate OPA near the wavelength where the group-velocity dispersion for the signal and idler beams becomes zero ($\omega_s \simeq \omega_i \simeq \omega_p/2$) [167] or the noncollinear OPA [77,78,168–170] permits the amplification of few-cycle pulses [171,172]. Both modes of operation can be simultaneously implemented in several OPA channels driven by the third or second harmonic or the fundamental of the 1030 nm picosecond pulses from Yb:YAG thin-disk amplifiers to yield synchronized tunable or few-cycle pulses in the visible (VIS), NIR, and mid-infrared (MIR) spectral ranges, respectively. These pulses may also be superimposed on each other for the synthesis of multi-octave light transients [173–175]. These options call for a seed coming in the form of a coherent, phase-stable, multi-octave supercontinuum covering the entire wavelength range of interest.

B. Generation of Waveform-Controlled Continua for OPA Seeding

The NIR continuum produced by the prototypical carrier-envelope-phase (CEP)-stabilized femtosecond KLM thin-disk-laser-based source described in Section 2.B [144], constitutes—after proper active synchronization to the pump pulses (see Section 2.C)—an ideal seed for broadband OPA. In fact, these CEP-stabilized continua exhibit a well-behaved spectral phase and excellent spatial beam quality and are delivered with microjoule-scale energy, allowing efficient OPA with low fluorescence background. The spectrum is perfectly matched to the gain band of BBO and LBO parametric amplifiers [136] pumped by the second harmonic of the Yb:YAG laser (515 nm).

Amplification in such an OPA to the millijoule energy level and recompression of the amplified NIR pulse may be followed by further spectral broadening in a gas-filled hollow-core fiber (HCF). Self-phase modulation and self-steepening broadens the input spectrum predominantly toward shorter

wavelengths. This approach can provide the broadband seed required by a VIS-OPCPA pumped by the third harmonic of the Yb:YAG laser (343 nm) but fails to do so for a MIR-OPCPA driven directly at 1030 nm. In the remaining part of this section we discuss the generation of a phase-stable continuum in the MIR and its subsequent extension to shorter wavelengths.

A powerful technique for the generation of CEP-stabilized MIR continua has been difference frequency generation (DFG) [176,177]. This process creates a CEP-stable output from a non-CEP-stabilized femtosecond pulse and has been successfully applied to seeding few-cycle MIR-OPA systems [166,178,179]. The output of the sub-10-fs NIR source described in Section 2.B can—after preamplification in a single broadband OPA stage pumped at 1030 nm—efficiently drive DFG to yield a continuum in the 1.5–2.5 μm range [180]. The oscillator does not need to be CEP stabilized, since the CEP of the fundamental cancels out in the DFG process.

The spectrum of the DFG output can be efficiently extended in a gas-filled HCF [181] to cover the multi-octave range of 400–2500 nm. The main building blocks of such a supercontinuum generator are sketched in Fig. 9(a). The 10-fs-scale seed pulses may possibly also be derived directly from the output of the near-1-ps Yb:YAG pump source by cascaded temporal compression [182], as indicated by a dashed line in Fig. 9(a). This approach would greatly relax the need for the active pump-seed synchronization system for the OPCPA described in Section 2.C, because both the pump and the seed would travel comparable optical paths.

All essential processes underlying the above concept have already been successfully demonstrated. In fact, we have recently generated IR continua [shown in Fig. 9(b)] from few-cycle NIR pulses with an efficiency exceeding 10% [180]. Moreover, the spectrum from a MIR-OPA seeded by a similar CEP-stable continuum could be efficiently broadened in a gas-filled HCF to cover the entire VIS-NIR-MIR spectral range of 400–2500 nm, which is also shown in Fig. 9(b). The temporal characterization of the continuum by second-harmonic frequency-resolved optical gating (FROG) shows the high degree of coherence and compressibility of the generated multi-octave spectrum in Fig. 9(b) [183]. This indicates such continua, at energy levels of hundreds of microjoules, are achievable with few-cycle MIR pulses, in agreement with theoretical predictions [181]. The seed signals for the simulated OPCPA systems discussed below are derived from the multi-octave continuum shown in Fig. 9(b).

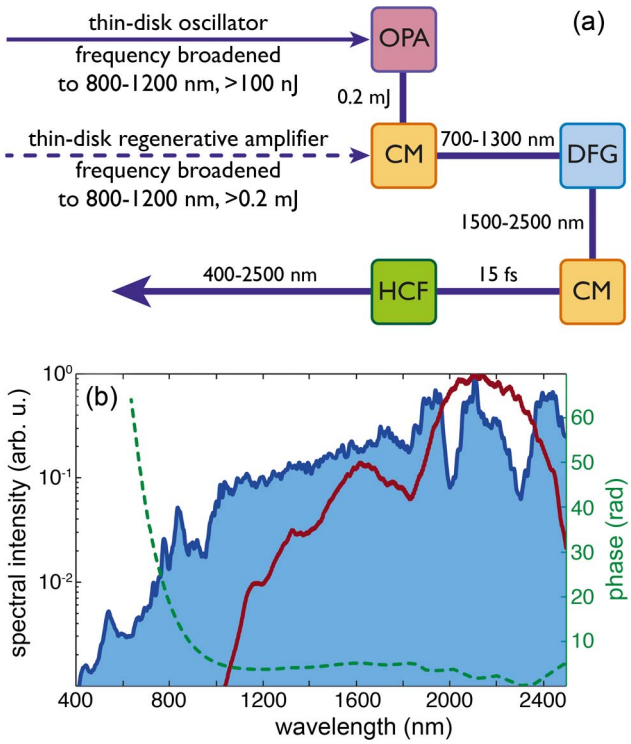

Fig. 9. Multi-octave seed generation. (a) Near-three-octave seed generation schemes based on the output from the oscillator described in Section 2.B or driven by the amplified subpicosecond pulse characterized in Fig. 5(b) (dashed arrow). The spectrally broadened and compressed output of the Yb:YAG oscillator is amplified in an OPA stage to 50 μJ of energy and subsequently compressed in a chirped-mirror compressor (CM) to about 6 fs for efficient difference frequency generation (DFG). The resultant broadband DFG signal, centered at about 2 μm, is compressed and focused into a gas-filled hollow-core fiber to extend the spectrum into the visible range. This approach provides a near-three-octave, phase-stable continuum at the energy level of the order of 1 μJ. Alternatively, spectrally broadened subpicosecond millijoule-scale pulses directly from the amplifier circumvent the need for an additional OPA stage and may result in a phase-stable supercontinuum at the level of several hundred microjoules. (b) Broadband phase-stable continua generated in preliminary experiments. Red curve: Difference-frequency radiation in a 500-μm-thick type-I BBO crystal optimized for 12% conversion efficiency. Blue shaded area: Spectral broadening of a parametrically amplified three-cycle DFG signal in a gas-filled hollow-core fiber to a supercontinuum containing 330 μJ of energy. The detected bandwidth of the spectrum in both cases is limited by the sensitivity of the spectrometer in the IR tail. The dashed green curve shows the measured spectral phase of the generated supercontinuum using the FROG technique. The red curve in (b) is reproduced from [180].

C. Prototypical OPCPA Architectures in 3FST

The common backbone for all prototypical 3FST architectures we propose and numerically analyze in the following sections consists of (i) a high-power femtosecond laser, in our case a 100-W-scale KLM Yb:YAG thin-disk oscillator, followed by (ii) the multi-octave seed generation described in the previous section and (iii) a multi-100-W-to-kW-scale source of multi-mJ, near-1-ps-pulses, in our case based on Yb:YAG thin-disk amplifiers, see Fig. 10(a). The supercontinuum seed [see Fig. 10(a)] is split into three spectral channels: VIS centered at 550 nm, NIR centered at 1 μm, and MIR centered at 2 μm, by using chirped dichroic beam splitters [173,184,185].

Each of the three OPA channels can be used to generate tunable multi-cycle pulses which will be described in Section 3.D or to yield few-cycle pulses as will be shown in Section 3.E. Their pump pulses are generated by a simple frequency-converter module comprising two LBO crystals. Our crystal of choice is LBO instead of BBO, owing to its availability in large sizes and its small spatial and temporal

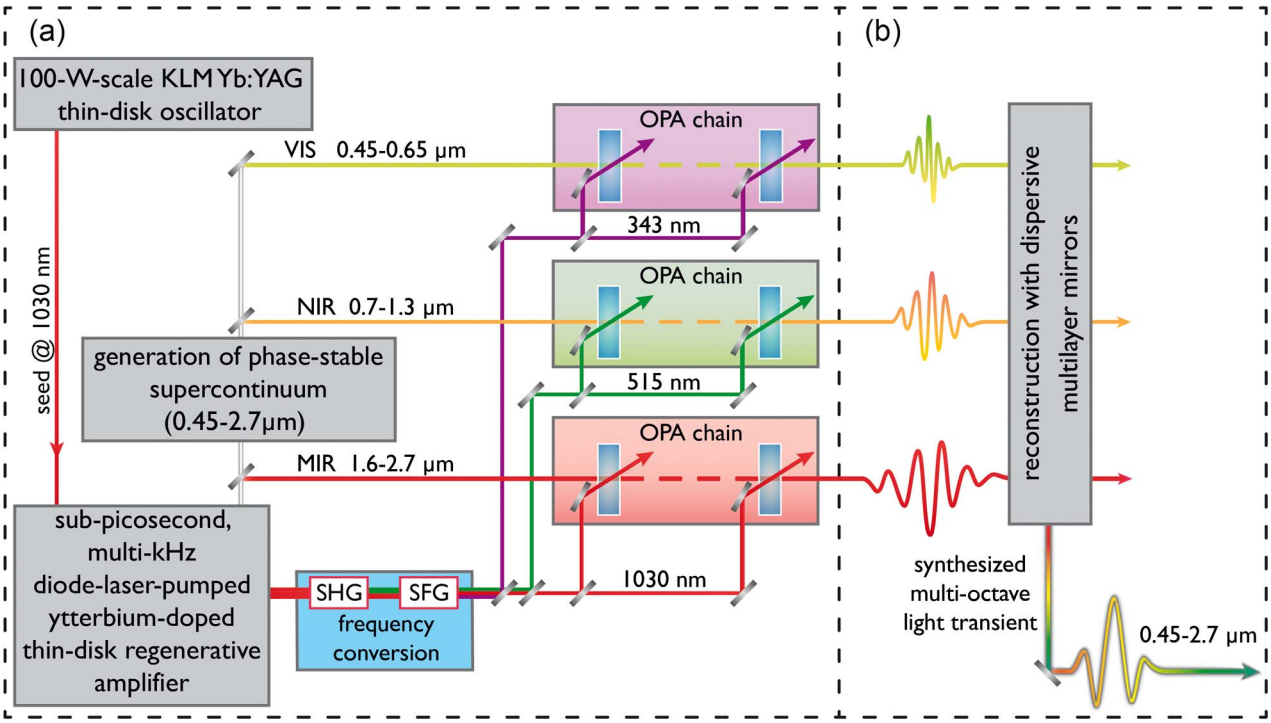

Fig. 10. Prototypical multi-octave 3FST field synthesizer (Section 3.E and Section 3.F). (a) Schematic architecture of a three-channel OPCPA system seeded and pumped by subpicosecond ytterbium lasers. A part of its output is used for generating the multi-octave supercontinuum signal, which is split into three channels, centered at 550 nm and 1 and 2 μm, respectively. The different channels are pumped by different (low-order) harmonics of the multimillijoule-level, kilohertz Yb:YAG regenerative amplifier output. Each channel supports few-cycle pulses after compression. Alternatively, using a similar concept, several-tens-of-femtoseconds multicycle pulses widely tunable from the UV to the IR spectral range can be produced. (b) By coherently combining the three few-cycle channels amplified in (a), nonsinusoidal multi-octave light transients can be generated.

walk-off, in spite of its smaller effective nonlinear coefficient. Second-harmonic generation (SHG) in the first one yields twin pulses of comparable energy at 515 nm and 1030 nm, which are mixed in the second crystal to produce a third pump pulse at 343 nm by sum-frequency generation (SFG). Moderate SHG and SFG conversion efficiencies (of about 50% and 20%–30%, respectively) ensure that all beams exiting the frequency converter unit have a good beam quality, which is important for OPCPA pumping. The three beams are subsequently separated by dichroic beam splitters and directed into the three OPA channels described in the following sections.

D. Power of 3FST: Tunability over Several Octaves

Time-resolved spectroscopy often requires tunable multicycle femtosecond pulses. The three OPCPA channels depicted in Fig. 10(a) can be designed to deliver wavelength-tunable femtosecond pulses. Their seed can be generated as described in the preceding section. We propose to produce the primary pump pulses at 1030 nm with the Yb:YAG thin-disk regenerative amplifier recently demonstrated, yielding 30 mJ, 1.6 ps pulses at a 10 kHz repetition rate, i.e., an average power level of 300 W [147]. The frequency converter described in the previous section distributes this pump energy among the three OPCPA channels. The super-continuum is divided into three bands centered at carrier wavelengths of 550 nm and 1 and 2 μm. They are seeded into the VIS, NIR, and MIR arms of the OPCPA system, each of which consists of two amplifier stages, using thin BBO, LBO, and $LiNbO_3$ crystals, pumped at 343, 515, and 1030 nm, respectively. For more details, see Supplement 1.

Pulse duration control and wavelength tuning of the amplified pulses is accomplished by temporally stretching the seed continua and controlling their delay with respect to the pump pulses. In fact, the pump temporal window of $\tau_{\text{pump}} \simeq 1$ ps slices out a fraction, $\Delta\nu_{\text{signal}}$, of the bandwidth of the (stretched) seed continuum, $\Delta\nu_{\text{seed}}$, which is inversely proportional to the duration τ_{seed} of the stretched seed: $\Delta\nu_{\text{signal}} \approx \Delta\nu_{\text{seed}}(\tau_{\text{pump}}/\tau_{\text{seed}})$ [see Fig. 11(a)]. Thanks to a near-linear chirp carried by the stretched seed, the carrier frequency of the amplified signal can be tuned by varying the delay of the seed with respect to the pump pulse and by setting the phase-matching angle of the amplifier crystal. Figure 11(b) shows a series of amplified signal spectra from simulations in the three channels pumped with pulses of a duration of $\tau_{\text{pump}} \simeq 1.7$ ps. The continua stretched to $\tau_{\text{seed}} \simeq 30$ ps yield—after recompression—sub-40-fs pulses tunable over several octaves from the VIS to the MIR spectral range. Synchronized femtosecond pulses with adjustable pulse duration and tunable carrier frequency at such a variety of wavelengths and unprecedented average power levels may open new prospects for sophisticated multidimensional spectroscopies and pump-control-probe schemes.

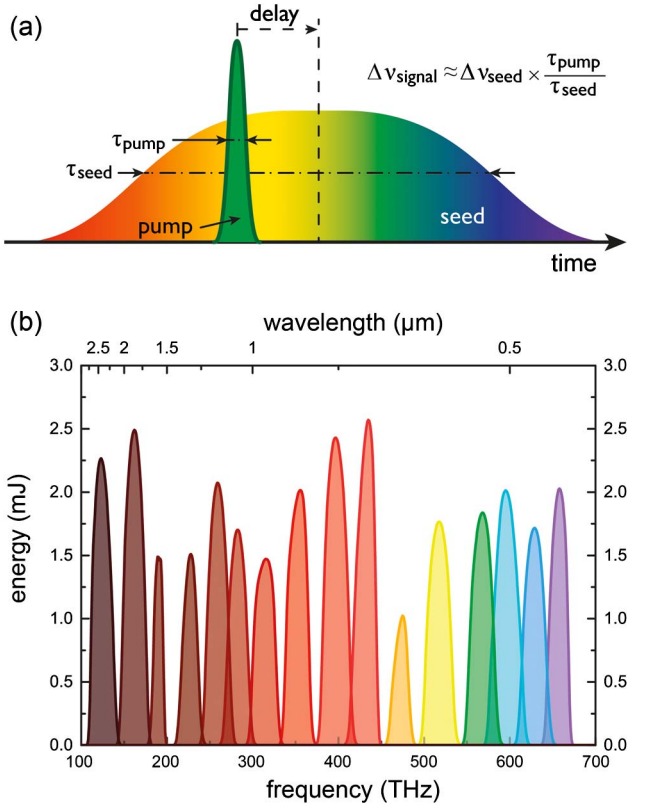

Fig. 11. Generation of widely tunable femtosecond pulses (Section 3.D). (a) Scheme for generating spectrally and temporally tunable pulses at any wavelength. The seed pulses are stretched to a significantly longer duration than that of the pump pulse. Amplification in a simple OPCPA setup yields pulses that can be spectrally tuned by changing the temporal delay between pump and seed pulses. (b) Amplified spectra of a widely tunable two-stage OPCPA system obtained from simulations. Millijoule-level, sub-40-fs pulses, tunable from 445 to 2750 nm, can be generated by using different harmonics of a 10 kHz Yb:YAG regenerative amplifier (see Supplement 1).

E. Power of 3FST: Multiterawatt VIS, NIR, and MIR Few-Cycle Waveforms

As an alternative to delivering tunable multicycle pulses, the three OPCPA channels of our prototypical 3FST system can be designed to generate few-cycle pulses at a single carrier wavelength from each channel, by broadband amplification and subsequent recompression of the continua seeded into the amplifier chains. Typical application fields of few-cycle pulses are attosecond science and extreme nonlinear optics, benefiting from peak powers as high as possible. Few-cycle pulses with multiterawatt peak powers are expected to allow scaling of the flux and/or the photon energy of attosecond pulses by increasing the beam size in high-harmonic generation (HHG) from ionizing atoms [22] or exploiting relativistic interactions with high-density plasmas at the surfaces of solids [186–191]. Therefore, we perform the following model calculations for a prototypical multicolor, multiterawatt few-cycle 3FST system by assuming the availability of the most powerful 3FST driver currently under development: a near-1-ps, 200 mJ, 5 kHz Yb:YAG thin-disk regenerative amplifier [158].

In our numerical study, we distribute the pump energy among the three OPA chains in favor of the NIR and MIR channels. This strategy is motivated by numerous applications benefiting from longer wavelengths [192–194]. Frequency conversion to the low-order harmonics as described in Section 3.C yields approximately 40 mJ at 343 nm, 74 mJ at 515 nm, and 86 mJ at 1030 nm for pumping the VIS, NIR, and MIR channels of the OPCPA system, respectively.

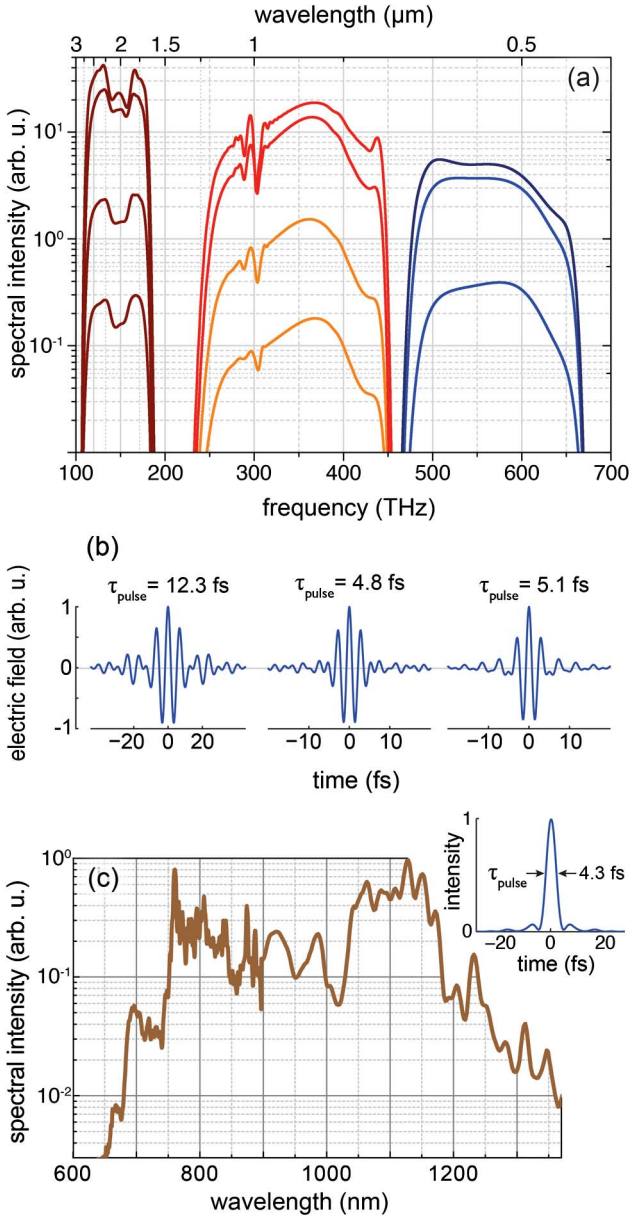

Fig. 12. Multi-octave amplified spectra of the three-channel synthesizer and corresponding waveforms (Section 3.E). (a) Spectra of the three-channel OPCPA synthesizer obtained from simulations. The spectra of the different stages in the different channels are normalized to their energy and shown on a logarithmic scale: VIS, blue; NIR, red-orange; IR, brown. For details of the simulations, see Supplement 1. (b) Fourier-transform-limited electric field associated with the output spectrum of each channel in (a); (c) amplified spectrum in a three-stage OPCPA chain. The spectrum contains 1.8 mJ and supports sub-5-fs pulses at a 3 kHz repetition rate.

The high intensity threshold for damage offered by the near-1-ps pump pulses allows a high single-pass gain in very thin (few-millimeter) OPA crystals, yielding a broad amplification bandwidth. The short length of the crystals is optimized for best gain saturation in each amplification stage. The energy is then boosted by using several amplification stages *without compromising the bandwidth.*

For the MIR channel using four $LiNbO_3$ crystals, our simulations predict an amplified pulse energy of 19.2 mJ, carried at a center wavelength of 2 μm, with a bandwidth-limited pulse duration of 12.3 fs (FWHM), corresponding to less than two cycles of the carrier wave. The pump-to-signal energy conversion efficiency in this channel is 22%, limited by back-conversion of the signal and idler into the pump via phase-matched SFG. In the NIR channel, 22.7 mJ pulses with a bandwidth-limited pulse duration of 4.8 fs can be expected (see Fig. 12), corresponding to a conversion efficiency of 30%. Thanks to the noncollinear geometry, parasitic back-conversion is strongly reduced, giving rise to an excellent efficiency. Last but not least, the VIS channel may yield 7.1 mJ pulses with a bandwidth-limited duration of 5.1 fs (Fig. 12). For details of the simulations, see Supplement 1.

In order to verify the credibility of this design study, we constructed a three-stage OPCPA test, seeded by a continuum derived from a Ti:sapphire front end (Femtopower Compact Pro Ti:sapphire multipass amplifier, Femtolasers GmbH) and pumped by an optically synchronized Yb:YAG thin-disk regenerative amplifier [136]. The 3 μJ seed pulse covering the spectral range of 500–1400 nm was generated in two stages of spectral broadening in a 120-μm-inner-diameter, 15-cm-long HCF filled with Kr atoms at a pressure of 5 bars and subsequently in a 2-mm-thick plate of YAG crystal using 30 μJ of the 1 mJ, 25 fs output pulses of the Ti:sapphire amplifier. The three subsequent stages of OPCPA used 2 mm LBO, 2 mm BBO, and 4 mm LBO as the nonlinear crystal, amplifying the spectral ranges of 800–1350, 670–1000, and 800–1350 nm, respectively. 1 mJ of a total energy of approximately 8 mJ of the 1.7 ps, 515 nm pump pulse drove the first stage, with the remaining energy and its fraction transmitted by the second stage pumping the second and third stages, respectively.

Figure 12(c) shows the spectrum of the amplified pulses supporting a transform-limited pulse duration of 4.3 fs (FWHM). The preliminary compression of the amplified spectrum to sub-10-fs pulses, utilizing a (not-yet-optimized) set of chirped mirrors, reveals a well-behaved spectral phase of the amplified signal, indicating its compressibility to the Fourier limit. The energy of the amplified pulses was 1.8 mJ, with negligible ASE content. The amplified bandwidth supporting sub-5-fs pulses and the conversion efficiency in excess of 20% achieved already in preliminary experiments create confidence in the predictions of our modeling.

F. Power of 3FST: Synthesis of Multi-Octave, Multiterawatt Light Transients

Waveform-controlled light transients with a bandwidth approaching two octaves have been demonstrated at microjoule energy and gigawatt peak power levels [173,184,195,196]. They allow temporal confinement of optical radiation to less than 1 femtosecond in subcycle waveforms [197,198]. With their power substantially enhanced, these extreme waveforms may open up a new chapter in nonlinear optics and attosecond science (thanks to, among other things, the feasibility of suppressing ionization up to unprecedented peak intensities and instantaneous ionization rates approaching optical frequencies, respectively). The prototypical three-color few-cycle OPCPA system described in the previous section offers a conceptually simple route to scaling multi-octave optical waveform synthesis to the multiterawatt regime.

To this end, the three channels delivering few-cycle pulses in the VIS, NIR, and MIR spectral ranges are recombined using a set of dichroic chirped mirrors to yield one beam in a scheme similar to that reported in [175,184]. Due to the difficulties of dispersion management, the high demands on a chirped-mirror compressor, and the required coating for the

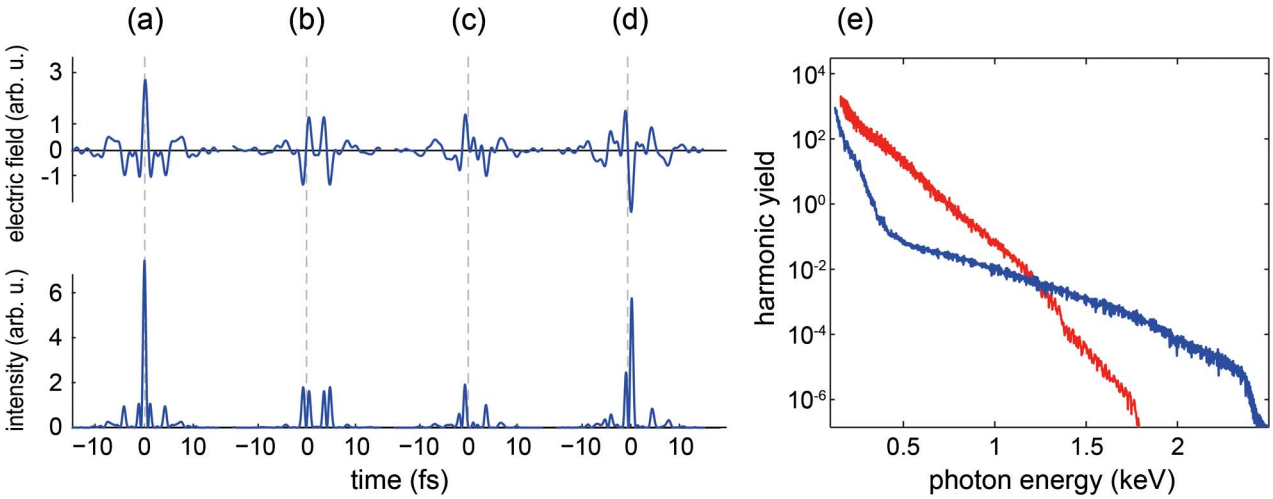

Fig. 13. Calculated synthesized waveforms from the three-channel OPCPA system and high-harmonic generation using synthesized waveforms (Section 3.E). (a) Fourier-transform-limited waveform; (b), (c) synthesized waveforms generated by changing the relative energy and time delay between different arms; (d) optimized waveform for HHG in terms of the highest cutoff energy of the synthesizer; (e) simulated HHG spectrum in helium. The red line represents the Gaussian-shaped pulse with 5 fs FWHM, whereas the blue line corresponds to the preoptimized waveform shown in (d).

OPCPA crystals in serial pulse synthesis [195], a parallel-synthesis [199] approach is chosen. Furthermore, fluctuations and drifts in the relative timing of the recombined pulses need to be suppressed to a tiny fraction of the half-field cycle for a stable waveform resulting from the coherent superposition [200]. This optical timing synchronization can be accomplished with the required sub-100-as precision with a balanced optical cross correlator demonstrated recently [175,196]. The feasibility of super-octave optical waveform synthesis was recently demonstrated in the NIR–VIS–UV spectral range by seeding a three-channel [184] and, more recently, four-channel [197] synthesizer consisting of broadband chirped mirrors with a continuum originating from a Ti:sapphire-laser-driven hollow-fiber/chirped-mirror compressor. Implementation with an OPA system is also being prepared [199,201,202].

Merely the adjustment of the relative timing of the three pulses emerging from the three OPA channels can result in a great variety of electric field forms on the time scale of the optical cycle. In fact, Figs. 13(a)–13(d) depict a few representative waveforms that may be synthesized from bandwidth-limited pulses emerging from the three channels described in the preceding section by varying their relative timing upon recombination. Further degrees of freedom for waveform sculpting can be introduced by shaping the amplitude and phase of the spectra of the individual channels, e.g., via an acousto-optic pulse shaper [203] and/or a spatial light modulator [204].

4. CONCLUSIONS AND OUTLOOK

Femtosecond technology emerged from nonlinear optical techniques allowing both the production and the characterization of femtosecond laser pulses. Its first generation (1FST) relied on dye lasers and delivered femtosecond pulses with peak and average powers up to the 100 MW and 100 mW ranges, respectively, over a narrow spectral range largely confined to 600–900 nm. Broadband solid-state laser media with high saturation fluence and CPA heralded the second generation of femtosecond technology (2FST), allowing for a boost of the peak and average powers of sub-100-fs pulses to the multiterawatt or 10 W regime, respectively, but not both of them simultaneously. Powerful 2FST systems are able to produce femtosecond pulses over an extended range of frequencies from the far-IR to the extreme UV via coherent frequency conversion based on $\chi^{(2)}$ and $\chi^{(3)}$ nonlinearities. However, these secondary sources are limited to power levels that are several orders of magnitude lower. The range of carrier wavelengths of powerful primary 2FST sources is—similar to 1FST—rather limited, currently spanning about 0.7–1.1 μm.

Based on OPCPA driven by terawatt-scale pulses from ytterbium lasers at kilowatt-scale average power (so far demonstrated with water-cooled thin-disk and slab and cryogenically cooled thick-disk technologies), third-generation technology (3FST) allows boosting the peak *and* average powers of coherent femtosecond light *simultaneously* to the multiterawatt and hundreds of watts range, respectively. It is capable of doing so over a wavelength range extended to more than two octaves, spanning 0.45–2.5 μm with either

(i) tunable, synchronized, multicycle, VIS, NIR, MIR tens of femtoseconds duration pulses,
(ii) synchronized, few-cycle VIS, NIR, MIR few-femtosecond-duration pulses, or
(iii) subcycle to few-cycle light transients synthesized from all spectral components,

available within the above multi-octave region, in all cases with full control over the generated light waves. These operation modes are being offered by a single basic system architecture and basic instrumentation, providing an unprecedented versatility and variety of methodologies for ultrafast spectroscopy and nonlinear optics.

Driven by the primary 3FST sources outlined in Section 3, secondary sources of femtosecond light are likely to outperform their predecessors based on 2FST in several respects. Not only are 3FST-based secondary sources likely to exceed the power of their 2FST-based predecessors by orders of magnitude, but they may also dramatically extend their spectral coverage. As an example, we have scrutinized the capability of multiterawatt, multi-octave light transients to extend the photon energy frontier of attosecond pulses to several kiloelectron volts, to the boundary of the regime of hard x rays. With the preoptimized waveform presented in Fig. 13(d), our numerical simulations of HHG, based on the strong field approximation [205] in helium [see caption of Fig. 13(e) for details] show that synthesized multi-octave transients are superior to few-cycle pulses in pushing the frontiers of HHG into the regime of hard x rays. As a matter of fact, our preoptimized subcycle transients substantially increase the photon energy of the cutoff harmonics as compared to those generated by a 5 fs Gaussian pulse of identical peak power. Our preliminary study indicates that 3FST will be beneficial for extending the frontiers of attosecond science into the x-ray regime.

1FST provided real-time access to a wealth of microscopic phenomena for the first time and created the technological basis for the birth of femtochemistry, allowing direct insight into the making and breaking of chemical bonds. 2FST has also created entirely new research fields and technologies, such as laser-driven accelerators and attosecond science. 3FST holds promise for consequences of comparable impact. One of them may be the recording of movies of any microscopic motion outside the atomic core via attosecond x-ray diffraction.

5. FUNDING INFORMATION

Center for Advanced Laser Applications (CALA); German Federal Ministry of Education and Research (BMBF); Max-Planck-Institute of Quantum Optics (MPQ); Munich Center for Advanced Photonics (MAP); Deutsche Forschungsgemeinschaft (DFG) (EXC-158).

DEDICATION

This paper is dedicated to Gerard Mourou on the occasion of his 70th birthday. His invention, chirped-pulse amplification, laid the groundwork for both second-generation and third-generation femtosecond technology, and thereby for all fields of science relying on intense laser light. Thank you, Gerard!

ACKNOWLEDGMENTS

The authors acknowledge both direct and indirect contributions from a number of colleagues at MPQ and LMU. Most importantly, the pioneering work of Stefan Karsch, László Veisz, and co-workers in the field of high-power OPCPA has led to relevant progress and insight on which the current work draws. We thank Christian Hackenberger for preparing the graphical illustrations for this paper.

See Supplement 1 for supporting content.

REFERENCES AND NOTES

1. E. P. Ippen, C. V. Shank, and A. Dienes, "Passive mode locking of the cw dye laser," Appl. Phys. Lett. **21**, 348–350 (1972).
2. J. P. Letouzey and S. O. Sari, "Continuous pulse train dye laser using an open flowing passive absorber," Appl. Phys. Lett. **23**, 311–313 (1973).
3. C. V. Shank and E. P. Ippen, "Subpicosecond kilowatt pulses from a mode-locked cw dye laser," Appl. Phys. Lett. **24**, 373–375 (1974).
4. R. L. Fork, B. I. Greene, and C. V. Shank, "Generation of optical pulses shorter than 0.1 psec by colliding pulse mode-locking," Appl. Phys. Lett. **38**, 671–672 (1981).
5. W. Dietel, E. Dopel, D. Kuhlke, and B. Wilhelmi, "Pulses in the femtosecond range from a cw dye ring laser in the colliding pulse mode-locking (CPM) regime with down-chirp," Opt. Commun. **43**, 433–436 (1982).
6. W. Dietel, J. J. Fontaine, and J. C. Diels, "Intracavity pulse-compression with glass: a new method of generating pulses shorter than 60 fsec," Opt. Lett. **8**, 4–6 (1983).
7. J. A. Valdmanis, R. L. Fork, and J. P. Gordon, "Generation of optical pulses as short as 27 femtoseconds directly from a laser balancing self-phase modulation, group-velocity dispersion, saturable absorption, and saturable gain," Opt. Lett. **10**, 131–133 (1985).
8. W. H. Knox, M. C. Downer, R. L. Fork, and C. V. Shank, "Amplified femtosecond optical pulses and continuum generation at 5-kHz repetition rate," Opt. Lett. **9**, 552–554 (1984).
9. C. Rolland and P. B. Corkum, "Amplification of 70-fs-pulses in a high repetition rate XeCl pumped dye-laser amplifier," Opt. Commun. **59**, 64–68 (1986).
10. W. Kaiser, D. H. Auston, K. B. Eisenthal, R. M. Hochstrasser, C. K. Johnson, A. Laubereau, D. Linde, A. von der Seilmeier, C. V. Shank, and W. Zinth, *Ultrashort Laser Pulses: Generation and Applications* (Springer, 1993).
11. A. H. Zewail, "Femtochemistry: atomic-scale dynamics of the chemical bond," J. Phys. Chem. A **104**, 5660–5694 (2000).
12. P. F. Moulton, "Spectroscopic and laser characteristics of Ti-Al_2O_3," J. Opt. Soc. Am. B **3**, 125–133 (1986).
13. V. Petričević, S. K. Gayen, R. R. Alfano, K. Yamagishi, H. Anzai, and Y. Yamaguchi, "Laser action in chromium-doped forsterite," Appl. Phys. Lett. **52**, 1040–1042 (1988).
14. E. Sorokin, S. Naumov, and I. T. Sorokina, "Ultrabroadband infrared solid-state lasers," IEEE J. Sel. Top. Quantum Electron. **11**, 690–712 (2005).
15. D. Strickland and G. Mourou, "Compression of amplified chirped optical pulses," Opt. Commun. **56**, 219–221 (1985).
16. D. E. Spence, P. N. Kean, and W. Sibbett, "60-fsec pulse generation from a self-mode-locked Ti:sapphire laser," Opt. Lett. **16**, 42–44 (1991).
17. S. Backus, C. G. Durfee, G. Mourou, H. C. Kapteyn, and M. M. Murnane, "0.2-TW laser system at 1 kHz," Opt. Lett. **22**, 1256–1258 (1997).
18. Y. Nabekawa, Y. Kuramoto, T. Togashi, T. Sekikawa, and S. Watanabe, "Generation of 0.66-TW pulses at 1 kHz by a Ti:sapphire laser," Opt. Lett. **23**, 1384–1386 (1998).
19. R. Szipöcs, K. Ferencz, C. Spielmann, and F. Krausz, "Chirped multilayer coatings for broad-band dispersion control in femtosecond lasers," Opt. Lett. **19**, 201–203 (1994).
20. M. Nisoli, S. DeSilvestri, O. Svelto, R. Szipöcs, K. Ferencz, C. Spielmann, S. Sartania, and F. Krausz, "Compression of high-energy laser pulses below 5 fs," Opt. Lett. **22**, 522–524 (1997).
21. S. Sartania, Z. Cheng, M. Lenzner, G. Tempea, C. Spielmann, F. Krausz, and K. Ferencz, "Generation of O.1-TW 5-fs optical pulses at a 1-kHz repetition rate," Opt. Lett. **22**, 1562–1564 (1997).
22. F. Krausz and M. Ivanov, "Attosecond physics," Rev. Mod. Phys. **81**, 163–234 (2009).
23. G. A. Mourou, T. Tajima, and S. V. Bulanov, "Optics in the relativistic regime," Rev. Mod. Phys. **78**, 309–371 (2006).
24. Y. Chu, X. Liang, L. Yu, Y. Xu, L. Xu, L. Ma, X. Lu, Y. Liu, Y. Leng, R. Li, and Z. Xu, "High-contrast 2.0 petawatt Ti:sapphire laser system," Opt. Express **21**, 29231–29239 (2013).
25. S. Hädrich, A. Klenke, A. Hoffmann, T. Eidam, T. Gottschall, J. Rothhardt, J. Limpert, and A. Tünnermann, "Nonlinear compression to sub-30-fs, 0.5 mJ pulses at 135 W of average power," Opt. Lett. **38**, 3866–3869 (2013).
26. A. Dubietis, G. Jonusauskas, and A. Piskarskas, "Powerful femtosecond pulse generation by chirped and stretched pulse parametric amplification in BBO crystal," Opt. Commun. **88**, 437–440 (1992).
27. D. Du, X. Liu, G. Korn, J. Squier, and G. Mourou, "Laser-induced breakdown by impact ionization in SiO_2 with pulse widths from 7 ns to 150 fs," Appl. Phys. Lett. **64**, 3071–3073 (1994).
28. B. C. Stuart, M. D. Feit, A. M. Rubenchik, B. W. Shore, and M. D. Perry, "Laser-induced damage in dielectrics with nanosecond to subpicosecond pulses," Phys. Rev. Lett. **74**, 2248–2251 (1995).
29. M. Lenzner, J. Krüger, S. Sartania, Z. Cheng, C. Spielmann, G. Mourou, W. Kautek, and F. Krausz, "Femtosecond optical breakdown in dielectrics," Phys. Rev. Lett. **80**, 4076–4079 (1998).
30. C. Radzewicz, Y. B. Band, G. W. Pearson, and J. S. Krasinski, "Short pulse nonlinear frequency conversion without group-velocity-mismatch broadening," Opt. Commun. **117**, 295–302 (1995).
31. S. M. Saltiel, K. Koynov, B. Agate, and W. Sibbett, "Second-harmonic generation with focused beams under conditions of large group-velocity mismatch," J. Opt. Soc. Am. B **21**, 591–598 (2004).
32. C. Y. Chien, G. Korn, J. S. Coe, J. Squier, and G. Mourou, "Highly efficient second-harmonic generation of ultraintense Nd-glass laser pulses," Opt. Lett. **20**, 353–355 (1995).
33. P. Rußbüldt, J. Weitenberg, T. Sartorius, G. Rotarius, H. D. Hoffmann, and R. Poprawe, "Ytterbium Innoslab amplifiers—the high average power approach of ultrafast lasers," AIP Conf. Proc. **1462**, 120–123 (2012).
34. P. Russbueldt, T. Mans, G. Rotarius, J. Weitenberg, H. D. Hoffmann, and R. Poprawe, "400 W Yb:YAG Innoslab fs-amplifier," Opt. Express **17**, 12230–12245 (2009).
35. O. G. Peterson, S. A. Tuccio, and B. B. Snavely, "CW operation of an organic dye solution laser," Appl. Phys. Lett. **17**, 245–247 (1970).
36. M. DiDomenico, "Small-signal analysis of internal (coupling-type) modulation of lasers," J. Appl. Phys. **35**, 2870–2876 (1964).
37. L. E. Hargrove, R. L. Fork, and M. A. Pollack, "Locking of He-Ne laser modes induced by synchronous intracavity modulation," Appl. Phys. Lett. **5**, 4–5 (1964).
38. A. Yariv, "Internal modulation in multimode laser oscillators," J. Appl. Phys. **36**, 388–391 (1965).
39. E. P. Ippen and C. V. Shank, "Dynamic spectroscopy and subpicosecond pulse compression," Appl. Phys. Lett. **27**, 488–490 (1975).
40. J. C. Diels, E. Vanstryland, and G. Benedict, "Generation and measurement of 200 femtosecond optical pulses," Opt. Commun. **25**, 93–96 (1978).
41. E. B. Treacy, "Measurement of picosecond pulse substructure using compression techniques," Appl. Phys. Lett. **14**, 112–114 (1969).
42. R. L. Fork, C. H. B. Cruz, P. C. Becker, and C. V. Shank, "Compression of optical pulses to six femtoseconds by using cubic phase compensation," Opt. Lett. **12**, 483–485 (1987).

43. C. V. Shank, "Generation of ultrashort optical pulses," Top. Appl. Phys. **60**, 5–34 (1988).
44. J. C. Diels, "Femtosecond dye lasers," in *Dye Laser Principles*, F. J. Duarte and L. W. Hillman, eds. (Academic, 1990), Chap. 3, pp. 41–132.
45. P. M. W. French, "The generation of ultrashort laser pulses," Rep. Prog. Phys. **58**, 169–262 (1995).
46. U. Keller, G. W. Thooft, W. H. Knox, and J. E. Cunningham, "Femtosecond pulses from a continuously self-starting passively mode-locked Ti:sapphire laser," Opt. Lett. **16**, 1022–1024 (1991).
47. L. Spinelli, B. Couillaud, N. Goldblatt, and D. K. Negus, "Starting and generation of sub-100 fs pulses in Ti:Al_2O_3 by self-focusing," in *Conference on Lasers and Electro-Optics*, J. Bufton, A. Glass, T. Hsu, and W. Krupke, eds., Vol. **10** of OSA Technical Digest (Optical Society of America, 1991), paper CPD7.
48. M. Piche, "Beam reshaping and self-mode-locking in nonlinear laser resonators," Opt. Commun. **86**, 156–160 (1991).
49. T. Brabec, C. Spielmann, P. F. Curley, and F. Krausz, "Kerr lens mode-locking," Opt. Lett. **17**, 1292–1294 (1992).
50. H. A. Haus, J. G. Fujimoto, and E. P. Ippen, "Analytic theory of additive pulse and Kerr lens mode locking," IEEE J. Quantum Electron. **28**, 2086–2096 (1992).
51. V. P. Kalosha, M. Muller, J. Herrmann, and S. Gatz, "Spatiotemporal model of femtosecond pulse generation in Kerr-lens mode-locked solid-state lasers," J. Opt. Soc. Am. B **15**, 535–550 (1998).
52. R. Szipöcs, A. Stingl, C. Spielmann, and F. Krausz, "Chirped dielectric mirrors for dispersion control in femtosecond laser systems," Proc. SPIE **2377**, 11–22 (1995).
53. A. Stingl, M. Lenzner, C. Spielmann, F. Krausz, and R. Szipöcs, "Sub-10-fs mirror-dispersion-controlled Ti:sapphire laser," Opt. Lett. **20**, 602–604 (1995).
54. A. Kasper and K. J. Witte, "10-fs pulse generation from a unidirectional Kerr-lens mode-locked Ti:sapphire ring laser," Opt. Lett. **21**, 360–362 (1996).
55. T. Brabec and F. Krausz, "Intense few-cycle laser fields: frontiers of nonlinear optics," Rev. Mod. Phys. **72**, 545–591 (2000).
56. P. Maine, D. Strickland, P. Bado, M. Pessot, and G. Mourou, "Generation of ultrahigh peak power pulses by chirped pulse amplification," IEEE J. Quantum Electron. **24**, 398–403 (1988).
57. J. V. Rudd, G. Korn, S. Kane, J. Squier, G. Mourou, and P. Bado, "Chirped-pulse amplification of 55-fs pulses at a 1-kHz repetition rate in a Ti-Al_2O_3 regenerative amplifier," Opt. Lett. **18**, 2044–2046 (1993).
58. O. E. Martinez, "Design of high-power ultrashort pulse amplifiers by expansion and recompression," IEEE J. Quantum Electron. **23**, 1385–1387 (1987).
59. C. P. J. Barty, G. Korn, F. Raksi, A. C. Tien, K. R. Wilson, V. V. Yakovlev, C. Rose-Petruck, J. Squier, and K. Yamakawa, "Regenerative pulse shaping and amplification of ultrabroadband optical pulses," Opt. Lett. **21**, 219–221 (1996).
60. M. Hentschel, Z. Cheng, F. Krausz, and C. Spielmann, "Generation of 0.1-TW optical pulses with a single-stage Ti:sapphire amplifier at a 1-kHz repetition rate," Appl. Phys. B **70**, S161–S164 (2000).
61. J. Z. H. Yang and B. C. Walker, "0.09-terawatt pulses with a 31% efficient, kilohertz repetition-rate Ti:sapphire regenerative amplifier," Opt. Lett. **26**, 453–455 (2001).
62. S. Backus, R. Bartels, S. Thompson, R. Dollinger, M. Murnane, and H. Kapteyn, "High efficiency, single-stage, 7 kHz, high average power ultrafast laser system," in *Conference on Lasers and Electro-Optics*, Baltimore, Maryland, 2001.
63. D. M. Gaudiosi, A. L. Lytle, P. Kohl, M. M. Murnane, H. C. Kapteyn, and S. Backus, "11-W average power Ti:sapphire amplifier system using downchirped pulse amplification," Opt. Lett. **29**, 2665–2667 (2004).
64. J. Huve, T. Haarlammert, T. Steinbruck, J. Kutzner, G. Tsilimis, and H. Zacharias, "High-flux high harmonic soft x-ray generation up to 10 kHz repetition rate," Opt. Commun. **266**, 261–265 (2006).
65. T. Imahoko, N. Inoue, K. Takasago, T. Sumiyoshi, H. Sekita, and M. Obara, "Development of a 50 kHz, 13 W Ti:sapphire femtosecond regenerative amplifier," in *Pacific Rim Conference on Lasers and Electro-Optics* (IEEE, 2007), pp. 774–775.
66. S. Chen, M. Chini, H. Wang, C. Yun, H. Mashiko, Y. Wu, and Z. Chang, "Carrier-envelope phase stabilization and control of 1 kHz, 6 mJ, 30 fs laser pulses from a Ti:sapphire regenerative amplifier," Appl. Opt. **48**, 5692–5695 (2009).
67. I. Matsushima, H. Yashiro, and T. Tomie, "10 kHz 40 W Ti:sapphire regenerative ring amplifier," Opt. Lett. **31**, 2066–2068 (2006).
68. M. Nisoli, S. DeSilvestri, and O. Svelto, "Generation of high energy 10 fs pulses by a new pulse compression technique," Appl. Phys. Lett. **68**, 2793–2795 (1996).
69. E. Goulielmakis, M. Schultze, M. Hofstetter, V. S. Yakovlev, J. Gagnon, M. Uiberacker, A. L. Aquila, E. M. Gullikson, D. T. Attwood, R. Kienberger, F. Krausz, and U. Kleineberg, "Single-cycle nonlinear optics," Science **320**, 1614–1617 (2008).
70. A. L. Cavalieri, E. Goulielmakis, B. Horvath, W. Helml, M. Schultze, M. Fieß, V. Pervak, L. Veisz, V. S. Yakovlev, M. Uiberacker, A. Apolonski, F. Krausz, and R. Kienberger, "Intense 1.5-cycle near infrared laser waveforms and their use for the generation of ultrabroadband soft-x-ray harmonic continua," New J. Phys. **9**, 242 (2007).
71. S. Bohman, A. Suda, T. Kanai, S. Yamaguchi, and K. Midorikawa, "Generation of 5.0 fs, 5.0 mJ pulses at 1 kHz using hollow-fiber pulse compression," Opt. Lett. **35**, 1887–1889 (2010).
72. W. Schweinberger, A. Sommer, E. Bothschafter, J. Li, F. Krausz, R. Kienberger, and M. Schultze, "Waveform-controlled near-single-cycle milli-joule laser pulses generate sub-10 nm extreme ultraviolet continua," Opt. Lett. **37**, 3573–3575 (2012).
73. U. Morgner, F. X. Kartner, S. H. Cho, Y. Chen, H. A. Haus, J. G. Fujimoto, E. P. Ippen, V. Scheuer, G. Angelow, and T. Tschudi, "Sub-two-cycle pulses from a Kerr-lens mode-locked Ti:sapphire laser," Opt. Lett. **24**, 411–413 (1999).
74. C. C. Wang and G. W. Racette, "Measurement of parametric gain accompanying optical difference frequency generation," Appl. Phys. Lett. **6**, 169–171 (1965).
75. S. E. Harris, M. K. Oshman, and R. L. Byer, "Observation of tunable optical parametric fluorescence," Phys. Rev. Lett. **18**, 732–734 (1967).
76. C. Chen, B. Wu, A. Jiang, and G. You, "A new-type ultraviolet SHG crystal: β-BaB_2O_4," Sci. Sin. Ser. B **28**, 235–243 (1985).
77. T. Wilhelm, J. Piel, and E. Riedle, "Sub-20-fs pulses tunable across the visible from a blue-pumped single-pass noncollinear parametric converter," Opt. Lett. **22**, 1494–1496 (1997).
78. E. Riedle, M. Beutter, S. Lochbrunner, J. Piel, S. Schenkl, S. Sporlein, and W. Zinth, "Generation of 10 to 50 fs pulses tunable through all of the visible and the NIR," Appl. Phys. B **71**, 457–465 (2000).
79. R. Butkus, R. Danielius, A. Dubietis, A. Piskarskas, and A. Stabinis, "Progress in chirped pulse optical parametric amplifiers," Appl. Phys. B **79**, 693–700 (2004).
80. A. Dubietis, R. Butkus, and A. P. Piskarskas, "Trends in chirped pulse optical parametric amplification," IEEE J. Sel. Top. Quantum Electron. **12**, 163–172 (2006).
81. S. Witte and K. S. E. Eikema, "Ultrafast optical parametric chirped-pulse amplification," IEEE J. Sel. Top. Quantum Electron. **18**, 296–307 (2012).
82. A. Vaupel, N. Bodnar, B. Webb, L. Shah, and M. Richardson, "Concepts, performance review, and prospects of table-top, few-cycle optical parametric chirped-pulse amplification," Opt. Eng. **53**, 051507 (2014).
83. G. Cerullo and S. De Silvestri, "Ultrafast optical parametric amplifiers," Rev. Sci. Instrum. **74**, 1–18 (2003).
84. A. Baltuska, T. Fuji, and T. Kobayashi, "Visible pulse compression to 4 fs by optical parametric amplification and programmable dispersion control," Opt. Lett. **27**, 306–308 (2002).
85. D. Herrmann, L. Veisz, R. Tautz, F. Tavella, K. Schmid, V. Pervak, and F. Krausz, "Generation of sub-three-cycle, 16 TW light pulses by using noncollinear optical parametric chirped-pulse amplification," Opt. Lett. **34**, 2459–2461 (2009).

86. I. N. Ross, P. Matousek, M. Towrie, A. J. Langley, and J. L. Collier, "The prospects for ultrashort pulse duration and ultrahigh intensity using optical parametric chirped pulse amplifiers," Opt. Commun. **144**, 125–133 (1997).
87. I. N. Ross, P. Matousek, G. H. C. New, and K. Osvay, "Analysis and optimization of optical parametric chirped pulse amplification," J. Opt. Soc. Am. B **19**, 2945–2956 (2002).
88. C. N. Danson, P. A. Brummitt, R. J. Clarke, J. L. Collier, B. Fell, A. J. Frackiewicz, S. Hawkes, C. Hernandez-Gomez, P. Holligan, M. H. R. Hutchinson, A. Kidd, W. J. Lester, I. O. Musgrave, D. Neely, D. R. Neville, P. A. Norreys, D. A. Pepler, C. Reason, W. Shaikh, T. B. Winstone, R. W. W. Wyatt, and B. E. Wyborn, "Vulcan petawatt: design, operation and interactions at 5×10^{20} Wcm^{-2}," Laser Part. Beams **23**, 87–93 (2005).
89. O. V. Chekhlov, J. L. Collier, I. N. Ross, P. K. Bates, M. Notley, C. Hernandez-Gomez, W. Shaikh, C. N. Danson, D. Neely, P. Matousek, S. Hancock, and L. Cardoso, "35 J broadband femtosecond optical parametric chirped pulse amplification system," Opt. Lett. **31**, 3665–3667 (2006).
90. V. V. Lozhkarev, G. I. Freidman, V. N. Ginzburg, E. V. Katin, E. A. Khazanov, A. V. Kirsanov, G. A. Luchinin, A. N. Mal'shakov, M. A. Martyanov, O. V. Palashov, A. K. Poteomkin, A. M. Sergeev, A. A. Shaykin, and I. V. Yakovlev, "Compact 0.56 petawatt laser system based on optical parametric chirped pulse amplification in KD*P crystals," Laser Phys. Lett. **4**, 421–427 (2007).
91. Z. Major, S. Trushin, I. Ahmad, M. Siebold, C. Wandt, S. Klingebiel, T.-J. Wang, J. A. Fülöp, A. Henig, S. Kruber, R. Weingartner, A. Popp, J. Osterhoff, R. Hörlein, J. Hein, V. Pervak, A. Apolonski, F. Krausz, and S. Karsch, "Basic concepts and current status of the petawatt field synthesizer—a new approach to ultrahigh field generation," Rev. Laser Eng. **37**, 431–436 (2009).
92. O. Novak, M. Divoky, H. Turcicova, and P. Straka, "Design of a petawatt optical parametric chirped pulse amplification upgrade of the kilojoule iodine laser PALS," Laser Part. Beams **31**, 211–218 (2013).
93. J. Rothhardt, S. Demmler, S. Hadrich, J. Limpert, and A. Tunnermann, "Octave-spanning OPCPA system delivering CEP-stable few-cycle pulses and 22 W of average power at 1 MHz repetition rate," Opt. Express **20**, 10870–10878 (2012).
94. S. Adachi, N. Ishii, T. Kanai, A. Kosuge, J. Itatani, Y. Kobayashi, D. Yoshitomi, K. Torizuka, and S. Watanabe, "5-fs, multi-mJ, CEP-locked parametric chirped-pulse amplifier pumped by a 450-nm source at 1 kHz," Opt. Express **16**, 14341–14352 (2008).
95. D. J. Bradley and W. Sibbett, "Streak-camera studies of picosecond pulses from a mode-locked Nd: glass laser," Opt. Commun. **9**, 17–20 (1973).
96. T. R. Royt, "Passive mode-locking of the Nd-glass oscillator at high repetition rate with thermally compensated phosphate glasses," Opt. Commun. **35**, 271–276 (1980).
97. L. S. Goldberg, P. E. Schoen, and M. J. Marrone, "Repetitively pulsed mode-locked Nd:phosphate glass laser oscillator-amplifier system," Appl. Opt. **21**, 1474–1477 (1982).
98. S. Tokita, J. Kawanaka, Y. Izawa, M. Fujita, and T. Kawashima, "23.7-W picosecond cryogenic-Yb:YAG multipass amplifier," Opt. Express **15**, 3955–3961 (2007).
99. P. Russbueldt, T. Mans, J. Weitenberg, H. D. Hoffmann, and R. Poprawe, "Compact diode-pumped 1.1 kW Yb:YAG Innoslab femtosecond amplifier," Opt. Lett. **35**, 4169–4171 (2010).
100. T. Eidam, S. Hanf, E. Seise, T. V. Andersen, T. Gabler, C. Wirth, T. Schreiber, J. Limpert, and A. Tünnermann, "Femtosecond fiber CPA system emitting 830 W average output power," Opt. Lett. **35**, 94–96 (2010).
101. K.-H. Hong, J. T. Gopinath, D. Rand, A. M. Siddiqui, S.-W. Huang, E. Li, B. J. Eggleton, J. D. Hybl, T. Y. Fan, and F. X. Kärtner, "High-energy, kHz-repetition-rate, ps cryogenic Yb:YAG chirped-pulse amplifier," Opt. Lett. **35**, 1752–1754 (2010).
102. J. Rothhardt, S. Hädrich, H. Carstens, N. Herrick, S. Demmler, J. Limpert, and A. Tünnermann, "1 MHz repetition rate hollow fiber pulse compression to sub-100-fs duration at 100 W average power," Opt. Lett. **36**, 4605–4607 (2011).
103. D. A. Rand, S. E. J. Shaw, J. R. Ochoa, D. J. Ripin, A. Taylor, T. Y. Fan, H. Martin, S. Hawes, J. Zhang, S. Sarkisyan, E. Wilson, and P. Lundquist, "Picosecond pulses from a cryogenically cooled, composite amplifier using Yb:YAG and Yb:GSAG," Opt. Lett. **36**, 340–342 (2011).
104. K. Kowalewski, J. Zembek, V. Envid, and D. C. Brown, "201 W picosecond green laser using a mode-locked fiber laser driven cryogenic Yb:YAG amplifier system," Opt. Lett. **37**, 4633–4635 (2012).
105. K. F. Wall, D. E. Miller, and T. Y. Fan, "Cryo-Yb:YAG lasers for next-generation photoinjector applications," Proc. SPIE **8235**, 823512 (2012).
106. A. Klenke, S. Breitkopf, M. Kienel, T. Gottschall, T. Eidam, S. Hädrich, J. Rothhardt, J. Limpert, and A. Tünnermann, "530 W, 1.3 mJ, four-channel coherently combined femtosecond fiber chirped-pulse amplification system," Opt. Lett. **38**, 2283–2285 (2013).
107. C. Jauregui, J. Limpert, and A. Tünnermann, "High-power fibre lasers," Nat. Photonics **7**, 861–867 (2013).
108. R. Riedel, A. Stephanides, M. J. Prandolini, B. Gronloh, B. Jungbluth, T. Mans, and F. Tavella, "Power scaling of supercontinuum seeded megahertz-repetition rate optical parametric chirped pulse amplifiers," Opt. Lett. **39**, 1422–1424 (2014).
109. B. A. Reagan, C. Baumgarten, K. Wernsing, H. Bravo, M. Woolston, A. Curtis, F. J. Furch, B. Luther, D. Patel, C. Menoni, and J. J. Rocca, "1 Joule, 100 Hz repetition rate, picosecond CPA laser for driving high average power soft x-ray lasers," in *CLEO*, OSA Technical Digest (online) (Optical Society of America, 2014), paper SM1F.4.
110. M. Schulz, R. Riedel, A. Willner, T. Mans, C. Schnitzler, P. Russbueldt, J. Dolkemeyer, E. Seise, T. Gottschall, S. Hädrich, S. Duesterer, H. Schlarb, J. Feldhaus, J. Limpert, B. Faatz, A. Tünnermann, J. Rossbach, M. Drescher, and F. Tavella, "Yb:YAG Innoslab amplifier: efficient high repetition rate subpicosecond pumping system for optical parametric chirped pulse amplification," Opt. Lett. **36**, 2456–2458 (2011).
111. G. Mourou, B. Brocklesby, T. Tajima, and J. Limpert, "The future is fibre accelerators," Nat. Photonics **7**, 258–261 (2013).
112. S. Breitkopf, "A path to terawatt peak-power fibre laser systems" (submitted).
113. G. Huber, C. Kränkel, and K. Petermann, "Solid-state lasers: status and future," J. Opt. Soc. Am. B **27**, B93–B105 (2010).
114. D. J. Richardson, J. Nilsson, and W. A. Clarkson, "High power fiber lasers: current status and future perspectives," J. Opt. Soc. Am. B **27**, B63–B92 (2010).
115. J. W. Dawson, J. K. Crane, M. J. Messerly, M. A. Prantil, P. H. Pax, A. K. Sridharan, G. S. Allen, D. R. Drachenberg, H. H. Phan, J. E. Heebner, C. A. Ebbers, R. J. Beach, E. P. Hartouni, C. W. Siders, T. M. Spinka, C. P. J. Barty, A. J. Bayramian, L. C. Haefner, F. Albert, W. H. Lowdermilk, A. M. Rubenchik, and R. E. Bonanno, "High average power lasers for future particle accelerators," AIP Conf. Proc. **1507**, 147–153 (2012).
116. M. E. Fermann and I. Hartl, "Ultrafast fibre lasers," Nat. Photonics **7**, 868–874 (2013).
117. A. Giesen, H. Hügel, A. Voss, K. Wittig, U. Brauch, and H. Opower, "Scalable concept for diode-pumped high-power solid-state lasers," Appl. Phys. B **58**, 365–372 (1994).
118. A. Giesen and J. Speiser, "Fifteen years of work on thin-disk lasers: results and scaling laws," IEEE J. Sel. Top. Quantum Electron. **13**, 598–609 (2007).
119. D. Kouznetsov, J.-F. Bisson, and K. Ueda, "Scaling laws of disk lasers," Opt. Mater. **31**, 754–759 (2009).
120. J. Speiser, "Scaling of thin-disk lasers—influence of amplified spontaneous emission," J. Opt. Soc. Am. B **26**, 26–35 (2009).
121. S. V. Marchese, C. R. E. Baer, R. Peters, C. Kränkel, A. G. Engqvist, M. Golling, D. J. H. C. Maas, K. Petermann, T. Südmeyer, G. Huber, and U. Keller, "Efficient femtosecond high power Yb:Lu_2O_3 thin disk laser," Opt. Express **15**, 16966–16971 (2007).

122. C. R. E. Baer, C. Kränkel, C. J. Saraceno, O. H. Heckl, M. Golling, T. Südmeyer, R. Peters, K. Petermann, G. Huber, and U. Keller, "Femtosecond Yb:Lu_2O_3 thin disk laser with 63 W of average power," Opt. Lett. **34**, 2823–2825 (2009).
123. S. Ricaud, A. Jaffres, P. Loiseau, B. Viana, B. Weichelt, M. Abdou-Ahmed, A. Voss, T. Graf, D. Rytz, M. Delaigue, E. Mottay, P. Georges, and F. Druon, "Yb:$CaGdAlO_4$ thin-disk laser," Opt. Lett. **36**, 4134–4136 (2011).
124. W. P. Latham, A. Lobad, T. C. Newell, and D. Stalnaker, "6.5 kW, Yb:YAG ceramic thin disk laser," AIP Conf. Proc. **1278**, 758–764 (2010).
125. M. Suzuki, H. Kiriyama, I. Daito, Y. Ochi, H. Okada, M. Sato, Y. Tamaoki, T. Yoshii, J. Maeda, S. Matsuoka, H. Kan, P. R. Bolton, A. Sugiyama, K. Kondo, and S. Kawanishi, "Hundred mJ, sub-picoseconds, high temporal contrast OPCPA/Yb:YAG ceramic thin disk hybrid laser system," Appl. Phys. B **105**, 181–184 (2011).
126. J. Mende, G. Spindler, J. Speiser, W. L. Bohn, and A. Giesen, "Mode dynamics and thermal lens effects of thin-disk lasers," Proc. SPIE **6871**, 68710M (2008).
127. A. Killi, C. Stolzenburg, I. Zawischa, D. Sutter, J. Kleinbauer, S. Schad, R. Brockmann, S. Weiler, J. Neuhaus, S. Kalfhues, E. Mehner, D. Bauer, H. Schlueter, and C. Schmitz, "The broad applicability of the disk laser principle: from CW to ps," Proc. SPIE **7193**, 71931T (2009).
128. A. Antognini, K. Schuhmann, F. D. Amaro, F. Biraben, A. Dax, A. Giesen, T. Graf, T. W. Hansch, P. Indelicato, L. Julien, C.-Y. Kao, P. E. Knowles, F. Kottmann, E. Le Bigot, Y.-W. Liu, L. Ludhova, N. Moschuring, F. Mulhauser, T. Nebel, F. Nez, P. Rabinowitz, C. Schwob, D. Taqqu, and R. Pohl, "Thin-disk Yb:YAG oscillator-amplifier laser, ASE, and effective Yb:YAG lifetime," IEEE J. Quantum Electron. **45**, 993–1005 (2009).
129. H. Furuse, H. Chosrowjan, J. Kawanaka, N. Miyanaga, M. Fujita, and Y. Izawa, "ASE and parasitic lasing in thin disk laser with anti-ASE cap," Opt. Express **21**, 13118–13124 (2013).
130. D. Bauer, I. Zawischa, D. H. Sutter, A. Killi, and T. Dekorsy, "Mode-locked Yb:YAG thin-disk oscillator with 41 μJ pulse energy at 145 W average infrared power and high power frequency conversion," Opt Express **20**, 9698–9704 (2012).
131. S. Ricaud, A. Jaffres, K. Wentsch, A. Suganuma, B. Viana, P. Loiseau, B. Weichelt, M. Abdou-Ahmed, A. Voss, T. Graf, D. Rytz, C. Hönninger, E. Mottay, P. Georges, and F. Druon, "Femtosecond Yb:$CaGdAlO_4$ thin-disk oscillator," Opt. Lett. **37**, 3984–3986 (2012).
132. O. Pronin, J. Brons, C. Grasse, V. Pervak, G. Boehm, M. C. Amann, A. Apolonski, V. L. Kalashnikov, and F. Krausz, "High-power Kerr-lens mode-locked Yb:YAG thin-disk oscillator in the positive dispersion regime," Opt. Lett. **37**, 3543–3545 (2012).
133. C. J. Saraceno, F. Emaury, C. Schriber, M. Hoffmann, M. Golling, T. Südmeyer, and U. Keller, "Ultrafast thin-disk laser with 80 μJ pulse energy and 242 W of average power," Opt. Lett. **39**, 9–12 (2014).
134. C. Teisset, M. Schultze, R. Bessing, M. Häfner, J. Rauschenberger, D. Sutter, and T. Metzger, "Picosecond thin-disk regenerative amplifier with high average power for pumping optical parametric amplifiers," in *CLEO*, OSA Postdeadline Paper Digest (online) (Optical Society of America, 2013), paper CTh5C.6.
135. J.-P. Negel, A. Voss, M. A. Ahmed, D. Bauer, D. Sutter, A. Killi, and T. Graf, "1.1 kW average output power from a thin-disk multipass amplifier for ultrashort laser pulses," Opt. Lett. **38**, 5442–5445 (2013).
136. H. Fattahi, C. Skrobol, M. Ueffing, Y. Deng, A. Schwarz, Y. Kida, V. Pervak, T. Metzger, Z. Major, and F. Krausz, "High efficiency, multi-mJ, sub 10 fs, optical parametric amplifier at 3 kHz," in *Conference on Lasers and Electro-Optics*, OSA Technical Digest (online) (Optical Society of America, 2012), paper CTh1N.6.
137. J. Aus der Au, G. J. Spuhler, T. Südmeyer, R. Paschotta, R. Hovel, M. Moser, S. Erhard, M. Karszewski, A. Giesen, and U. Keller, "16.2-W average power from a diode-pumped femtosecond Yb: YAG thin disk laser," Opt. Lett. **25**, 859–861 (2000).
138. C. J. Saraceno, F. Emaury, O. H. Heckl, C. R. E. Baer, M. Hoffmann, C. Schriber, M. Golling, T. Südmeyer, and U. Keller, "275 W average output power from a femtosecond thin disk oscillator operated in a vacuum environment," Opt. Express **20**, 23535–23541 (2012).
139. S. V. Marchese, C. R. Baer, A. G. Engqvist, S. Hashimoto, D. J. Maas, M. Golling, T. Sudmeyer, and U. Keller, "Femtosecond thin disk laser oscillator with pulse energy beyond the 10-microjoule level," Opt Express **16**, 6397–6407 (2008).
140. J. Brons, V. Pervak, E. Fedulova, M. Seidel, D. Bauer, D. Sutter, V. L. Kalashnikov, A. Apolonski, O. Pronin, and F. Krausz, "Power-scaling of Kerr-lens mode-locked Yb:YAG thin-disk oscillators," in *CLEO*, OSA Technical Digest (online) (Optical Society of America, 2014), paper SM4F.7.
141. A. Diebold, F. Emaury, C. Schriber, M. Golling, C. J. Saraceno, T. Südmeyer, and U. Keller, "SESAM mode-locked Yb:$CaGdAlO_4$ thin disk laser with 62 fs pulse generation," Opt. Lett. **38**, 3842–3845 (2013).
142. C. J. Saraceno, C. Schriber, M. Mangold, M. Hoffmann, O. H. Heckl, C. R. Baer, M. Golling, T. Südmeyer, and U. Keller, "SESAMs for high-power oscillators: design guidelines and damage thresholds," IEEE J. Sel. Top. Quantum Electron. **18**, 29–41 (2012).
143. O. Pronin, J. Brons, C. Grasse, V. Pervak, G. Boehm, M. C. Amann, V. L. Kalashnikov, A. Apolonski, and F. Krausz, "High-power 200 fs Kerr-lens mode-locked Yb:YAG thin-disk oscillator," Opt. Lett. **36**, 4746–4748 (2011).
144. O. Pronin, M. Seidel, F. Lücking, J. Brons, V. Pervak, A. Apolonski, T. Udem, and F. Krausz, "Next-generation source of waveform-controlled light" (submitted).
145. C. Hönninger, I. Johannsen, M. Moser, G. Zhang, A. Giesen, and U. Keller, "Diode-pumped thin-disk Yb:YAG regenerative amplifier," Appl. Phys. B **65**, 423–426 (1997).
146. T. Metzger, C. Y. Teisset, and F. Krausz, "High-repetition-rate picosecond pump laser based on a Yb:YAG disk amplifier for optical parametric amplification," in *Advanced Solid-State Photonics*, OSA Technical Digest Series (CD) (Optical Society of America, 2008), paper TuA2.
147. C. Teisset, M. Schultze, R. Bessing, M. Haefner, S. Prinz, D. Sutter, and T. Metzger, "300 W picosecond thin-disk regenerative amplifier at 10 kHz repetition rate," in *Advanced Solid-State Lasers Congress Postdeadline*, OSA Postdeadline Paper Digest (online) (Optical Society of America, 2013), paper JTh5A.1.
148. J. Tuemmler, R. Jung, T. Nubbemeyer, I. Will, and W. Sandner, "Providing thin-disk technology for high laser pulse energy at high average power," in *Frontiers in Optics 2011/Laser Science XXVII*, OSA Technical Digest (Optical Society of America, 2011), paper FThB3.
149. M. Schulz, H. Hoeppner, M. Temme, R. Riedel, B. Faatz, M. J. Prandolini, M. Drescher, and F. Tavella, "14 kilowatt burst average power from 2-stage cascaded Yb:YAG thin-disk multipass amplifier," in *Frontiers in Optics*, OSA Technical Digest (online) (Optical Society of America, 2013), paper FTu4A.2.
150. C. Skrobol, I. Ahmad, S. Klingebiel, C. Wandt, S. A. Trushin, Z. Major, F. Krausz, and S. Karsch, "Broadband amplification by picosecond OPCPA in DKDP pumped at 515 nm," Opt. Express **20**, 4619–4629 (2012).
151. S. Klingebiel, I. Ahmad, C. Wandt, C. Skrobol, S. A. Trushin, Z. Major, F. Krausz, and S. Karsch, "Experimental and theoretical investigation of timing jitter inside a stretcher-compressor setup," Opt. Express **20**, 3443–3455 (2012).
152. T. Miura, K. Takasago, A. Endo, K. Torizuka, and F. Kannari, "Timing stabilization of the 1-kHz femtosecond pulses with active control by means of the spectral-resolved upconversion," in *The 4th Pacific Rim Conference on Lasers and Electro-Optics* (IEEE, 2001), Vol. **2**, pp. 520–521.
153. A. Schwarz, M. Ueffing, Y. Deng, X. Gu, H. Fattahi, T. Metzger, M. Ossiander, F. Krausz, and R. Kienberger, "Active stabilization for optically synchronized optical parametric chirped pulse amplification," Opt. Express **20**, 5557–5565 (2012).

154. S. Prinz, "Sub-2-fs active pump-seed synchronization for OPCPA" (submitted).
155. J. Tümmler, R. Jung, H. Stiel, P. V. Nickles, and W. Sandner, "High-repetition-rate chirped-pulse-amplification thin-disk laser system with joule-level pulse energy," Opt. Lett. **34**, 1378–1380 (2009).
156. J. Tümmler, R. Jung, H. Stiel, P. V. Nickles, and W. Sandner, "High repetition rate diode pumped CPA thin disk laser of the joule class," in *Conference on Lasers and Electro-Optics/International Quantum Electronics Conference*, OSA Technical Digest (CD) (Optical Society of America, 2009), paper CFD4.
157. http://www.mb-berlin.de/de/research/projects/1.2/topics/1_power_disk_laser/.
158. M. Gorjan and T. Metzger, (unpublished).
159. J. Speiser, "Thin disk laser—energy scaling," Laser Phys. **19**, 274–280 (2009).
160. T. Gottwald, C. Stolzenburg, D. Bauer, J. Kleinbauer, V. Kuhn, T. Metzger, S. Schad, D. Sutter, and A. Killi, "Recent disk laser development at Trumpf," Proc. SPIE **8547**, 85470C (2012).
161. M. Kienel, M. Müller, S. Demmler, J. Rothhardt, A. Klenke, T. Eidam, J. Limpert, and A. Tünnermann, "Coherent beam combination of Yb:YAG single-crystal rod amplifiers," Opt. Lett. **39**, 3278–3281 (2014).
162. J. Limpert, "Performance scaling of ultrafast laser systems by coherent addition of femtosecond pulses," in *CLEO*, OSA Technical Digest (online) (Optical Society of America, 2014), paper SW3E.3.
163. M. Kienel, A. Klenke, T. Eidam, S. Hädrich, J. Limpert, and A. Tünnermann, "Energy scaling of femtosecond amplifiers using actively controlled divided-pulse amplification," Opt. Lett. **39**, 1049–1052 (2014).
164. D. Herrmann, C. Homann, R. Tautz, M. Scharrer, P. S. J. Russell, F. Krausz, L. Veisz, and E. Riedle, "Approaching the full octave: noncollinear optical parametric chirped pulse amplification with two-color pumping," Opt. Express **18**, 18752–18762 (2010).
165. Alternatively, momentum conservation can also be fulfilled by periodic modulation of some optical property of the nonlinear crystal (quasi-phase matching) instead of exploiting birefringence. Periodically poled crystals are being widely used for this purpose.
166. D. Brida, C. Manzoni, G. Cirmi, M. Marangoni, S. Bonora, P. Villoresi, S. D. Silvestri, and G. Cerullo, "Few-optical-cycle pulses tunable from the visible to the mid-infrared by optical parametric amplifiers," J. Opt. **12**, 013001 (2010).
167. R. Danielius, A. Piskarskas, A. Stabinis, G. P. Banfi, P. Di Trapani, and R. Righini, "Traveling-wave parametric generation of widely tunable, highly coherent femtosecond light pulses," J. Opt. Soc. Am. B **10**, 2222–2232 (1993).
168. T. J. Driscoll, G. M. Gale, and F. Hache, "Ti:sapphire second-harmonic-pumped visible range femtosecond optical parametric oscillator," Opt. Commun. **110**, 638–644 (1994).
169. G. M. Gale, M. Cavallari, T. J. Driscoll, and F. Hache, "Sub-20-fs tunable pulses in the visible from an 82-MHz optical parametric oscillator," Opt. Lett. **20**, 1562–1564 (1995).
170. G. M. Gale, M. Cavallari, and F. Hache, "Femtosecond visible optical parametric oscillator," J. Opt. Soc. Am. B **15**, 702–714 (1998).
171. Optical parametric amplification done in the frequency domain holds promise for relaxing restrictions arising from phase mismatch in OPA.
172. B. E. Schmidt, N. Thiré, M. Boivin, A. Laramée, F. Poitras, G. Lebrun, T. Ozaki, H. Ibrahim, and F. Légaré, "Frequency domain optical parametric amplification," Nat. Commun. **5**, 3643 (2014).
173. M. T. Hassan, A. Wirth, I. Grguraš, A. Moulet, T. T. Luu, J. Gagnon, V. Pervak, and E. Goulielmakis, "Invited Article: Attosecond photonics: synthesis and control of light transients," Rev. Sci. Instrum. **83**, 111301 (2012).
174. S.-W. Huang, G. Cirmi, J. Moses, K.-H. Hong, S. Bhardwaj, J. R. Birge, L.-J. Chen, E. Li, B. J. Eggleton, G. Cerullo, and F. X. Kartner, "High-energy pulse synthesis with sub-cycle waveform control for strong-field physics," Nat. Photonics **5**, 475–479 (2011).
175. S.-W. Huang, G. Cirmi, J. Moses, K.-H. Hong, S. Bhardwaj, J. R. Birge, L.-J. Chen, I. V. Kabakova, E. Li, B. J. Eggleton, G. Cerullo, and F. X. Kärtner, "Optical waveform synthesizer and its application to high-harmonic generation," J. Phys. B **45**, 074009 (2012).
176. C. Manzoni, G. Cerullo, and S. De Silvestri, "Ultrabroadband self-phase-stabilized pulses by difference-frequency generation," Opt. Lett. **29**, 2668–2670 (2004).
177. G. Cerullo, A. Baltuška, O. D. Mücke, and C. Vozzi, "Few-optical-cycle light pulses with passive carrier-envelope phase stabilization," Laser Photon. Rev. **5**, 323–351 (2011).
178. K.-H. Hong, S.-W. Huang, J. Moses, X. Fu, C.-J. Lai, G. Cirmi, A. Sell, E. Granados, P. Keathley, and F. X. Kärtner, "High-energy, phase-stable, ultrabroadband kHz OPCPA at 2.1 μm pumped by a picosecond cryogenic Yb:YAG laser," Opt. Express **19**, 15538–15548 (2011).
179. Y. Deng, A. Schwarz, H. Fattahi, M. Ueffing, X. Gu, M. Ossiander, T. Metzger, V. Pervak, H. Ishizuki, T. Taira, T. Kobayashi, G. Marcus, F. Krausz, R. Kienberger, and N. Karpowicz, "Carrier-envelope-phase-stable, 1.2 mJ, 1.5 cycle laser pulses at 2.1 μm," Opt. Lett. **37**, 4973–4975 (2012).
180. H. Fattahi, A. Schwarz, S. Keiber, and N. Karpowicz, "Efficient, octave-spanning difference-frequency generation using few-cycle pulses in simple collinear geometry," Opt. Lett. **38**, 4216–4219 (2013).
181. D. Kartashov, S. Ališauskas, A. Pugžlys, A. Voronin, A. Zheltikov, M. Petrarca, P. Béjot, J. Kasparian, J.-P. Wolf, and A. Baltuška, "White light generation over three octaves by femtosecond filament at 3.9 μm in argon," Opt. Lett. **37**, 3456–3458 (2012).
182. A. A. Voronin, J. M. Mikhailova, M. Gorjan, Z. Major, and A. M. Zheltikov, "Pulse compression to subcycle field waveforms with split-dispersion cascaded hollow fibers," Opt. Lett. **38**, 4354–4357 (2013).
183. A. Schwarz, "Few-cycle, phase-stable infrared OPCPA," Ph.D. dissertation (LMU, 2014).
184. A. Wirth, M. T. Hassan, I. Grguraš, J. Gagnon, A. Moulet, T. T. Luu, S. Pabst, R. Santra, Z. A. Alahmed, A. M. Azzeer, V. S. Yakovlev, V. Pervak, F. Krausz, and E. Goulielmakis, "Synthesized light transients," Science **334**, 195–200 (2011).
185. O. Razskazovskaya, et al., is preparing an article.
186. S. V. Bulanov, N. M. Naumova, and F. Pegoraro, "Interaction of an ultrashort, relativistically strong laser pulse with an overdense plasma," Phys. Plasmas **1**, 745–757 (1994).
187. R. Lichters, J. Meyer-ter-Vehn, and A. Pukhov, "Short-pulse laser harmonics from oscillating plasma surfaces driven at relativistic intensity," Phys. Plasmas **3**, 3425–3437 (1996).
188. T. Baeva, S. Gordienko, and A. Pukhov, "Theory of high-order harmonic generation in relativistic laser interaction with overdense plasma," Phys. Rev. E **74**, 046404 (2006).
189. G. D. Tsakiris, K. Eidmann, J. Meyer-ter-Vehn, and F. Krausz, "Route to intense single attosecond pulses," New J. Phys. **8**, 19 (2006).
190. P. Heissler, R. Hörlein, J. M. Mikhailova, L. Waldecker, P. Tzallas, A. Buck, K. Schmid, C. M. S. Sears, F. Krausz, L. Veisz, M. Zepf, and G. D. Tsakiris, "Few-cycle driven relativistically oscillating plasma mirrors: a source of intense isolated attosecond pulses," Phys. Rev. Lett. **108**, 235003 (2012).
191. J. M. Mikhailova, M. V. Fedorov, N. Karpowicz, P. Gibbon, V. T. Platonenko, A. M. Zheltikov, and F. Krausz, "Isolated attosecond pulses from laser-driven synchrotron radiation," Phys. Rev. Lett. **109**, 245005 (2012).
192. J. Tate, T. Auguste, H. G. Muller, P. Salières, P. Agostini, and L. F. DiMauro, "Scaling of wave-packet dynamics in an intense midinfrared field," Phys. Rev. Lett. **98**, 013901 (2007).
193. A. D. Shiner, C. Trallero-Herrero, N. Kajumba, H. C. Bandulet, D. Comtois, F. Légaré, M. Giguère, J. C. Kieffer, P. B. Corkum, and D. M. Villeneuve, "Wavelength scaling of high harmonic generation efficiency," Phys. Rev. Lett. **103**, 073902 (2009).

194. F. Krausz and M. I. Stockman, "Attosecond metrology: from electron capture to future signal processing," Nat. Photonics **8**, 205–213 (2014).
195. A. Harth, M. Schultze, T. Lang, T. Binhammer, S. Rausch, and U. Morgner, "Two-color pumped OPCPA system emitting spectra spanning 1.5 octaves from VIS to NIR," Opt. Express **20**, 3076–3081 (2012).
196. C. Manzoni, S. W. Huang, G. Cirmi, P. Farinello, J. Moses, F. X. Kärtner, and G. Cerullo, "Coherent synthesis of ultra-broadband optical parametric amplifiers," Opt. Lett. **37**, 1880–1882 (2012).
197. T. T. Luu, M. T. Hassan, A. Moulet, O. Razskazovskaya, N. Kaprowicz, V. Pervak, F. Krausz, and E. Goulielmakis, "Isolated optical attosecond pulses," in *CLEO*, OSA Technical Digest (online) (Optical Society of America, 2013), paper QF1C.6.
198. M. T. Hassan, "Attosecond control of bound electrons" (submitted).
199. F. X. Kärtner, O. Mücke, G. Cirmi, S. Fang, S.-H. Chia, C. Manzoni, P. Farinello, and G. Cerullo, "High energy sub-cycle optical waveform synthesizer," in *Advanced Solid-State Lasers Congress*, OSA Technical Digest (online) (Optical Society of America, 2013), paper AW2A.1.
200. S. N. Bagayev, V. I. Trunov, E. V. Pestryakov, V. E. Leschenko, S. A. Frolov, and V. A. Vasiliev, "High-intensity femtosecond laser systems based on coherent combining of optical fields," Opt. Spectrosc. **115**, 311–319 (2013).
201. G. M. Rossi, G. Cirmi, S. Fang, S.-H. Chia, O. D. Muecke, F. Kärtner, C. Manzoni, P. Farinello, and G. Cerullo, "Spectro-temporal characterization of all channels in a sub-optical-cycle parametric waveform synthesizer," in *CLEO*, OSA Technical Digest (online) (Optical Society of America, 2014), paper SF1E.3.
202. F. Shaobo, G. Cirmi, S. H. Chia, O. D. Mucke, F. X. Kartner, C. Manzoni, P. Farinello, and G. Cerullo, "Multi-mJ parametric synthesizer generating two-octave-wide optical waveforms," in *Conference on Lasers and Electro-Optics Pacific Rim* (Optical Society of America, 2013), paper WB3_1.
203. F. Verluise, V. Laude, Z. Cheng, C. Spielmann, and P. Tournois, "Amplitude and phase control of ultrashort pulses by use of an acousto-optic programmable dispersive filter: pulse compression and shaping," Opt. Lett. **25**, 575–577 (2000).
204. T. Binhammer, E. Rittweger, R. Ell, F. X. Kärtner, and U. Morgner, "Prism-based pulse shaper for octave spanning spectra," IEEE J. Quantum Electron. **41**, 1552–1557 (2005).
205. M. Lewenstein, P. Balcou, M. Y. Ivanov, A. L'Huillier, and P. B. Corkum, "Theory of high-harmonic generation by low-frequency laser fields," Phys. Rev. A **49**, 2117–2132 (1994).
206. M. Schultze, C. Y. Teisset, S. Prinz, D. H. Sutter, K. Michel, and T. Metzger, "Highly-efficient, optically synchronized thin disk amplifier for pumping OPCPA at high repetition rates between 100–300 kHz," Solid State Lasers XXIII: Technology and Devices, 2014, to be published.